MODELING AND VALIDATION OF THE BALING PROCESS IN THE COMPRESSION CHAMBER OF A LARGE SQUARE BALER

A Thesis

Submitted to the College of Graduate Studies and Research

in Partial Fulfillment of the Requirement

for the Degree of

Doctor of philosophy

in the

Department of Agricultural and Bioresource Engineering

University of Saskatchewan

Saskatoon, Saskatchewan

By

Sadegh Afzalinia

March, 2005

COPYRIGHT

ABSTRACT

The pressure-density relationship and the pressure distribution inside the compression chamber of a newly designed New Holland BB960 large square baler were studied for the baling of alfalfa, whole green barley, barley straw, and wheat straw. An analytical model was developed for the pressure distribution inside the compression chamber of the large square baler in the *x*-, *y*-, and *z*-directions by assuming isotropic linear elastic properties for forage materials. In order to validate this model, a tri-axial sensor was designed and used to measure the forces inside the compression chamber when whole green barley, barley straw, and wheat straw were baled. The experimental results proved that the developed analytical model for each of the tested forage materials had a good correlation with the experimental data with a reasonable coefficient of determination (0.95) and standard error (20.0 kPa). Test data were also used to develop an empirical model for the pressure distribution inside the compression chamber of the baler for each of the tested forage materials using least square method in regression analysis. These empirical models were simple equations which were only functions of the distance from the full extension point of the plunger along the compression chamber length.

Analytical and empirical models were also developed for the pressure-density relationship of the baler for baling alfalfa and barley straw. Results showed that bale density initially decreased with distance from the plunger, and then remained almost constant up to the end of the compression chamber. The developed empirical model for both alfalfa and barley straw was a combination of a quadratic and an exponential equation. In order to validate the developed models, field tests were performed by

baling alfalfa and barley straw of different moisture contents, flake sizes, and load settings. The forces on the plunger arms were recorded by a data acquisition system. The actual bale bulk density was calculated by measuring the bale dimensions and weight. Results showed that both load setting and flake size had a significant effect on the plunger force. The plunger force increased with increased load setting and flake size. Comparing analytical and empirical models for bale density as a function of the pressure on the plunger showed that the trend of variation of density with pressure in both models was similar, but the rate of change was different. The variation rate of density with pressure in the analytical model was higher than that of the empirical model. The analytical model underestimated the bale density at low plunger pressures but showed more accurate prediction at higher pressures, while the empirical model accurately predicted the bale density at both low and high pressures.

Some crop properties such as coefficient of friction and modulus of elasticity were determined for the development of the pressure distribution model. Results showed that static coefficient of friction of alfalfa on a polished steel surface was a quadratic function of material moisture content, while the relationship between the coefficient of friction of barley straw on a polished steel surface and material moisture content was best expressed by a linear equation. Results of this study also proved that modulus of elasticity of alfalfa and barley straw was constant for the density range encountered in the large square baler.

Acknowledgments

I would first like to thank Allah who enabled me to complete this work. I would like to express my great appreciation to my supervisor, Dr. Martin Roberge for his effective guidance, support, and encouragement during this study. I would also like to acknowledge the guidance and encouragement offered by the members of my advisory committee Dr. W. Szyskowski, Dr. T. G. Crowe, Dr. L. G. Tabil, Jr, and Dr. C. P. Maule and my external examiner Dr. B. Panneton. I would like to appreciate the encouragement and help received from the faculty and staff of the department of Agricultural and Bioresource Engineering, in particular the help extended by Wayne Morley in instrumentation set up.

I would like to extend my sincerest appreciation to my family for their encouragement and moral support during this study. This work would not have been possible without the financial support of Agricultural Research and Education Organization of Iran.

DEDICATION

This work is dedicated to my wife Mahnaz and my son Ehsan whose love and encouragement have always been with me.

TABLE OF CONTENTS

LIST OF TABLES

LIST OF FIGURES

LIST OF SYMBOLS

a	maximum height of compression chamber (cm)
A_0	model coefficient
A_d	adhesion coefficient (kPa)
AE	average error
b	maximum width of compression chamber (cm)
b_i	body force (N)
B_0, B_1, B_2	model coefficients
c	cut length (mm)
c_i, c_x, c_y, c_0	model coefficients
C	model coefficient
d	material property index
D	sample diameter (in)
D_a	average depth of the converging section of baler (m)
D_0	model coefficient
E	modulus of elasticity (MPa)
E_0	initial modulus of elasticity (MPa)
E_r	modulus of rupture (psi)
$E_{(\varepsilon)}$	modulus of elasticity as a function of strain (psi)
F_c	portion of the plunger force resulting from the convergence of the bale chamber side walls (N)
F_x	load in the x-direction (N)
F_y	load in the y-direction (N)

i, j, k	x, y, z
k_1, k_2	model coefficients
K	forage particle stiffness (MPa)
K_0	initial bulk modulus
K_1, K_2	variables which are linear functions of material moisture content, loading rate, and leaf content
l	model coefficient
L	compression chamber length (cm)
L_c	length of the converging section of baler (m)
L_s	sample length (m)
m	model coefficient
M_w	moisture content (% wb)
M_θ	bending moment in ring section at angular position θ (N m)
n	model coefficient
p_r	pressure ratio
P	compression pressure (MPa)
P_b	pressure at the base of compression chamber (MPa)
P_e	pressure at the end of compression chamber (MPa)
P_{max}	maximum pressure in the compression chamber (MPa)
P_p	pressure on the plunger (kPa)
P_x	pressure in x-direction at the distance x from the full extension point of the plunger (kPa)
P_y	pressure in y-direction at the distance x from the full extension point of the plunger (kPa)

P_z	pressure in z-direction at the distance x from the full extension point of the plunger (kPa)
q	model coefficient
r	compression ratio
R	radius (m)
S	tensile yield stress (kPa)
SE	standard error (%)
t	ring thickness (m)
V	bale volume as a function of distance from the full extension point of the plunger (m^3)
V_0	bale initial volume (m^3)
V_x	output of the horizontal force measurement bridge (v)
V_y	output of the vertical force measurement bridge (v)
ΔV	bale volume change (m^3)
w_c	width of the converging section of baler (m)
w_r	ring width (m)
W/A_a	cross-sectional area density (lb/in^2)
W_s	specific energy (MJ/t)
x	distance from the full extension point of the plunger (cm)
y	average lateral deflection of the hay (m)
y_e	experimental data
$\bar{y}_e$	average of experimental data
y_p	predicted data

α	angle of the top wall of the compression chamber with respect to the *x*-axis (radians)
β	angle of the side wall of the compression chamber with respect to the *x*-axis (radians)
δ_{ij}	Kronecker delta
γ_i	bulk density (lb/in^3)
γ_0	initial bulk density (kg/m^3)
γ_s	material bulk density (kg/m^3)
ε	material strain (m/m)
ε_e	material strain (in/in)
ε_θ	strain at the angular position θ on the ring (m/m)
θ	angle measured clockwise from the top of the ring (radians)
μ	coefficient of friction
ν	Poisson's ratio
σ	axial stress (psi)
σ_n	normal stress (kPa)
τ	shear stress (kPa)

CHAPTER 1

INTRODUCTION

Compressing forage materials into high-density packages is necessary to reduce handling and storage costs and to facilitate the storage operation. Making such packages requires a comprehensive understanding of the physical and the mechanical properties of these materials and their mechanical behavior under pressure. It is also important to know the pressure distribution within the compressed materials and the pressure-density relationship for different forage materials, and to be able to quantify the effect of material properties, machine characteristics, and operating conditions on this relationship.

Baled forage material is the major type of forage material considered on the commercial market. About 90% of produced forage material is baled by commercial balers. Among the commercial balers, small rectangular balers have low field capacity and produce small bales with low density in the range of 114 to 207 kg/m^3 (Hunt 2001). Round bales on the other hand have low density in the range of 100 to 170 kg/m^3, and have high transportation cost because of their cylindrical shape and low density (Hunt 2001, Culpin 1986, and Jenkins et al. 1985). Using a large square baler that produces large, high-density rectangular bales could very well eliminate the aforementioned problems. Therefore, to achieve accurate data for the bale compression chamber design and optimization in a newly designed large square baler, it is necessary to study the baling process which consists of: a) the relationship between the plunger pressure and

the bale density; b) the pressure distribution within the compression chamber in different directions; and c) the effect of machine settings and forage material properties on the baling process. In order to study the baling process, the first step is to measure the physical and mechanical properties of the forage materials which are baled with this baler. Accurate data of physical and mechanical properties of forage materials, such as particle stiffness and coefficients of internal and external friction, are needed to estimate the forces exerted on the bale and the compression chamber of the baler. These data are also needed as input to the analytical and numerical models of the forage material compaction process.

Applied forces on the forage material by the baler plunger are exerted on the bale chamber during the baling process. In order to design and optimize the bale chamber structure, comprehensive knowledge of these forces is necessary. Therefore, appropriate sensor is needed to record these compressive forces in orthogonal directions. The tri-axial sensor is a force transducer which is able to independently measure the forces in three directions. Ideally, this sensor should measure the forces independently, but in practice, there is always some cross sensitivities in this type of transducers because of errors in machining, locating the strain nodes, and installation of the strain gages. It is not possible to eliminate the cross sensitivity, but efforts must be made to reduce this effect during the design, fabrication, and calibration process.

It is also very important to study the pressure-density relationship, stress distribution along the bale, and the effect of different factors on the bale formation of field-scale balers to achieve accurate data for the bale compression chamber design and optimization.

In this project, a New Holland BB960 large square baler was used to bale alfalfa, whole green barley, barley straw, and wheat straw. This baler produces bales with 1.2 m width, 0.9 m height, and an adjustable length of up to 2.5 m. In this baler, forage materials are continuously picked up and fed into the baler using pick up system. A baffle plate conducts forage materials towards the baler, and centering augers transfer the crop from the ends of the pick up system into the packer. Double-tine packer fingers handle the materials from the pick up system into the pre-compression chamber, and crop holding fingers keep the forage materials in the pre-compression chamber, while still the stuffer fork is inactive. When the pre-compression chamber is filled by the forage materials, the stuffer system is activated by the pre-compression sensing mechanism. The top opening of the pre-compression chamber is cleared by the holding fingers, while the preset charge of forage materials are charged to the main compression chamber by the stuffer fork at the same moment. The plunger pushes these materials to the main compression chamber in its return stroke and compresses them against the partially formed bale in the previous strokes. When the material flake is fed into the main bale chamber, the material holding fingers return to their closed position. In this baler, top and side walls are hinged; therefore, they can be inclined by the side density cylinder according to the requested bale density. Top and side walls movement changes the bale outlet cross-section, and therefore controls the bale density (New Holland BB960 manual 2001).

The structure of this thesis is intended to provide the reader with a detailed description of previous works related to this research, theoretical analysis and experiments that were conducted during this study, state and discuss the results obtained from this research, summarize the findings of this study, and finally, to offer some suggestions and recommendations regarding this particular baler.

1.1 OBJECTIVES

1.1.1 General Objective

The general objective of this research was to develop and validate a model describing the baling operation process inside the compression chamber of a large square baler using various crops and different mechanical settings.

1.1.2 Specific Objectives

In order to achieve the main objective of this research, the following are the specific objectives:

a. to develop and validate an analytical model for the pressure distribution in the compression chamber as a function of the crop properties, bale chamber dimensions, and distance from the plunger along the compression chamber length;
b. to develop and validate an empirical model for the pressure distribution in the compression chamber as a function of distance from the plunger along the compression chamber length;
c. to develop and validate analytical and empirical models describing the relationship between plunger pressure and crop density; and
d. to evaluate the effects of flake size and load settings on the bale density and the plunger force.

CHAPTER 2

LITERATURE REVIEW

There are many published papers in the area of the physical properties of forage materials, their mechanical behavior when they are compressed, the pressure distribution along the compression axis of the compressed materials, and the relationship between applied pressure and material bulk density. In this review, efforts were made to gather the most important part of the existing information regarding physical properties and mechanical behavior of forage materials when they are compressed to high density. Wafering is a process during which, loose forage material is concentrated into a high density and compressed product. This compressed product is called a wafer. Most of the previous research has been conducted on the wafering process using a cylindrical die; however, this information can still be helpful to study the behavior of forage materials during the baling operation because of the similarity between wafering with a die and baling operations, which also incorporate wafering. Literature related to forage material physical and mechanical properties, compression characteristics, wafer formation, baling operation, tri-axial sensor design, and a summary of the review are topics covered in this chapter.

2.1 Physical and Mechanical Properties

Without knowledge of physical and mechanical properties of agricultural materials, an explanation of their behavior under compression is difficult. The following

sections provide a survey of previous studies and their findings about the coefficient of friction, adhesion and cohesion coefficients, particle stiffness, the modulus of elasticity, and Poisson's ratio.

2.1.1 Friction, Adhesion, and Cohesion Coefficients

The maximum friction (limiting friction) force is the maximum force needed to move a body which is subjected to a normal force against another body from rest. Once the body starts to move, the friction force decreases compared to the maximum friction force. This lower friction force is called sliding friction force. The ratio of the maximum friction force to the corresponding normal force is called static coefficient of friction. The ratio of the sliding friction force to the corresponding normal force is called sliding or kinetic coefficient of friction. The coefficient of friction between two layers of the same substance is called coefficient of internal friction, while the coefficient between two different materials is called the coefficient of external friction.

The friction coefficient plays an important role in the compression of forage materials. Applied pressure to the material during the baling process is directly affected by the coefficient of friction; therefore, it can affect the energy requirement of the baling process. The coefficient of friction depends on different parameters such as material moisture content, the surface of the compression chamber wall, material type, particle size, pressure, plant maturity, and position of the stem internode. Although, most research work in the field of the coefficient of friction of agricultural materials were related to grains, some literature was found regarding the static coefficient of friction of forage materials.

Richter (1954) for instance, determined the static and sliding friction coefficients for different forage materials. Coefficients of friction of chopped hay, chopped straw, and corn and grass silages on a galvanized steel surface were measured. The static and sliding coefficients of friction for chopped hay and straw were reported to range from 0.17 to 0.42 and 0.28 to 0.33, respectively. Based on these results, it was suggested that values of 0.35 and 0.30 be used for the static and sliding coefficients of friction of the chopped hay and straw, respectively. The range of 0.52 to 0.82 and 0.57 to 0.78 for the static and sliding coefficients of friction regarding corn and grass silages were also reported. It was also recommended that static and sliding coefficients of friction of 0.80 and 0.70 for corn and grass silages, respectively be used.

Bickert and Buelow (1966) determined the sliding coefficient of friction for shelled corn on a steel and plywood surface, and barley on a steel surface. The researchers reported that the sliding coefficient of friction was a linear function of material moisture content. Snyder et al. (1967) studied the effect of normal pressure and relative humidity on the sliding coefficient of friction of wheat grains on various metal surfaces. The results of their study showed that normal pressure and relative humidity had a small effect on the coefficient of friction. The value of the coefficient increased with increasing relative humidity in the range of 25 to 85%.

Brubaker and Pos (1965) evaluated the effect of the type of material, the type of surface, and the moisture content on the coefficient of friction of grains on structural surfaces. Three types of materials (wheat, soybeans, and nylon spheres), three different surfaces (Teflon, steel, and plywood), and four different moisture contents were considered. They found that an increase of moisture content increased the static coefficient of friction on all surfaces but Teflon. It was also reported that the moisture

content of plywood had a significant effect on frictional resistance on plywood. Furthermore, Thompson and Ross (1983) reported that the coefficient of friction of wheat grain on steel was affected by wheat moisture content. It was found that the coefficient of friction increased with increasing moisture content from 8 to 20%, but at 24% moisture content, it decreased.

In another study, Lawton and Marchant (1980) designed and fabricated a shear box to measure the coefficient of friction of agricultural seeds. The effect of the seed moisture content on the coefficient of internal friction of wheat, barley, oats, tick beans, and field beans was tested using the designed shear box. It was reported that material moisture content had a significant effect on the coefficients of internal friction of all the tested seeds; the coefficient increased with increasing moisture content. However, the rate of increment was higher for the moisture ranging from 15 to 25% wet basis (wb). Zhang et al. (1994) measured the coefficient of friction of wheat on corrugated galvanized steel, smooth galvanized steel, and wheat using a direct shear box. Three different levels of material moisture contents and four levels of normal pressures were considered. Results showed that increasing the normal pressure in the range of 9.73 to 70.53 kPa with the moisture content ranging from 11.9 to 17.7% (wb) decreased the coefficient of friction of wheat on a corrugated steel surface. It was also reported that the coefficient of friction of wheat on a corrugated steel surface increased with increasing moisture content.

Ling et al. (1997) determined the static and the kinetic coefficients of friction of wood ash on a stainless steel surface, and evaluated the effect of ash moisture content and the particle size on the coefficient of friction. Results of this study showed that both the static and the kinetic coefficients of friction increased with increasing ash moisture

content and decreased with increasing ash particle size. Moysey and Hiltz (1985) studied the effect of relative humidity and the method of filling the shear box on the coefficient of internal friction of some chemical fertilizers. The angle of repose for the tested fertilizers was also measured, and the results were compared with the coefficient of internal friction. It was concluded that the filling method had a significant effect on the coefficient of internal friction, while relative humidity had a small influence on the coefficient. It was also observed that the angle of repose was smaller than the angle of internal friction obtained using a direct shear box. Furthermore, it was found that the coefficient of friction of the tested fertilizers on the common bin wall materials was significantly higher than that of wheat on these materials.

Shinners et al. (1991) measured the friction coefficient of alfalfa on different surfaces as affected by the surface type, moisture content, velocity, the normal pressure, and the water lubrication rate. The moisture content was found to have a significant effect on the coefficient of friction so that it was lower in the moisture range of 33 to 37% (wb) than the range of 73 to 77% (wb). In this study, the two highest coefficients of friction (0.529 and 0.49) were obtained from polished steel and the glass coated steel surfaces, respectively. The lowest coefficients (0.416, 0.402, and 0.375) were obtained from polyethylene, iron oxide-coated steel, and Teflon coated steel, respectively. Furthermore, the normal pressure and velocity in the tested range had no significant effect on the friction coefficient, and the friction coefficient was reduced by the water lubrication by an average of 67% for the all tested surfaces.

Ferrero et al. (1990) introduced the following analytical model for calculating the coefficient of friction of straw from the die geometry, the wafer length, and the applied pressure:

$$\mu = -(D / 4 p_r L_s) \ln(P_b - P), \quad (2.1)$$

where:

μ = coefficient of friction,

D = sample diameter (m),

p_r = pressure ratio,

L_s = sample length (m),

P_b = pressure at the base of compression chamber (MPa) and

P = compression pressure (MPa).

A direct relationship between the coefficient of wall friction and the straw moisture content was also found, while there was an inverse relationship between the straw compressed density and the coefficient of wall friction.

Cohesion is the mutual attraction of particles of the same substance, while adhesion is the attraction of dissimilar substances for each other. Mani et al. (2003) measured the static coefficient of friction and the adhesion coefficient of corn stover grind on a galvanized steel surface at different particle sizes and moisture contents. The results showed that moisture content had a significant effect on the coefficient of friction but adhesion was not affected by moisture content. Tabil and Sokhansanj (1997) determined the cohesions of alfalfa grinds from low quality chop ground in a hammer mill with two different screen sizes of 2.4 and 3.2 mm. They reported cohesions of 2.19 and 2.51 kPa for alfalfa ground using 3.2 and 2.4 mm screen sizes, respectively.

2.1.2 Particle Stiffness

Particle stiffness is the ability of particles to resist deformation within the linear range. Bilanski et al. (1985) studied the mechanical behavior of alfalfa under compression in a closed-end cylindrical die. They developed an analytical model for the material bulk density in terms of the applied axial pressure and a constant coefficient (K). They validated the derived model using their experimental data for alfalfa, and found the value of 16.85 MPa for the model constant at a moisture content of 14% (wb). They claimed that the model constant was particle stiffness; however, they did not prove that. Mani et al. (2003) evaluated the effect of particle size and moisture content on the particle stiffness of corn stover grind. The results showed that moisture content and particle size had significant effect on the particle stiffness; particle stiffness increased with increasing particle size and decreased with increasing moisture content.

2.1.3 Modulus of Elasticity and Poisson's Ratio

Modulus of elasticity is defined as the slope of the linear part of the stress-strain curve of engineering materials. For biological materials, the apparent modulus of elasticity is used to explain the relationship between stress and strain. Apparent modulus of elasticity is calculated based on two different definitions called the secant definition and the tangent definition. In the secant definition, the apparent modulus is considered as the ratio of stress to strain at a certain point, while the apparent modulus in tangent method is defined as the slope of the stress-strain curve at a certain point on the curve (Stroshine 2000). The modulus of elasticity of forage materials varies during the compression process. The magnitude of this modulus mainly depends on the material volumetric weight; however it is slightly affected by the material moisture content

(Sitkei 1986). Sitkei (1986) proposed the following equation for the variation of Young's modulus of forage materials during compression in terms of initial Young's modulus, initial bulk density, and material strain:

$$E_{(\varepsilon)} = E_0 + C\gamma_0{}^2(\varepsilon_e/(1-\varepsilon_e)^2), \tag{2.2}$$

where:

$E_{(\varepsilon)}$ = modulus of elasticity (psi),

E_0 = initial modulus of elasticity (psi),

C = model coefficient,

γ_0 = initial bulk density (lb/in^3) and

ε_e = material strain (in/in).

Norris and Bilanski (1969) emphasized that the tensile modulus of elasticity for the alfalfa stems was proportional to the stem bulk density and varied from 0.9 to 6.8 GPa (1.3 x 10^5 to 9.87 x 10^5 psi). These values are very high for forage materials and are not reliable.

O'Dogherty (1989) cited the work of Osobov (1967) who suggested an exponential equation for the modulus of elasticity as a function of bulk density in the closed-end die in the following form:

$$E = E_0 \exp[(\gamma_s - \gamma_0)/n], \tag{2.3}$$

where:

γ_s = material bulk density (kg/m^3),

γ_0 = initial bulk density (kg/m^3),

E = modulus of elasticity (MPa),

E_0 = initial modulus of elasticity (MPa) and

n = model coefficient.

O'Dogherty et al. (1995) studied the effect of plant maturity, position of the stem internode, and stem moisture content on the physical and mechanical properties of wheat straw. The results showed that the modulus of elasticity of wheat stems was affected by plant maturity so that it increased with more advanced stage of plant maturity, whereas, plant maturity had no significant effect on other stem physical properties. Elastic modulus was also affected by the position of stem internode so that the fourth stem internode (measured downward from the head) had the highest modulus of elasticity, while the first stem internode had the least modulus of elasticity.

Poisson's ratio is the absolute value of the ratio of the lateral strain over the axial strain. Applied pressure to forage materials during the compression is also a function of Poisson's ratio. O'Dogherty (1989) cited the work of Mewes (1958 and 1959) who reported that the maximum value of Poisson's ratio for wheat straw was 0.5 at an applied pressure of 177 kPa and it decreased to less than 0.1 by increasing applied pressure up to 1.4 MPa.

2.2 Compression Characteristics

Previous studies related to the pressure-density relationship, pressure distribution inside the compressed material, and energy requirement are reviewed in the next three subsections.

2.2.1 Pressure-Density Relationship

There is a direct relationship between the applied pressure and the forage material bulk density during the compaction process. Most reported models for the pressure-density

relationship have either power law or exponential forms. Hundtoft and Buelow (1971) studied the relationship between stress and strain during compression of bulk alfalfa. The axial pressure was correlated to variables such as material moisture content, sample size, and strain. They chopped the alfalfa with a length of 1/8 in. and compressed the chopped material in a 3 in. diameter compression cylinder at a constant strain rate of 1 in/in-s. The equation of the axial pressure in terms of tested variables was given as:

$$\sigma = (124 / M_w^{\,2})(M_w + 0.032W / A_a)(\varepsilon_e + 1.36M_w)^{-(0.69+6.1M_w)}, \qquad (2.4)$$

where:

σ = axial pressure (psi),

M_w = wet basis moisture content ranging from 0.13 to 0.4 (decimal),

W/A_a = cross-sectional area density ranging from 1 to 3 (lb/in^2) and

ε_e = bulk strain ranging from 0.2 to 4.0 (in/in).

The shortcoming of this model appears at low strain values. This model predicted unreasonable values for axial stresses at low values of strain (Bilanski et al. 1985).

O'Dogherty and Wheeler (1984) introduced the following empirical models to show the pressure-density relationship of barley straw compressed in a cylindrical die:

$$P = 0.000012\gamma_s^{\,2} \qquad \text{for} \quad 150 < \gamma_s < 400 \text{ kg/m}^3 \qquad \text{and} \qquad (2.5)$$

$$\ln P = 0.00226[\ln(\gamma_s)]^4 - 2.32 \qquad \text{for} \quad \gamma_s > 400 \text{ kg/m}^3, \qquad (2.6)$$

where:

P = compression pressure (MPa) and

γ_s = material bulk density (kg/m^3).

The density range encountered in balers is less than 400 kg/m^3; therefore, Eq. 2.5 is applicable to the pressure-density relationship in balers, but it has the same shortcoming as Eq. 2.4.

Bilanski et al. (1985) studied the mechanical behavior of alfalfa under compression in a closed-end cylindrical die. An analytical model was derived to express the relationship between the applied axial pressure and the material bulk density by assuming constant bulk modulus and then the derived model was validated with the experimental data. The analytical model is given below:

$$(\gamma_{\max} - \gamma_s)/(\gamma_{\max} - \gamma_0) = e^{(-P/K)}, \tag{2.7}$$

where:

γ_s = material bulk density (kg/m^3),

γ_{max} = maximum bulk density (kg/m^3),

γ_0 = initial bulk density (kg/m^3),

P = compression pressure (MPa) and

K = forage particle stiffness (MPa).

They estimated γ_{max} and K from the experimental data for alfalfa in the pressure range of 0.0 to 39.3 MPa and validated the abovementioned model as follow:

$$(1405 - \gamma)/(1405 - \gamma_0) = e^{(-P/16.85)}. \tag{2.8}$$

They also developed the following empirical model for the relationship between the cohesive strength and the recovered density in compressed alfalfa:

$$S = A_0 \gamma_s^{B_0} - C, \tag{2.9}$$

where:

S = tensile yield stress (kPa),

γ_s = material bulk density (kg/m^3) and

A_0, B_0, C = model coefficients.

Figure 2.1 shows a typical pressure-density curve based on Bilanski's model (Eq. 2.7). This graph properly explains the mechanical behavior of forage materials under compression. At the beginning of the compression process, forage materials resist deformation under small pressures (density remains constant with increasing pressure), but when pressure exceeds a certain amount, materials start to buckle. After that point, density increases with increasing applied pressure until materials behave as incompressible materials, and density remains constant from that point.

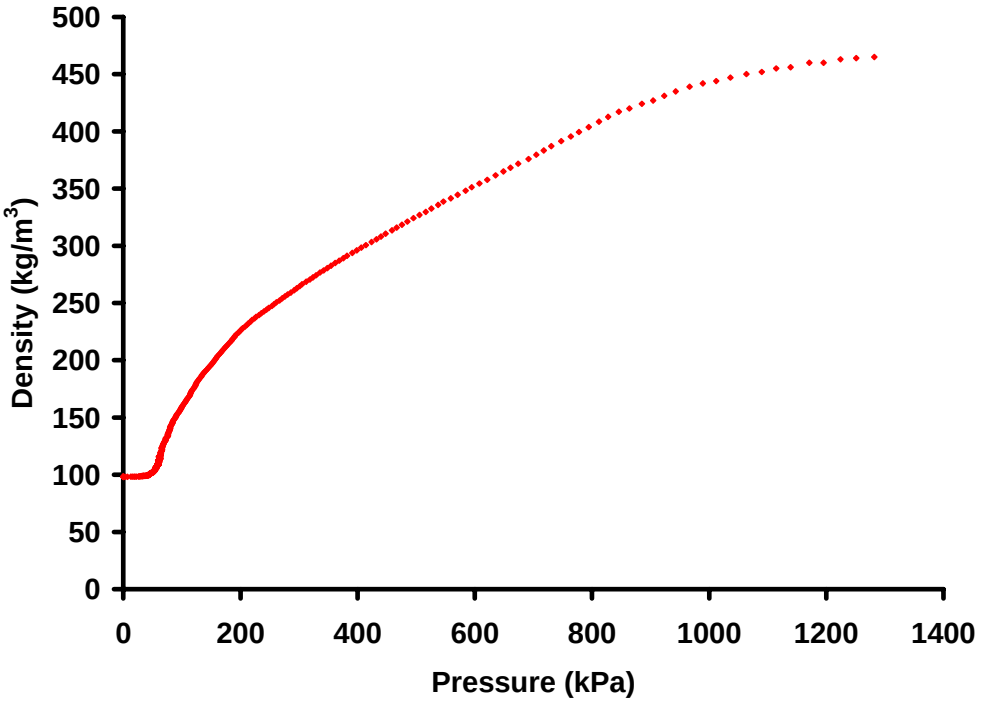

Figure 2.1 Pressure-density relationships for barley straw at a moisture content of 30% (wb) based on Bilanski's model (Eq. 2.8).

Butler and McColly (1959) introduced the following empirical model to express the compressed straw density as a function of the applied axial pressure:

$$\gamma_i = k_1 \ln(\sigma / k_2), \tag{2.10}$$

where:

γ_i = bulk density (lb/in^3),

σ = applied axial pressure (psi) and

k_1, k_2 = model coefficients.

Bilanski et al. (1985) reported a power law equation for the pressure-density relationship of the compressed straw. The equation had the following form:

$$P = C\gamma_s^{\,m}, \tag{2.11}$$

where:

P = compression pressure (MPa),

γ_s = material bulk density (kg/m^3) and

C, m = model coefficients.

Equations 2.11 and 2.12 were developed using a low loading rate; therefore, these models are not applicable to the compression process at high loading rates. On the other hand, initial conditions ($P = 0$ and $\gamma = \gamma_0$) are not defined for Eq. 2.11. Therefore, these models can predict material density for a certain range of applied pressure (Bilanski et al. 1985).

Faborode and O'Callaghan (1986) theoretically studied the compression process of agricultural materials. They derived a new model for the compression pressure in terms of compression ratio ($r = \gamma/\gamma_0$) and the initial density:

$$P = \frac{A_0 \gamma_0}{d}\left[e^{d(r-1)} - 1\right], \tag{2.12}$$

where:

P = compression pressure (MPa),

γ_0 = initial bulk density (kg/m^3),

d = material property index,

r = compression ratio and

A_0 = model coefficient.

They also developed the following model for the compression pressure in terms of material deformation:

$$P = \frac{K_0}{d}\left[e^{d(\varepsilon/(1-\varepsilon))} - 1\right], \tag{2.13}$$

where:

ε = material strain (m/m) and

K_0 = initial bulk modulus.

O'Dogherty and Wheeler (1989) introduced an equation for applied pressure as a function of the material relaxed bulk density for compacted barley straw. The equation had the following form:

$$P = A_0 e^{B_0 \gamma_s}, \tag{2.14}$$

where:

P = compression pressure (MPa),

γ_s = material bulk density (kg/m^3) and

A_0, B_0 = model coefficients.

O'Dogherty and Wheeler (1989) also reported the relationship between pressure, moisture content, and the relaxed density of compressed wheat straw as given below:

$$\gamma_s = (1/l)\left[(P-7)/m\right]^{M_w/n} \ln(P/q), \tag{2.15}$$

where:

P = compression pressure (MPa),

γ_s = material bulk density (kg/m^3),

M_w = straw moisture content (% wb) and

l, m, n, q = model coefficients.

Ferrero et al. (1990) studied the pressure-density relationship of compressed straw. They compressed chopped wheat and barley straw with maximum length of 40 mm and moisture contents ranging from 7 to 23 and 10 to 20%, respectively. The pressure range of 20 to 100 MPa at a loading rate of 13 mm/s was applied to the materials and the following empirical model was fitted to the experimental data:

$$\gamma_s = \gamma_0 + (A_0 + B_0 P)(1 - e^{-CP}), \tag{2.16}$$

where:

γ_s = material bulk density (kg/m^3),

γ_0 = initial bulk density (kg/m^3),

P = compression pressure (MPa) and

A_0, B_0, C = model coefficients.

Watts and Bilanski (1991) reported that the maximum stress in alfalfa wafers for a certain deformation was a function of the material density in the form of:

$$P = K_1 \log\left[1 - K_2(\gamma_s - \gamma_0)\right] \tag{2.17}$$

where:

P = compression pressure (MPa),

γ_s = material bulk density (kg/m^3),

γ_0 = initial bulk density (kg/m^3) and

K_1, K_2 = variables which are linear functions of material moisture content, loading rate, and leaf content.

Viswanathan and Gothandapani (1999) studied the pressure-density relationship of compressed coir pith with different levels of moisture contents and particle sizes. They compressed coir pith in the pressure range of 1 to 416 kPa and used the following empirical model for the pressure-density relationship:

$$P = A_0 + B_0\gamma_s + C\gamma_s^{\,2}, \tag{2.18}$$

where:

P = compression pressure (kPa),

γ_s = material bulk density (kg/m^3) and

A_0, B_0, C = model coefficients.

Most of the developed models for the pressure-density relationships are generally either exponential or power law relationships. In most cases, the shortcomings of these models appear at the initial and boundary conditions where they fail to predict the density at these conditions. It seems that a good model for the pressure-density should have an exponential term to satisfy the boundary condition of $P = \infty$ and γ_{max} = constant. On the other hand, there should be either a linear or a quadratic term to satisfy the initial condition of $P = 0$ and $\gamma = \gamma_0$. Therefore, a model containing a combination of an exponential and either a linear or a quadratic term such as Eq. 2.16 could best express

the pressure-density relationship in compressed forage materials. It should also be noted that all aforementioned models have been developed based on data obtained from compressing forage materials in a closed-end cylindrical die. Thus, the models cannot be exactly extended to the baling process.

2.2.2 Pressure Distribution

Sitkei (1986) introduced a model for the stress distribution inside the forage bale at a distance x from the full extension point of the compressing plunger in terms of the material properties and the compression chamber dimensions by assuming isotropic linear elastic property for forage materials. The model had the form of:

$$P_x = P_e^{A_s(L-x)} + (B_s / A_s\alpha^2)(e^{A_s(L-x)} - 1) + (B_s a^2 / \alpha^3)(e^{A_s(L-x)} / \xi_L - 1/\xi) + e^{(A_s/\alpha)\xi} \quad K_s\left[\int_{\xi=a}^{\xi_L} (e^{-(A_s/\alpha)\xi} / \xi)d\xi - \int_{\xi=a}^{\xi} (e^{-(A_s/\alpha)\xi} / \xi)d\xi\right] \quad , \tag{2.19}$$

where:

$$A_s = \left[(\alpha + 2\mu)/a_m + 2\mu/b\right]\nu/(1-\nu), \tag{2.20}$$

$$B_s = C\gamma_0{}^2\alpha^2\left[(\alpha + 2\mu)/a_m(1-\nu^{2)} + (2\mu/b)\nu/(1-\nu^2)\right], \tag{2.21}$$

$$K_s = A_s B_s a^2/\alpha^4 + 2aB_s/\alpha^3, \tag{2.22}$$

$$\xi = a - \alpha x, \tag{2.23}$$

$$a_m = a - \alpha(l/2), \tag{2.24}$$

$$\xi_L = a - \alpha L, \tag{2.25}$$

P_x = pressure in the x-direction at the distance x from the full extension point of plunger (kPa),

P_e = pressure at the end of the compression chamber (kPa),

L = compression chamber length (cm),

x = distance from the full extension point of the plunger along the compression chamber length (cm),

α = angle of top wall of compression chamber (radian),

γ_0 = initial bulk density (kg/m^3),

μ = coefficient of friction between forage and compression chamber wall,

ν = Poisson's ratio,

a = maximum height of compression chamber (cm),

b = maximum width of compression chamber (cm) and

C = model coefficient.

The shortcomings of this model were as follows:

a. it was derived for the bale chambers with only the top wall inclined, therefore it could not be a general model for the pressure distribution,
b. in this model, pressure at the end of bale chamber was used as the boundary condition to solve the governing differential equation which is difficult to measure in practice and
c. there are some unnecessary terms in the model making it more complicated.

Faborode and O'Callaghan (1986) derived an equation to express the pressure distribution in the compression die given by the following:

$$P_x = \frac{K_0}{d}\left[e^{d(r-1)} - 1\right]e^{(-\mu p_r x)/R}, \tag{2.26}$$

where:

P_x = pressure in the x-direction at the distance x from the full extension point of plunger (MPa),

K_0 = initial bulk modulus,

d = material property index,

r = compression ratio,

μ = coefficient of friction between die wall and forage materials,

x = distance from the full extension point of the plunger along the compression chamber length (cm),

p_r = pressure ratio and

R = die radius (m).

Kepner et al. (1972) proposed the following equation to estimate the portion of the plunger force which comes from the convergence of the bale chamber side walls:

$$F_c = E\frac{y}{D_a}(2L_c w_c)\mu, \tag{2.27}$$

where:

F_c = portion of the plunger force resulting from the convergence of the bale chamber side walls (N),

E = modulus of elasticity of the forage material (Pa),

y = average lateral deflection of the hay (m),

D_a = average depth of the converging section of baler (m),

L_c = length of the converging section of baler (m),

w_c = width of the converging section of baler (m) and

μ = coefficient of friction between the forage materials and chamber walls.

They emphasized that this equation covered only the side walls' convergence force rather than bottom wall friction force and the effect of the bottom wedges. Furthermore, in the case of four-side convergence, the two F_c values should be considered.

Burrows et al. (1992) reported that in a high density baler, the compaction force and the piston stroke had a parabolic relationship, when wheat straw with an initial density of 92 kg/m^3 was baled.

2.2.3 Energy Requirement

Reece (1967) designed a new wafering machine that continuously formed wafers. The machine was tested by producing wafers from chopped alfalfa with 25% moisture content, compression pressure of 13.81 MPa (2000 psi), and a holding time of 13 s. The results showed that the energy requirement for forming the wafer by this machine with the abovementioned conditions was 3.23 Watt-h/kg (4.20 hp-h/t).

Hann and Harrison (1976) reported that in order to make wafers from alfalfa with a cut length of 1.5 in. using a hydraulic wafering press, approximately 4.61 Watt-h/kg (6 hp-h per ton of dry hay) was required. Mohsenin and Zaske (1976) studied the compaction of alfalfa hay and fresh alfalfa at different moisture contents and concluded that the compaction energy required to achieve a certain bulk density for low moisture hay was higher than that of the high moisture hay.

O'Dogherty and Wheeler (1984) reported the following equation to express the relationship between the specific energy and the material relaxed bulk density of compressed barley straw:

$$W_s = 0.0525\gamma_s - 5.00, \tag{2.28}$$

where:

W_s = specific energy (MJ/t) and

γ_s = material bulk density (kg/m^3).

Sitkei (1986) derived the following equation for the specific energy requirement of compressed forage materials as a function of the applied pressure and material bulk density:

$$W_s = \int_{\gamma_0}^{\gamma_s} Pd(1/\gamma_s) + P_{\max}/\gamma_{\max}, \tag{2.29}$$

where:

W_s = specific energy,

P_{max} = maximum pressure in the compression chamber,

γ_s = material bulk density,

γ_{max} = maximum bulk density and

γ_0 = initial bulk density.

Faborode and O'Callaghan (1986) reported that the specific energy of forage materials increased during the compression process when the maximum applied pressure increased. Freeland and Bledsoe (1988) compared seven different models of the large round baler from the energy requirement viewpoint. They evaluated the effect of chamber type and the operational procedures on the energy requirement of the balers. The baler models with either fixed-geometry or variable-geometry chambers were considered. They introduced a characteristic power curve for each of the balers, and concluded that the fixed-geometry chamber needed more power to bale a certain amount of materials compared to the variable-geometry chamber baler.

2.3 Wafer Formation

Wafer formation is affected by the physical characteristics of the materials that are to be compressed such as crop moisture content, quality of forage materials, and

particle size. The following sections describe the effect of these parameters on wafer formation.

2.3.1 Moisture Content

Pickard et al. (1961) studied the effect of the hay moisture content on the pressure requirement of alfalfa wafers. Results of their research showed that at a constant wafer density, the required pressure to form the wafer increased with increasing alfalfa moisture content.

Rehkugler and Buchele (1967) evaluated the effect of moisture content of alfalfa forage on the formation of wafers in a closed-end die. The results showed that wafer density decreased with increased moisture content; therefore, concluded that to have a high density wafer, moisture content of materials must be low.

Hall and Hall (1968) used a quadratic equation to express the wafer forming stress at different die heating levels in terms of alfalfa moisture content in the form of:

$$\sigma = B_0 + B_1 M_w + B_2 M_w^{\,2}, \tag{2.30}$$

where:

σ = required pressure (psi),

M_w = moisture content (% wb) and

B_0, B_1, B_2 = model coefficients.

Srivastava et al. (1981) studied the effect of material moisture content on the compression ratio, wafer density, and durability in the compaction of a mixture of alfalfa and grass. They found that 11% (wb) was the optimum moisture content to get the highest wafer density, durability, and the compression ratio. In another study, the range

of 10 to 20% (wb) was found to be the best moisture content of straw in order to produce high durability wafers (O'Dogherty and Wheeler 1984).

2.3.2 Quality of Forage Materials

Pickard et al. (1961) studied the effect of the hay maturity on the pressure requirement of alfalfa wafers. Results of their research showed that at a constant wafer density, the required pressure to form the wafer increased with increasing alfalfa maturity.

Reece (1966) studied the effect of alfalfa quality on the wafer durability. Wafer formation was affected by the hay quality which was different for the hay coming from the first and the second cuts. The hay from the second cut alfalfa resulted in a wafer with a higher durability compared to the hay from the first cut due to its higher leaf-to-stem ratio.

Rehkugler and Buchele (1967) evaluated the effect of the percentage of alfalfa stem on the formation of wafers in a closed-end die. The experiments were performed on both chopped and ground materials. The results showed that the high quantity of stem in the material had an inverse effect on the formation of the wafer by decreasing protein content as binding material. Grinding forage materials also decreased the expansion of the wafer by changing the stem's physical property.

2.3.3 Particle Size

O'Dogherty and Wheeler (1984) reported that durability of the straw wafer decreased by chopping the material to be wafered. O'Dogherty and Gilbertson (1988) conducted a study to establish a empirical relationship between the bulk density and the cut length of wheat straw. Wheat straw was cut to a uniform length of 15 to 250 mm and

the samples were placed into a cylindrical container and a low pressure (100 Pa) was applied to them. After measuring the bulk density of the samples at different cut lengths, the following empirical model for the density-cut length relationship was developed:

$$\gamma_s = 98.17/[0.03412c + (1.109/c) + 1], \quad (2.31)$$

where:

γ_s = material bulk density (kg/m^3) and

c = cut length (mm).

2.4 Studies Related to Baling Operation

Corrie and Bull (1969) compared large rectangular hay bales with the conventional bales at similar moisture content and density from the viewpoint of heating, nutrient losses, and molding. The study showed that heating occurred in large bales more than small ones at a certain dry matter density and moisture content, and it was significantly affected by the dry matter bulk density, while nutrient losses were higher in small bales compared to large bales. The results also indicated that decreasing the dry matter density reduced the heating problem of the bales with a moisture content of more than 25%, however this could not eliminate the risk of being contaminated with mold. Meanwhile, the large rectangular bales provided a more efficient handling system compared to the small ones.

Fairbanks et al. (1981) evaluated the effect of three types of baling machines on the quality and the quantity of harvested hay. A small round baler, a big round baler, and a mechanical stack maker were used in this study. The percentage of the crude fibre, protein, and ash was measured as the quality factors immediately after baling and then

six months afterward. Results of this study revealed that there was no significant difference between the quality of the fibres taken immediately after harvesting and those taken after six months of storage; however, hay quality decreased with an increase in precipitation.

Jenkins et al. (1985) used a large rectangular baler to collect and handle rice straw, and compared its performance to that of a big round baler and the conventional handling equipment. An economic comparison among the equipment was also conducted. The results indicated that the large rectangular baler had the lowest handling cost compared to the other available handling systems if the baler capacity was kept high. Rain could easily penetrate the rectangular bales in an uncovered storage condition, while rain penetration was limited to the outside surface in big round bales. They concluded that, in contrast to the round bales, big rectangular bales must be stored with cover.

Shinners et al. (1992) compared the performance of two small rectangular balers with different feeding systems (side fed and bottom fed chamber) from the viewpoint of the bale chamber and pick up losses. Results indicated 1.09 and 1.31% pick up losses for the bottom and the side fed chambers, respectively. Therefore, the bottom-fed baler pick up loss was 17% lower than that of the side fed chamber baler. Furthermore, they reported 2.28 and 2.66% chamber losses for the bottom fed and the side fed chamber baler, respectively (14% lower loss for the bottom fed chamber baler).

Coblentz et al. (1993) designed a new laboratory scale baler to make 10.3 by 10.8 by 13.4 cm wire-tied bales. The system was producing bales with densities of 150 to 800 kg/m^3. The laboratory bale density was compared with that of the conventional small-square alfalfa bales and a good correlation was found.

Shinners et al. (1996) compared the harvest and the storage losses of different types of balers. Mid-size and small rectangular balers and the large round baler for the harvesting losses comparison were considered. The pick up and the bale chamber losses were compared for the considered balers. The results showed that the pick up losses of the mid-size and the small rectangular and the large round baler were 0.7, 0.4, and 2.6% of the total dry weight of the collected hay, respectively; therefore, the rectangular balers had less pick up losses than the round balers. The bale chamber losses were 0.7, 1.6, and 1.6% of the total dry weight of the collected hay for the mid-size and the small rectangular balers and the large round baler, respectively; therefore, the mid-size rectangular baler had the least bale chamber loss.

2.5 Tri-axial Sensor Design

Forces applied to the forage material by the baler plunger are exerted on the bale and bale chamber during the baling process. In order to model the pressure distribution resulting from these forces, comprehensive knowledge of these forces is necessary. Therefore, a tri-axial sensor is needed to record these compressive forces in three directions. In this section, a review of studies related to sensor design is presented.

The tri-axial sensor is a force transducer which is able to measure the forces in three directions independently using an extended octagonal ring (EOR). The EOR was developed from the circular ring force transducer to give more stability to the transducer. The idea of using the EOR in a measurement system was first introduced by Lowen et al. (1951). Hoag and Yoerger (1975) derived analytical equations of stress distribution for the simple and the extended ring transducers at different loading and boundary conditions using the strain energy method. This study resulted in two equations

developed for the bending moment in the ring section of the extended ring which are used for moment calculation in the ring section of the EOR as well. Thereafter, modifications were brought to one of the Hoag and Yoerger's equations by McLaughlin (1996).

Godwin (1975) designed an extended octagonal ring transducer to measure the soil reaction forces to the soil engaging tools in two directions and the moment in the plane of these forces. A good linearity, small cross sensitivity, and hysteresis were reported. Meanwhile, the practical sensitivities of the strain gages were much more than the obtained values from the analytical equations. O'Dogherty (1975) fabricated a transducer to determine the cutting and vertical forces of a sugar beet topping knife using an extended octagonal ring. The results showed a good linearity, low hysteresis in loading and unloading cycles, and cross sensitivities of 4.1 and 6.5% for the cutting and the vertical forces, respectively in the calibration process of the transducer. Based on this calculation, a modification to the coefficients of the formula which is used for the EOR transducers was suggested; coefficients of 1.6 and 1.9 instead of 0.7 and 1.4 in the equations of the vertical and the horizontal forces, respectively.

Godwin et al. (1993) designed a dynamometer using the EOR to measure the exerted forces and moments on tillage tools. Two EOR in back-to-back form which their longitudinal axes were making angles of 90^0 were used. The dynamometer using a tri-axial loading method was calibrated and excellent linearity between the applied forces and moments and the bridge output voltage was found. A small amount of hysteresis effect between loading and unloading calibration curves, and cross sensitivity of less than 4% was reported; however, in one case the reported cross sensitivity was 10.6%.

Gu et al. (1993) designed and built a transducer to measure the vertical and the horizontal forces on the wheels of a quarter scaled model tractor using two EORs with the stress nodes at positions of $\theta = \pm 45^{\circ}$ and $\theta = 0^{\circ}$. The transducer was calibrated by applying independent forces in two perpendicular directions, and a regression model for each of the vertical and the horizontal primary sensitivities and the cross sensitivities was developed. Cross sensitivities ranging from around zero to four percent were reported.

O'Dogherty (1996) derived a formula to determine the ring thickness of the EOR transducer using the data of the designed transducers by previous researchers. He introduced a graphical procedure for the EOR design based on the geometrical parameters of the ring. McLaughlin and co-workers (1998) designed and fabricated a double extended octagonal ring (DEOR) drawbar transducer. They calibrated the transducer using both uni-axial and tri-axial loading method. From the uni-axial loading calibration, sensor cross sensitivities were assessed at 1.9 and 7.0% for the draft and the vertical loading, respectively. From the tri-axial loading calibration, regression models were derived to predict each of the draft, vertical, and side loads. The designed transducer was also used to measure the draft, the vertical, and the side loads on the drawbar of two secondary tillage tools and proved to be reliable in the field to measure the drawbar forces.

2.6 Summary

Most of the information found in the literature about coefficients of friction was related to the kinetic coefficient of friction rather than the static coefficient of friction. Only one study was found about static coefficient of friction of some forage materials

(Richter 1954), but results of this research were not reliable because the moisture content of materials has not been reported. Regarding other properties such as modulus of elasticity and particle stiffness, information found in the literature were for materials different from those used in this study. The results of crop properties from literature are not directly extendable to this study; however, this information can help understand crop behavior during the baling process. This information also gives an idea about methods of measuring crop properties.

In the area of pressure-density relationships, more literature was found, however all developed models were based on the data of compressing forage materials in a closed-end cylindrical die. Although, these models cannot be directly extended to the pressure-density relationship in balers, some of them (recently derived ones) give information about the form of the pressure-density model in balers. They can also help to determine the factors affecting this relationship.

The knowledge of pressure distribution along the axis of compression for compressed forage materials, as expressed within the literature (Eqs. 2.19 and 2.26), provides an idea about the pattern of pressure distribution in a large square baler and the parameters affecting this pattern. Only two models (Sitkei1986 and Faborode and O'Callaghan1986) were found in the literature regarding pressure distribution. One was based on data released from compressing forage materials in a cylindrical die which is not extendable to the pressure distribution in a bale chamber. The other one was an analytical model which has been developed for a bale chamber by assuming an isotropic linear elastic property for forage materials. The latter model had three shortcomings as follows:

a. it was derived for bale chambers with only the top wall inclined, whereas in a large square baler not only the top wall, but the side walls are also inclined;
b. in this model, the pressure at the end of bale chamber was used as the boundary condition to solve the governing differential equation which is difficult to measure in practice; and
c. there are some unnecessary terms in the model, making it more complicated.

The aforementioned shortcomings in previous studies justify distinct experimental and theoretical studies on the pressure-density relationships and the pressure distribution during the baling process.

CHAPTER 3

MATERIALS AND METHODS

In this chapter, model development, materials and methods used to carry out the experiments, instrumentation set up, and field and laboratory tests are described.

3.1 Model Development

In this section, model development for the pressure distribution and pressure-density relationship is explained. In each case, development of both analytical and empirical models is covered.

3.1.1 Pressure Distribution

3.1.1.1 Analytical Model

The compositions and the properties of forage materials change continuously during growth, maturity, and even after harvest because they are alive and biological materials. These materials consist of solid and liquid components which make a very complex construction whose mechanical behavior cannot be characterized by simple equations and constants. The mechanical behavior of these materials varies with factors such as loading rate, previous history of loading, material composition, and moisture content. Therefore, most agricultural materials do not follow linearity in compression tests even at small deformations. Because the load-deformation relationship in forage materials depends on deformation rate, time also plays a role in this relationship. Thus,

these materials are categorized as viscoelastic. In spite of being aware of the aforementioned fact and in order to simplify the problem in this study, it was assumed that the forage material behaves as an isotropic linear elastic material. With this assumption, analytical models of the pressure distribution inside the compression chamber and the pressure-density relationship for a large square baler were developed using the theory of elasticity.

In general, the constitutive relationship for an isotropic linear elastic material (Fig. 3.1) is characterized by modulus of elasticity (E) and Poisson's ratio (v). Either stress can be expressed as a function of strain or strain as a function of stress using the following equations (Fung 1977):

$$\sigma_{ij} = \frac{E}{1+\nu}\varepsilon_{ij} + \frac{E\nu}{(1+\nu)(1-2\nu)}\delta_{ij}\varepsilon_{kk}, \tag{3.1}$$

or

$$\varepsilon_{ij} = \frac{1+\nu}{E}\sigma_{ij} - \frac{\nu}{E}\delta_{ij}\sigma_{kk}, \tag{3.2}$$

where:

i = *x, y, or z,*

j = *x, y, or z,*

k = *x, y, or z,*

δ_{ij} = Kronecker delta with the following definition:

δ_{ij} = 1 if $i = j$ and

δ_{ij} = 0 if $i \neq j$.

Considering the normal stresses only and substituting $\sigma_{ii} = -P_i$ and $\varepsilon_{ii} = -\varepsilon_i$ where $i = x, y,$ and z (Fig. 3.2) the following equations can be derived between pressure and compressive strain of an element of the bale in different directions:

$$\varepsilon_x = \frac{1}{E}\left[P_x - \nu\left(P_y + P_z\right)\right] \qquad \text{in } x\text{-direction,} \tag{3.3}$$

$$\varepsilon_y = \frac{1}{E}\left[P_y - \nu\left(P_x + P_z\right)\right] \qquad \text{in } y\text{-direction and} \tag{3.4}$$

$$\varepsilon_z = \frac{1}{E}\left[P_z - \nu\left(P_x + P_y\right)\right] \qquad \text{in } z\text{-direction.} \tag{3.5}$$

These relationships only valid for an isotropic linear elastic element.

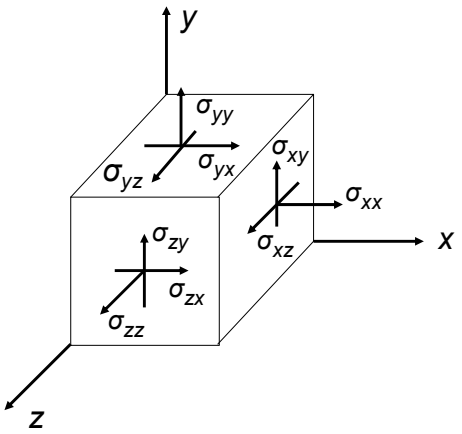

Figure 3.1 Stress tensor on an element of an isotropic linear elastic material.

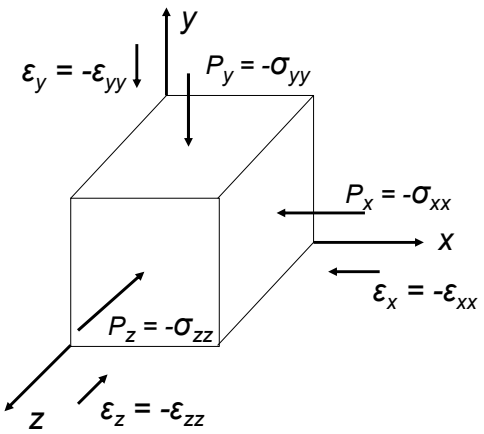

Figure 3.2 Normal stresses applied to an element of the bale inside the compression chamber.

From Eqs. 3.3, 3.4, and 3.5, ε_x, P_y, and P_z can be calculated in terms of P_x, ε_y, and ε_z as follows:

$$\varepsilon_x = \frac{(1+\nu)(1-2\nu)}{E(1-\nu)} P_x - \frac{\nu}{(1-\nu)}\left(\varepsilon_Y + \varepsilon_Z\right), \tag{3.6}$$

$$P_y = \frac{\nu}{1-\nu} P_x + \frac{E}{(1-\nu^2)}\left(\varepsilon_Y + \nu\varepsilon_Z\right) \text{ and} \tag{3.7}$$

$$P_z = \frac{\nu}{1-\nu} P_x + \frac{E}{(1-\nu^2)}\left(\nu\varepsilon_Y + \varepsilon_Z\right). \tag{3.8}$$

Volume change of element is also stated in terms of either strains or stresses using the following equation:

$$\frac{\Delta V}{V} \cong \varepsilon_x + \varepsilon_y + \varepsilon_z = \frac{1-2\nu}{E}\left(P_x + P_y + P_z\right). \tag{3.9}$$

A general form of the equation of equilibrium for an isotropic linear elastic material is given as follows:

$$\frac{\partial \sigma_{ij}}{\partial j} + b_i = 0 . \tag{3.10}$$

Since body forces (b_i) are assumed to be zero, the following equations result from Eq. 3.10:

$$\frac{\partial \sigma_{xx}}{\partial x} + \frac{\partial \sigma_{xy}}{\partial y} + \frac{\partial \sigma_{xz}}{\partial z} = 0 , \tag{3.11}$$

$$\frac{\partial \sigma_{xy}}{\partial x} + \frac{\partial \sigma_{yy}}{\partial y} + \frac{\partial \sigma_{yz}}{\partial z} = 0 \text{ and} \tag{3.12}$$

$$\frac{\partial \sigma_{xz}}{\partial x} + \frac{\partial \sigma_{yz}}{\partial y} + \frac{\partial \sigma_{zz}}{\partial z} = 0 . \tag{3.13}$$

From Figures 3.3 and 3.4, a_x and b_x (variable height and width of compression chamber as a function of the distance from the plunger) are defined using the following equations:

$$a_x = a - \alpha x , \tag{3.14}$$

$$b_x = b - 2\beta x , \tag{3.15}$$

where:

a = maximum height of compression chamber (cm) and

b = maximum width of compression chamber (cm).

Furthermore, according to the geometry of the compression chamber, the following assumptions can be made:

$$-\varepsilon_y = \frac{\alpha x}{a} = \varepsilon_y(x) \text{ and} \tag{3.16}$$

$$-\varepsilon_z = \frac{2\beta x}{b} = \varepsilon_z(x) . \tag{3.17}$$

Equations 3.16 and 3.17 state that the strains in the *y*- and *z*-directions are solely a function of x. Therefore, based on Eqs. 3.6, 3.7, and 3.8, the strain in *x*-direction and the pressures in *y*- and *z*-directions are also functions of *x* only if the variation of P_x with respect to *y* and *z* is zero. σ_{yz} is also assumed to be zero which is a reasonable assumption. Therefore, the following equations result from Eqs. 3.11, 3.12, and 3.13:

$$\frac{\partial \sigma_{xx}}{\partial x} + \frac{\partial \sigma_{xy}}{\partial y} + \frac{\partial \sigma_{xz}}{\partial z} = 0, \tag{3.18}$$

$$\frac{\partial \sigma_{xy}}{\partial x} = 0 \text{ and} \tag{3.19}$$

$$\frac{\partial \sigma_{xz}}{\partial x} = 0. \tag{3.20}$$

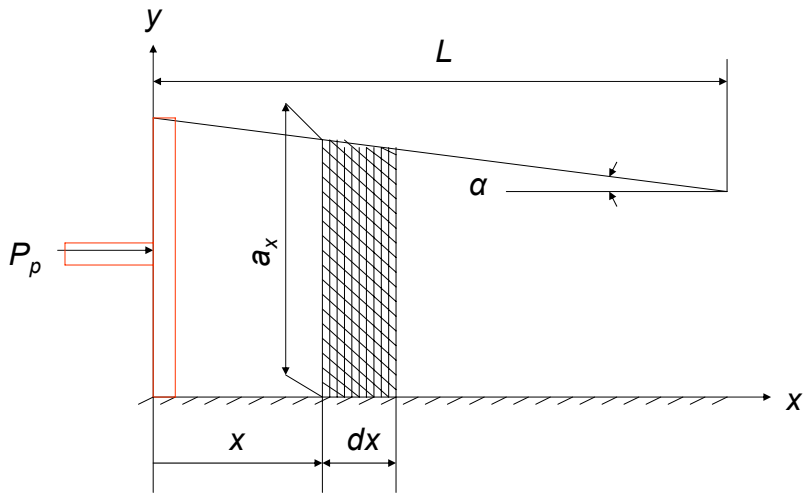

Figure 3.3 Side view of the compression chamber of a large square baler.

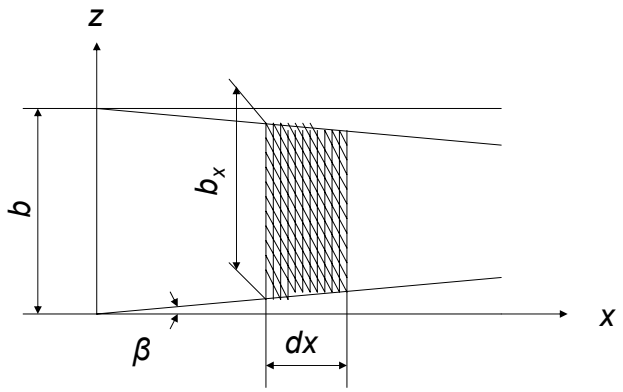

Figure 3.4 Top view of the compression chamber of a large square baler.

Equations 3.19 and 3.20 show that σ_{xy} and σ_{xz} are only functions of y and z, so they do not appear in the equation of equilibrium in the x-direction. Therefore, the stresses on the wedge part of an element of elastic material resemble what are shown in Fig. 3.5. Based on this free body diagram, the equations of equilibrium in the x- and y-directions are as follows:

$$\left(\sigma_x \Delta x \tan\alpha + \sigma_{xy}\Delta x\right) b_x - \left(\sigma_n \frac{\Delta x \sin\alpha}{\cos\alpha} + \tau_n \frac{\Delta x \cos\alpha}{\cos\alpha}\right) b_x = 0 \text{ and} \tag{3.21}$$

$$-\left(\sigma_y \Delta x + \sigma_{xy}\Delta x \tan\alpha\right) b_x + \left(\sigma_n \frac{\Delta x \cos\alpha}{\cos\alpha} - \tau_n \frac{\Delta x \sin\alpha}{\cos\alpha}\right) b_x = 0\,. \tag{3.22}$$

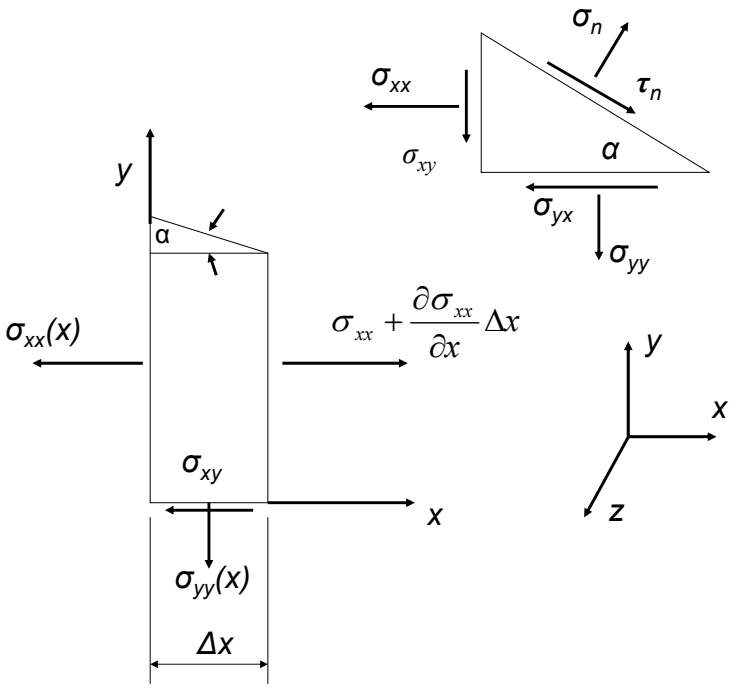

Figure 3.5 Stresses applied on the wedge part of an elastic material.

From Eqs. 3.21 and 3.22, σ_n and τ_n could be calculated as follows:

$$\sigma_n = \sigma_x \sin^2 \alpha + \sigma_y \cos^2 \alpha + \sigma_{xy} \sin 2\alpha \text{ and} \tag{3.23}$$

$$\tau_n = \left(\frac{\sigma_x - \sigma_y}{2} \right) \sin 2\alpha + \sigma_{xy} \cos 2\alpha . \tag{3.24}$$

Comparing these stresses to pressures applied to an element of the bale in bale chamber (Fig. 3.6), the following relationships could be found:

$$P_n = -\sigma_n = P_x \sin^2 \alpha + P_y \cos^2 \alpha - \sigma_{xy} \sin 2\alpha \text{ and} \tag{3.25}$$

$$\tau_f = -\tau_n = \mu P_n = \left(\frac{P_x - P_y}{2} \right) \sin 2\alpha - \sigma_{xy} \cos 2\alpha . \tag{3.26}$$

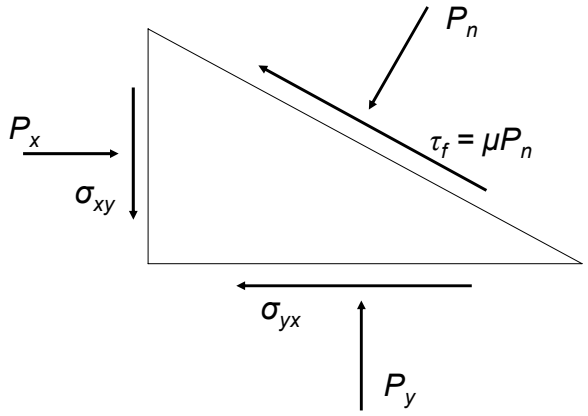

Figure 3.6 Pressures applied on the wedge part of an element of the bale.

Using Eqs. 3.25 and 3.26, σ_{xy} and P_n can be calculated in terms of μ, α, P_x, and P_y as follow:

$$\sigma_{xy} = \left[\frac{P_x\left(2\mu\sin^2\alpha + \sin 2\alpha\right) + P_y\left(2\mu\cos^2\alpha - \sin 2\alpha\right)}{2\left(\mu\sin 2\alpha - \cos 2\alpha\right)} \right] \quad \text{and} \tag{3.27}$$

$$P_n = P_x \sin^2\alpha + P_y \cos^2\alpha - \left[\frac{P_x\left(2\mu\sin^2\alpha + \sin 2\alpha\right) + P_y\left(2\mu\cos^2\alpha - \sin 2\alpha\right)}{2\left(\mu\sin 2\alpha - \cos 2\alpha\right)} \right] \sin 2\alpha \,. \tag{3.28}$$

Since in the large square baler, α is very small (α<<1rad) the following assumptions can be made:

$$P_n \approx P_y \quad \text{and} \tag{3.29}$$

$$\tau_f \approx -\sigma_{xy} = \mu P_n . \tag{3.30}$$

Therefore, there are only two components of stresses on the inclined surface of the element (both top and side inclined surfaces). The normal stress which equals to P_y for top surface and to P_z for side surfaces, and the shear stress which equals to μP_y for top surface and to μP_z for side surfaces, respectively. In Sitkei's model (Eq. 2.19), it has been assumed that only the top wall of the bale chamber made an angle of α with the *x*-axis (longitudinal axis), and the rest are parallel to the *x*-axis. Therefore, this model has been derived by assuming zero strain in the *z*-direction. In the large square baler, the top wall makes an angle of α and the side walls make angle of β with the *x* axis (Figures 3.3 and 3.4). In other words, the strain in none of the directions is zero. In order to derive an equation for the pressure distribution inside the bale along the length of the compression chamber, the equation of equilibrium of an element of bale shown in Figure 3.7 in the *x*-direction is considered as follows:

$$\sum F_x = 0 \text{ and} \tag{3.31}$$

$$\begin{aligned} &P_x A_x - (P_x + dP_x)(A_x + dA_x) - \frac{P_n{}^y dxb_x \sin\alpha}{\cos\alpha} - \frac{\tau_f{}^y dxb_x \cos\alpha}{\cos\alpha} - \tau_b dxb_x \\ &- \frac{2P_n{}^z dxa_x \sin\beta}{\cos\beta} - \frac{2\tau_f{}^z dxa_x \cos\beta}{\cos\beta} = 0 \end{aligned} . \tag{3.32}$$

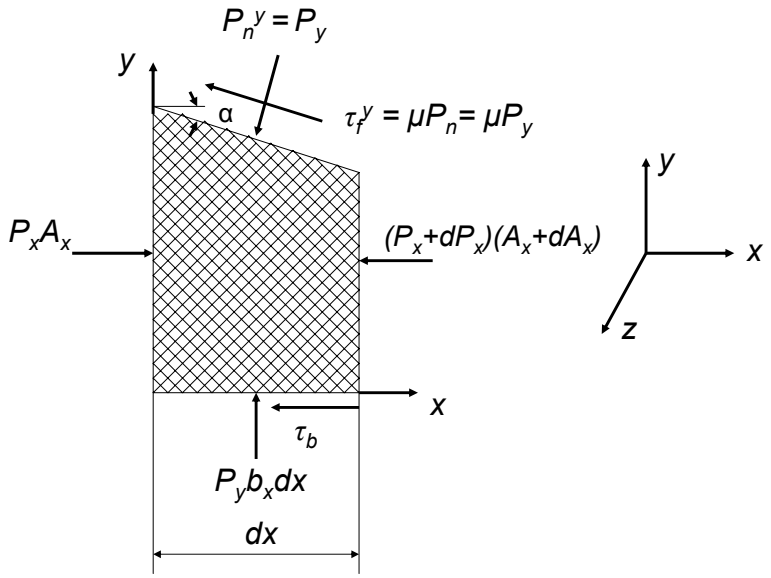

Figure 3.7 Applied forces to an element of the bale in the compression chamber.

Since α and β are small, the following assumptions can be made:

$\sin\alpha = \tan\alpha = \alpha$,

$\sin\beta = \tan\beta = \beta$,

$\cos\alpha = \cos\beta = 1$,

$P_n^{\ y} = P_y$,

$\tau_n^{\ y} = \mu P_y$,

$P_n^{\ z} = P_z$,

$\tau_n^{\ z} = \mu P_z$ and

$\tau_b = \mu P_y$.

By considering the above assumptions, Eq. 3.32 can be written as:

$$\frac{d(P_x A_x)}{dx} + P_y b_x(\alpha + 2\mu) + 2P_z a_x(\beta + \mu) = 0\,. \tag{3.33}$$

By inserting P_y and P_z from Eqs. 3.7 and 3.8 into Eq. 3.33, the following equation is obtained:

$$\begin{aligned}&\frac{d(P_x A_x)}{dx} + \frac{P_x \nu}{1-\nu}\left[b_x(\alpha + 2\mu) + 2a_x(\beta + \mu)\right] \\ &+ \frac{E}{1-\nu^2}\left[b_x(\alpha + 2\mu)(\varepsilon_y + \nu\varepsilon_z) + 2a_x(\beta + \mu)(\varepsilon_z + \nu\varepsilon_y)\right] = 0\end{aligned} \tag{3.34}$$

By inserting ε_y and ε_z from Eqs. 3.16 and 3.17 into Eq. 3.34, the following equation can be written:

$$\begin{aligned}&\frac{d(P_x A_x)}{dx} + \frac{P_x A_x \nu}{1-\nu}\left[\frac{(\alpha + 2\mu)}{a_x} + \frac{2(\beta + \mu)}{b_x}\right] \\ &+ \frac{EA_x}{1-\nu^2}\left[\frac{(\alpha + 2\mu)}{a_x}\left(\frac{\alpha}{a} + \frac{2\nu\beta}{b}\right) + \frac{2(\beta + \mu)}{b_x}\left(\frac{2\beta}{b} + \frac{\nu\alpha}{a}\right)\right]x = 0\end{aligned} \tag{3.35}$$

In order to simplify the problem, the mean values of A_m, a_m, and b_m are used instead of variable values of A_x, a_x, and b_x according to the following definitions:

$a_x \approx a_m = a - \alpha(L/2)$,

$b_x \approx b_m = b - 2\beta(L/2)$ and

$A_x \approx A_m = a_m b_m$.

Therefore the following differential equation can be written for the pressure in the x-direction:

$$\frac{dP_x}{dx}+\frac{\nu}{1-\nu}\left[\frac{\alpha+2\mu}{a_m}+\frac{2(\mu+\beta)}{b_m}\right]P_x+ E\left[\frac{b_m(\alpha+2\mu)(\alpha b+2\beta\nu a)+2a_m(\beta+\mu)(\alpha\nu b+2\beta a)}{aba_mb_m(1-\nu^2)}\right]x=0 \tag{3.36}$$

In Sitkei's model (Eq. 2.19), the modulus of elasticity (E) has been considered as a function of the strain in y-direction, while the results of the experiments in this study showed that E was constant for the density range encountered in the large square baler. Therefore, a constant E was considered in this model. By reducing the constant coefficients of the above differential equation to A and B using the following relationships (Eqs. 3.38 and 3.39), the differential equation can be written in a simple form of Eq. 3.37.

$$\frac{dP_x}{dx}+AP_x+Bx=0, \tag{3.37}$$

where:

$$A=\frac{\nu}{1-\nu}\left[\frac{\alpha+2\mu}{a_m}+\frac{2(\mu+\beta)}{b_m}\right], \tag{3.38}$$

$$B=E\left[\frac{b_m(\alpha+2\mu)(\alpha b+2\beta\nu a)+2a_m(\beta+\mu)(\alpha\nu b+2\beta a)}{aba_mb_m(1-\nu^2)}\right], \tag{3.39}$$

P_x = pressure in the x-direction at the distance x from the full extension point of plunger (kPa),

L = compression chamber length (cm),

x = distance from the full extension point of the plunger along the compression chamber length (cm),

α = angle of top wall of compression chamber with respect to x-axis,

β = angle of side wall of compression chamber with respect to x-axis,

μ = coefficient of friction between forage and compression chamber wall,

ν = Poisson's ratio,

a = maximum height of compression chamber (cm) and

b = maximum width of compression chamber (cm).

Equation 3.39 is a first order linear differential equation. The solution of this equation with the boundary condition of $P_x = P_p$ at $x = 0$ (pressure on the plunger is P_p) could be written as:

$$P_x = P_p e^{-Ax} + \frac{B}{A^2}\left(1 - Ax - e^{-Ax}\right). \tag{3.40}$$

A and B as are expressed in Eqs. 3.38 and 3.39 are functions of compression chamber geometry and forage material properties. In order to evaluate the effect of these parameters (α, β, μ, υ, and cross-section area) on the constants A and B and consequently on the pressure distribution, a compression chamber with a square cross-section is assumed for simplification ($a = b$ and $a_m = b_m$). Therefore, A and B could be written as follows:

$$A = \frac{\nu}{a_m(1-\nu)}\left(\alpha + 4\mu + 2\beta\right), \tag{3.41}$$

$$B = E\left[\frac{(\alpha + 2\mu)(\alpha + 2\beta\nu) + 2(\beta + \mu)(\alpha\nu + 2\beta)}{aa_m(1-\nu^2)}\right], \tag{3.42}$$

According to Eqs. 3.41 and 3.42, A and B increase with increasing α, β, μ, and υ, while they decrease with increasing cross-section area (a and a_m). Therefore, pressure in the x-direction drops off faster with increasing wall angles, coefficient of friction, and

Poisson's ratio, whereas with an increasing cross-section area it drops off more slowly. If a compression chamber with no converged walls is considered ($\alpha = \beta = 0$), constant B will disappear and constant A will be only function of coefficient of friction, Poisson's ratio, and chamber cross-section area. This shows that the second term of Eq. 3.40 comes from the walls convergence. Equation 3.40 expresses the pressure distribution inside the compression chamber of a baler along the axis of compression (x-direction) as a function of crop properties, bale dimensions, and the distance from the full extension point of the plunger. Using Eqs. 3.7, 3.8, and 3.40, the following equations can be derived for pressures in the y- and z-directions (P_y and P_z):

$$P_y = \frac{\nu}{1-\nu}\left[P_p e^{-Ax} + \frac{B}{A^2}\left(1 - Ax - e^{-Ax}\right)\right] + E\left[\frac{b\alpha + 2a\nu\beta}{ab\left(1-\nu^2\right)}\right]x \text{ and} \tag{3.43}$$

$$P_z = \frac{\nu}{1-\nu}\left[P_p e^{-Ax} + \frac{B}{A^2}\left(1 - Ax - e^{-Ax}\right)\right] + E\left[\frac{2a\beta + b\nu\alpha}{ab\left(1-\nu^2\right)}\right]x. \tag{3.44}$$

According to Eqs. 3.43 and 3.44, on the plunger ($x = 0$) the following relationships exist between pressures in the x-, y-, and z-directions (P_p is pressure in the x-direction at $x = 0$):

$$P_y(0) = P_z(0) = \left(\frac{\nu}{1-\nu}\right)P_p = \left(\frac{\nu}{1-\nu}\right)P_x(0). \tag{3.45}$$

Therefore, the Poisson's ratio (v) can be calculated using Eq. 3.45 as follows:

$$\nu = \frac{P_y(0)}{P_y(0) + P_x(0)} = \frac{P_z(0)}{P_z(0) + P_x(0)}. \tag{3.46}$$

The developed analytical model for pressure distribution in this study was validated using collected data for barley straw, wheat straw, and whole green barley. The least-

square regression analysis method was used for model validation, and model constant coefficients were estimated.

3.1.1.2 Empirical Model

The analytical model for the pressure distribution is a complicated model with many parameters. These parameters which are related to the compression chamber dimensions or forage material physical and mechanical properties have to be measured prior to the modeling process. Measuring these parameters is usually a time-consuming exercise (requires a lot of time) and is very expensive. So, in addition to the analytical model, an empirical model was also introduced for the pressure distribution in the *x*- and *y*-directions for the tested forage materials using the experimental data. According to the pattern of the experimental data, an exponential model with unknown constants was considered for each of the materials. The least square error in the regression analysis was used to validate the model and estimate the model parameters. The general form of the presented models was the same for the all tested forage materials, while the model constants differed from material to material. The following is the general form of the model in the *x*-direction for the tested forage materials:

$$P_x = A_0 e^{-B_0 x}, \tag{3.47}$$

where:

P_x = pressure in the *x*-direction as a function of distance from the full extension point of the plunger (kPa),

x = distance from the full extension point of the plunger along the compression chamber length (cm) and

A_0, B_0 = model coefficients.

Because the dug hole in the bale for the sensor was usually larger than the sensor size, there was a gap between the sensor body and the top and side walls of the dug hole. In practice, some of the forces applied in the *y*-direction have been consumed to fill this gap. Since filling this gap takes some time, at the beginning of the force recording process (near the plunger), the recorded forces in the *y*-direction were much lower than the expected forces. However, the recorded forces at the end of the compression chamber were much closer to the expected forces. Therefore, the values of forces recorded in the *y*-direction were not reliable (especially near the plunger), however the trend of force changing with distance from the plunger showed the force distribution pattern inside the compression chamber in the *y*-direction. After converting the recorded forces to pressure, the following exponential model was fitted to the experimental data of barley straw, wheat straw, and whole green barley in the *y*-direction:

$$P_y = Ce^{-D_0 x} \tag{3.48}$$

where:

P_y = pressure in the *y*-direction at the distance *x* from the full extension point of plunger (kPa),

x = distance from the full extension point of the plunger along the compression chamber length (cm) and

C, D_0 = model coefficients.

The designed sensor was not able to record the forces in the *z*-direction (section 3.3.2.2); therefore, there were no data available in the *z*-direction to model the pressure distribution in this direction.

3.1.2 Pressure-Density Relationship

3.1.2.1 Analytical Model

It is also important to find a relationship between bale density and applied pressure to the bale. Bale density changes during the baling process along the bale length because of changing bale volume. Bale volume change is related to the pressures in different directions given by Eq. 3.9. An analytical model can be derived by inserting P_y and P_z from Eqs. 3.7 and 3.8 into Eq. 3.9 as follows:

$$\frac{\Delta V}{V_0} = \frac{1-2\nu}{E}\left(P_x + \frac{2\nu}{1-\nu} P_x + \frac{E}{1-\nu}\left(\varepsilon_y + \varepsilon_z\right)\right) . \tag{3.49}$$

On the other hand, the relationship between volume change and density is expressed by:

$$\frac{\Delta V}{V_0} = 1 - \frac{V}{V_0} = 1 - \frac{\gamma_0}{\gamma_x} , \tag{3.50}$$

where:

ΔV = bale volume change (m^3),

V_0 = bale initial volume (m^3),

V = bale volume as a function of distance from the full extension point of the plunger (m^3),

γ_x = bale density as a function of distance from the full extension point of the plunger (kg/m^3) and

γ_0 = initial bale density (kg/m^3).

By equating the right hand sides of Eqs. 3.49 and 3.50, and using Eqs. 3.16 and 3.17, the following equation can be obtained:

$$1-\frac{\gamma_0}{\gamma_x}=\frac{P_x(1-2\nu)(1+\nu)}{E(1-\nu)}+\frac{1-2\nu}{1-\nu}\left(\frac{b\alpha+2a\beta}{ab}\right)x. \tag{3.51}$$

After simplifying Eq. 3.51, the following model can be developed for the bale density as a function of pressure, crop properties, and compression chamber dimensions:

$$\gamma_x=\frac{\gamma_0 Eab(1-\nu)}{Eab(1-\nu)-(1-2\nu)[abP_x(1+\nu)+E(b\alpha+2a\beta)x]}. \tag{3.52}$$

At the plunger ($x = 0$), P_x is equal to P_p; therefore, γ_p which is the bale density in front of the plunger is calculated from the following equation:

$$\gamma_p=\frac{\gamma_0 E(1-\nu)}{E(1-\nu)-(1-2\nu)(1+\nu)P_p}. \tag{3.53}$$

3.1.2.2 Empirical Model

Developing an empirical model for the relationship between the bale density and plunger pressure in a large square baler was one of the objectives of this study. In order to establish this model, the data of baling alfalfa and barley straw at different load settings were used. In these tests, plunger forces were recorded by strain gages, and densities were calculated by measuring bale dimensions and weight. Different models have been introduced for the pressure-density relationship of forage materials, where some of them were tested with the data of this experiment to find the best model for the pressure-density relationship. The most promising model for the purpose of this study was the model (Eq. 2.16) suggested by Ferrero et al. (1990). Thus, this model was modified to show the best agreement with the experimental data of the relationship between alfalfa and barley straw bale density and plunger pressure. Therefore, the

pressure-density relationship for the large square baler during the alfalfa and barley straw baling process was best expressed with the following model:

$$\gamma_s = \gamma_0 + (A_0 + B_0 P_p + C P_p^{\,2})(1 - e^{-D_0 P_p}), \tag{3.54}$$

where:

γ_s = material bulk density (kg/m^3),

γ_0 = initial bulk density (kg/m^3),

P_p = compression pressure on the plunger (MPa) and

A_0, B_0, C, D_0 = model coefficients.

Comparison of the analytical and empirical models for bale density as a function of pressure on plunger, P_p, (Eqs. 3.52 and 3.53) shows that these models have completely different general forms, however both models reveal that bale density has a direct relationship with material initial density and plunger pressure.

3.2 Large Square Baler

In this project, a newly designed New Holland BB960 large square baler (Fig. 3.8) was used to bale alfalfa, whole green barley, barley straw, and wheat straw. This baler produces bales with a width of 1.2 m, height of 0.9 m, and an adjustable length of up to 2.5 m. A schematic of the large square baler and its components is shown in Figure 3.9. A large square baler has a two-stage feeding system (Figs. 3.10 and 3.11). After being lifted by the pickup (1), the centering augers guide the crop to the packer chamber throat opening, where it is swept into the pre-compression chamber by a set of packer fingers (2) mounted on a triple throw crankshaft, giving the packer a

Figure 3.8 New Holland BB960 large square baler.

raking action that mixes the crop and ties the flake together as it feeds into the fixed-volume pre-compression chamber (3). The holding fingers (4) retain the charge in the chamber until the crop density reaches a predetermined level. At this point, the pre-compression forks (5) engage to sweep the preformed flake into the bale chamber where it is compressed by the plunger (6) into the compression chamber (7). Since one charge makes one complete flake, bale density is always consistent throughout the bale with all sides being well formed regardless of crop conditions or ground speed. This is especially important when baling light swaths on rough ground. Conversely, balers without pre-chambers must be driven at high speed to attempt to maintain flake content and bale shape.

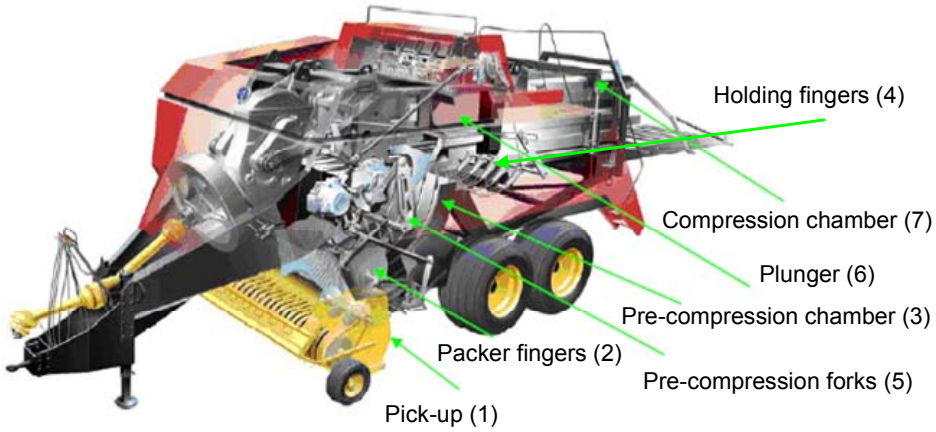

Figure 3.9 Cross-view of a CNH large square baler (courtesy of CNH).

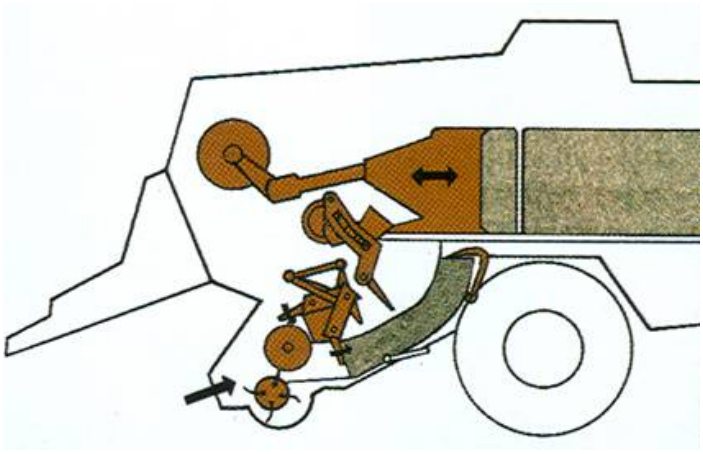

Figure 3.10 Packing the pre-compression chamber (courtesy of CNH).

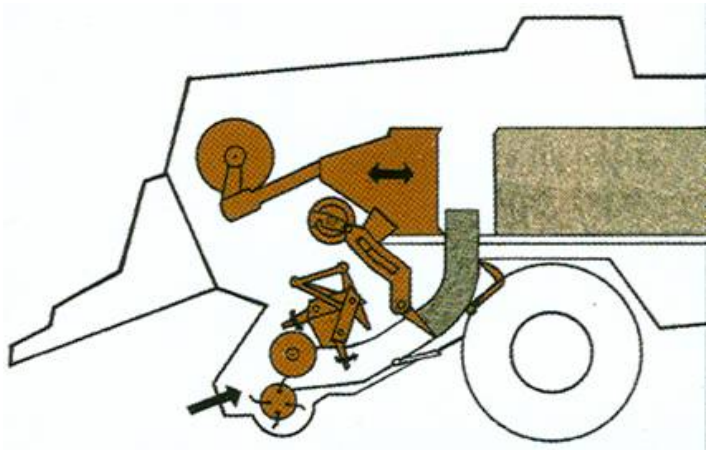

Figure 3.11 Filling the main compression chamber (courtesy of CNH).

The bale density control system in the large square baler could be used in three different modes. The first mode is called the automatic bale density control mode. The baler should work normally in this mode to produce bales with a uniform bale density close to the pre-set density by the operator. In this study, the baler was operated in the automatic mode, so only this mode is explained in this section. In this mode, the plunger force sensor senses the force applied to the bale via the plunger, and a processor sets the pressure in the bale density controlling system to adjust the bale density based on plunger force. A density level is selected in this mode by an operator from the tractor cab based on the crop type and moisture content. This mode can compensate for the variation in the baling material conditions such as moisture content, so that the pressure in the density cylinders changes to keep the plunger load and the bale density constant. The available settings are 10, 20, 30, up to 100% of the maximum available plunger force, and by changing the load setting; the side hydraulic cylinders adjust the applied

forces to the top and side walls in such a way that the baler applies a resistance equal to the requested force to the plunger (New Holland BB960 Manual 2001).

There is also a pre-compression chamber that is located prior to the main compression chamber so that the forage materials are compressed at an adjustable pressure before entering the main chamber. The packer charges the forage materials continuously into this chamber; when enough material is charged into the pre-compression chamber and the pressure in the pre-compression chamber is exceeded from the stuffer trip setting (this setting sets the size of the flake charged into the bale chamber), the sensor paddles are pushed down (Fig. 3.12). At this time, the stuffer drive is activated and the stuffer fork sends the material from the pre-compression chamber to the bale chamber when the plunger is doing its compression stroke. At the same time, the holding fingers open the top opening of the pre-compression chamber. Once the material flake is charged to the bale chamber, the holding fingers return to their original position (Fig. 3.13).

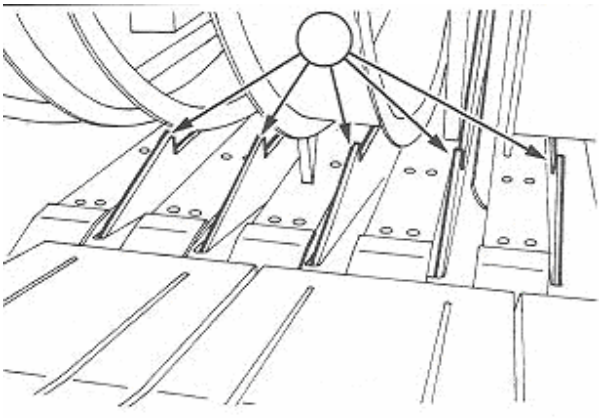

Figure 3.12 Sensors of the pre-compression chamber (New Holland BB960 Manual 2001).

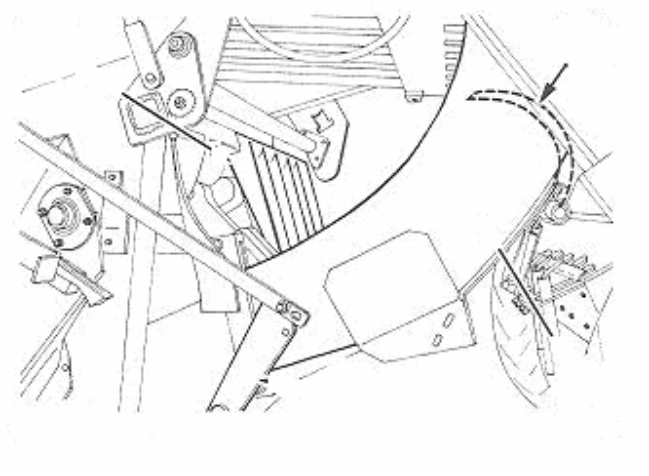

Figure 3.13 The holding fingers situation right after feeding the materials to the bale chamber (New Holland BB960 manual 2001).

There is a lever with ten positions to apply ten different pre-compression pressure levels to the materials which is called the stuffer trip sensitivity lever. This lever is connected to the pre-compression chamber sensor via a spring. Changing the lever position changes the spring tension and consequently changes the sensor sensitivity. The position of this lever determines the amount of materials fed to the bale chamber (flake size) in such a way that increasing the spring tension increases the flake size and decreasing the spring tension decreases the flake size. There are ten positions on this lever (one to ten) to choose ten different flake sizes. Lower positions give thinner flakes and higher positions give thicker flakes. Well-shaped dense bales should have a flake with the thickness of 60 to 80 mm; however, flake size depends on the sensor sensitivity.

3.3 Instrumentation Set up

In this section, sensor installation on the baler and sensor design are explained.

3.3.1 Sensor Installation

To record forces exerted to the baler plunger and different parts of the compression chamber walls, appropriate sensors were installed in different points of the baler. To measure the forces on the plunger, a set of four strain gages (EA-06-500BL-350, Microsoft Measurements, Raleigh, NC) were mounted on each arm of the plunger (Figs. 3.14 and 3.15). Strain gages were used in a Wheatstone bridge, and a data acquisition system was used to record the bridge outputs which were voltages at the frequency of 50 Hz (Fig. 3.16). Repeated loading-unloading procedure was carried out in the lab to calibrate the installed sensor.

Figure 3.14 Strain gages installed on the plunger arm.

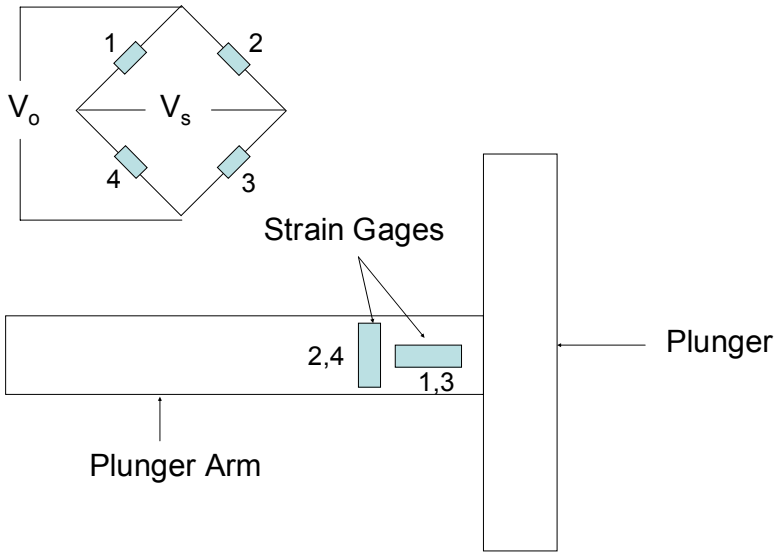

Figure 3.15 Arrangement of strain gages on the plunger arm and Wheatstone bridge (V_s and V_o are excitation and bridge output voltages, respectively).

To measure the top and side wall displacements during baling, a displacement sensor was mounted on each wall. The displacement sensor used a potentiometer linked to a rotary device that turned around its axis when pushed by an arm linked to the wall. A rolled plate created a spring effect to follow the wall displacement. The measured displacements were then used to calculate the top and side wall angles which appear in the analytical model of the pressure distribution inside the compression chamber.

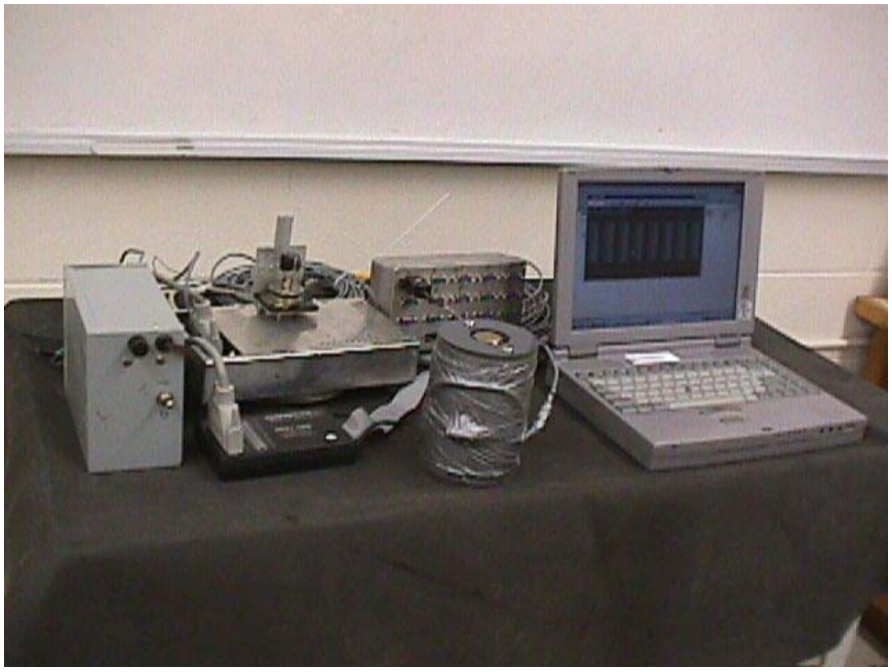

Figure 3.16 Data acquisition and monitoring system.

3.3.2 Sensor Design

The main purpose of the field experiments with the baler was to collect appropriate experimental data to validate the models of the pressure-density relationship and the pressure distribution inside the bale along the length of the compressing chamber. In order to achieve this goal, two types of measurement sensors were designed.

3.3.2.1 Uni-axial Sensor

The uni-axial sensor consisted of an S-shape load cell which was put inside a pipe as a cover (radius of 50 mm and total length of 150 mm) and fixed at one end. The other end was used as the area that senses the applied force (Fig. 3.17). The Instron testing machine (Instron Corp., Canton, MA) was used to calibrate this sensor (Fig. 3.18). This load cell was put inside the bale in the *x*-, *y*-, and *z*-directions to record the forces in those directions for alfalfa bales. The main problem with the uni-axial sensor

was that it was not able to record the forces in three directions simultaneously. In addition, because of the cylindrical shape of the sensor, the alignment with the corresponding axis inside the bale chamber was difficult.

Figure 3.17 Assembled uni-axial sensor (height is 150 mm).

Figure 3.18 Load cell calibration using the Instron testing machine.

3.3.2.2 Tri-axial Sensor

A tri-axial sensor was designed using two extended octagonal ring (EOR) which were put together as shown in Figure 3.19. The EOR was machined from aluminium 6061-T6 with yield strength of 275 MPa and Young's modulus of 70 GPa. A cube of six aluminum plates was used to cover the sensor and provide a suitable sensing area for the applied forces at different directions (Fig. 3.20). Therefore, the outside dimensions of the tri-axial sensor were: length of 210 mm, height of 160 mm, and width of 175 mm. *z*- and *y*-direction views of the sensor and applied forces to the covering plates of sensor are shown in Figures 3.21 and 3.22. The applied forces to the covering plates can be transferred to each of the EOR used in this sensor. Therefore, three forces (F_x, F_y, and F_z) and two moments (M_x and M_z) are applied to each EOR (Fig. 3.23). Since two

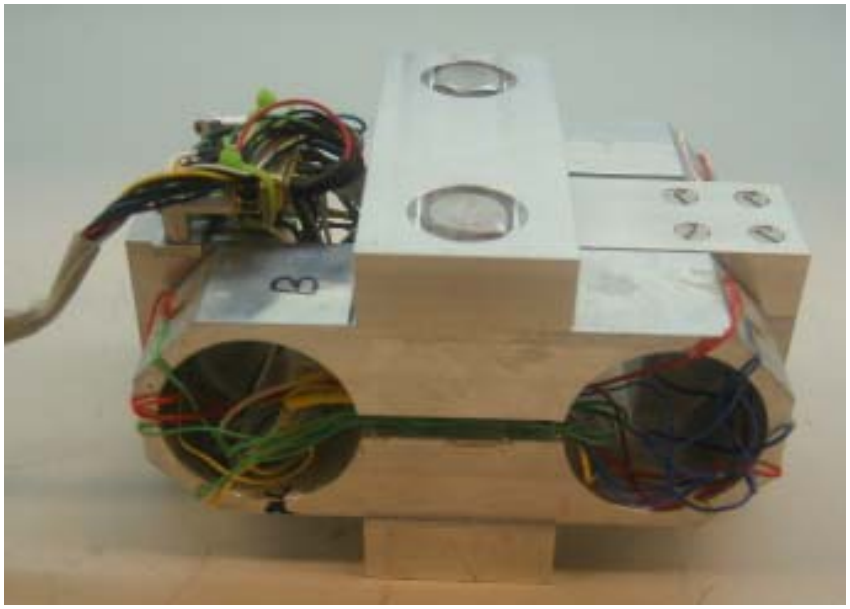

Figure 3.19 Designed sensor without cover plates (length of 163 mm, height of 110 mm, and width of 126mm).

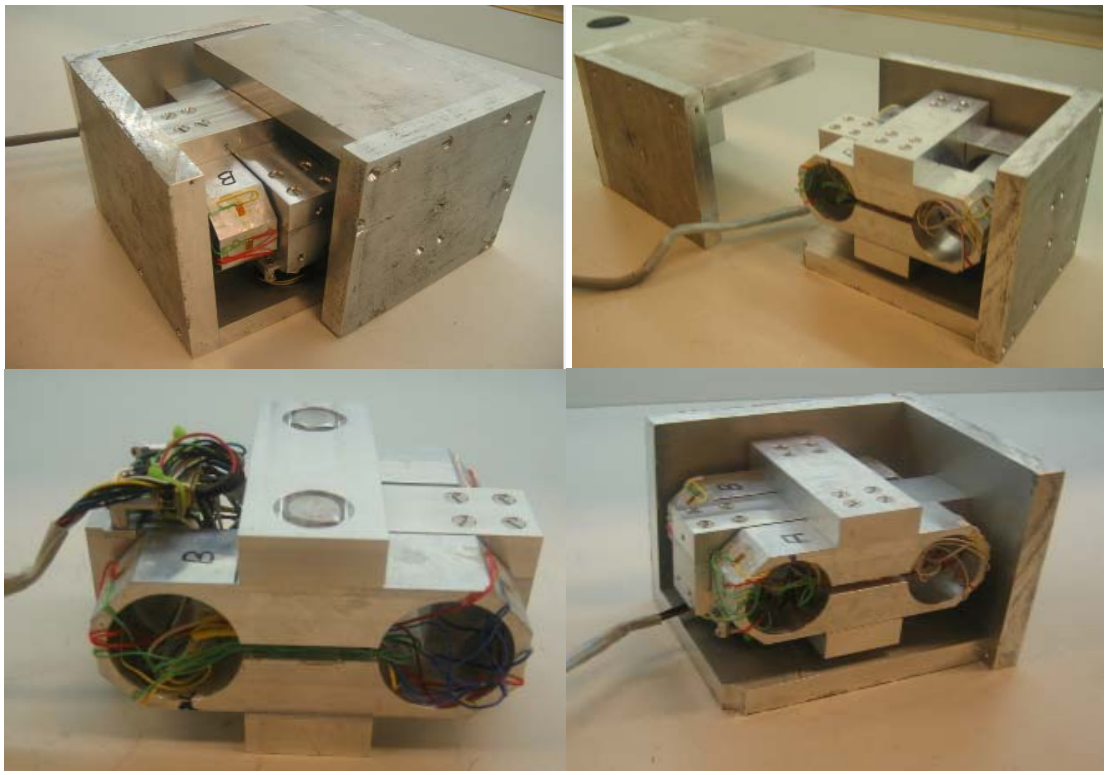

Figure 3.20 Different pictures of the designed tri-axial sensor (length of 210 mm, height of 160 mm, and width of 175 mm for the sensor with cover).

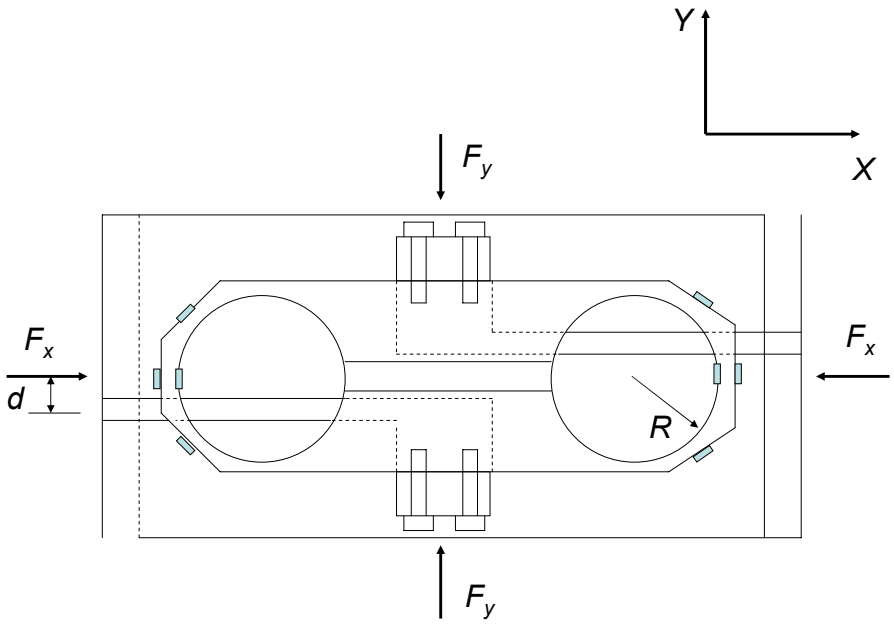

Figure 3.21 Applied forces to the covering plates of the sensor in the *x*-*y* plane.

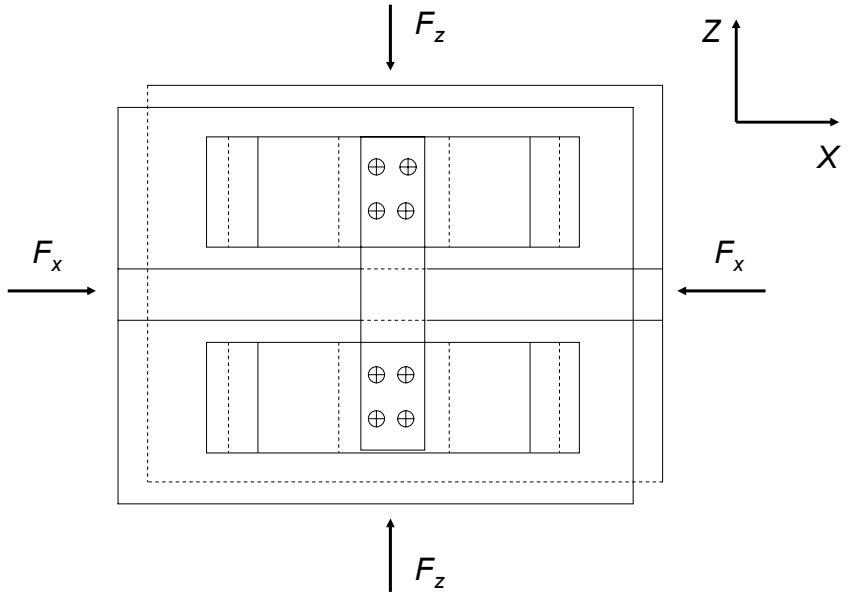

Figure 3.22 Applied forces to the covering plates of the sensor in the *x*-*z* plane.

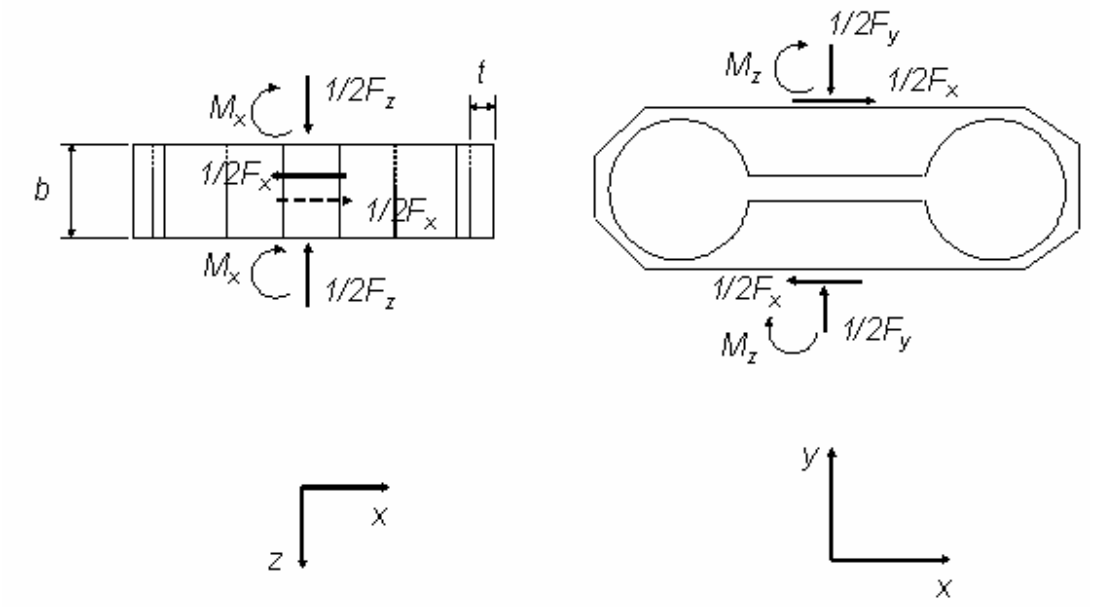

Figure 3.23 Forces transferred from covering plates to the extended octagonal ring in different directions.

EORs have been used in this sensor, half of the applied forces to the covering plates in each direction is applied to each EOR. The EOR consists of a rigid part and a flexible part (Fig. 3.24). The flexible part which is the ring section of the EOR, is used as a sensitive element to bending moment to measure the applied forces by installing strain gages on. The horizontal and vertical forces (F_x and F_y) and M_z apply bending moment at the ring section of the EOR; therefore, by installing strain gages at proper positions on this element, these forces can be measured simultaneously and independently. The bending moment at different angles of the ring section of this element is calculated from the following equation using mechanics of materials:

$$M_\theta = F_y \frac{R}{2}(\frac{2}{\pi} - \sin\theta) - F_x \frac{R}{2}\cos\theta, \tag{3.55}$$

where:

R = radius of the ring section (m),

θ = angle, measured clockwise from the top of the ring (radians),

M_θ = bending moment in ring at angular position θ (N m) and

F_x, F_y = applied load in the x and y-directions (N).

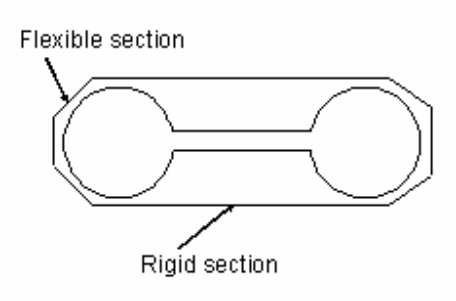

Figure 3.24 Flexible and rigid sections of the extended octagonal ring (EOR).

In order to measure forces in different directions simultaneously and independently with minimum cross sensitivities, proper positions of strain gages must be determined using Eq. 3.55. For measuring F_y, the angle of the location of strain gage must be selected in such a way that bending moment at that angle is only a function of F_y. Therefore, the second term of Eq. 3.55 should be zero:

$$F_x \frac{R}{2} \cos\theta = 0 . \tag{3.56}$$

From Eq. 3.56, θ is obtained to be 90°. So, strain gages should be installed at the angle of 90° clockwise from the top point of ring section to measure F_y without any side effects from F_x and F_z. For F_x measurement, the first term of Eq. 3.56 should be zero; therefore:

$$F_y \frac{R}{2}(\frac{2}{\pi} - \sin\theta) = 0 . \tag{3.57}$$

From Eq. 3.57, θ is calculated to be 39.5°. So, strain gages should be installed at the angle of 39.5° from the top point of the ring section to measure F_x without any side effects from F_y and F_z. Strain gages installed at these two angles are not affected by F_z, because F_z applies shear and torsion at those points which cannot be recorded by these strain gages. In order to measure F_z, the strain gages must be installed on the side faces of the ring section (Fig. 3.25).

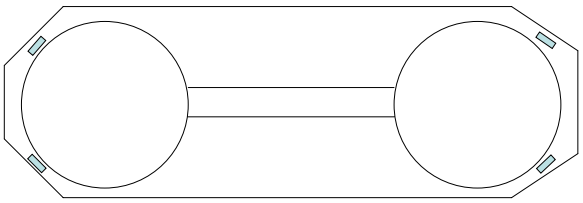

Figure 3.25 Positions of the strain gages on the EOR to record side forces.

Based on the above analysis of the strain gage position, the stress nodes of the EOR (Fig. 3.26) used in this sensor were selected at the positions of $\theta = \pm 39.50^{\circ}$ and $\theta = 90^{\circ}$ for axial and vertical force measurements, respectively. The radius of the ring section of the EOR (R) was considered 25 mm, because it was the smallest required

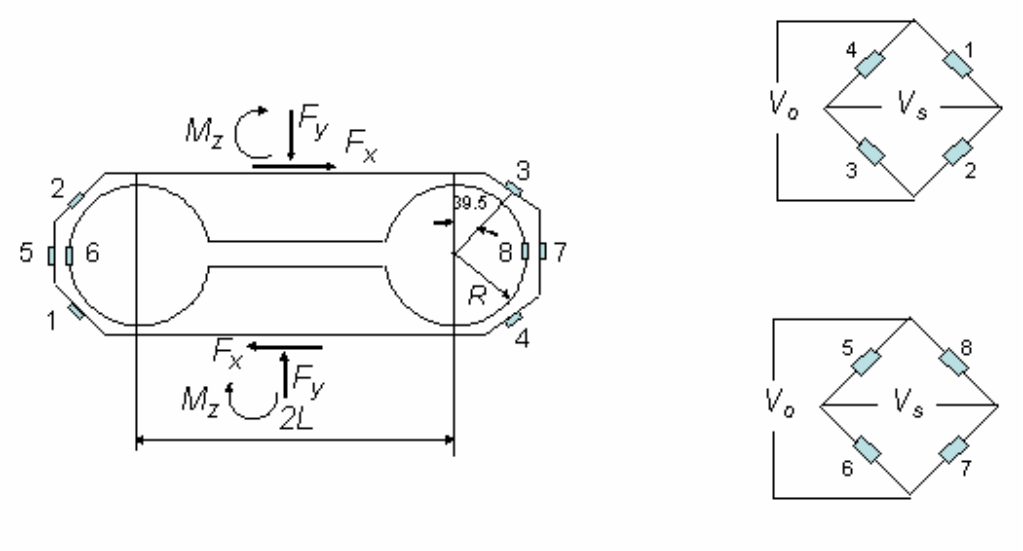

Figure 3.26 Stress nodes and strain gage locations in the extended octagonal ring. Bridge containing gages 1, 2, 3, and 4 is sensitive to F_x and the bridge containing gages 5, 6, 7, and 8 is sensitive to F_y.

size of the ring for strain gage installation. A ring width of at least 38 mm was needed to attach the horizontal force bracket to the EOR via four bolts. The ring center to center distance ($2L$) was chosen to be 100 mm, and a distance of 50 mm was also required between the two EORs. Based on these dimensions and a preliminary estimation of the maximum plunger pressure, the maximum applied force to the sensor in the x-direction was found to be about 9 kN. Therefore, the horizontal design load was considered to be

9 kN, and 56% of this load (5 kN) was selected as the vertical design load. According to the abovementioned dimensions and design loads, the ring thickness was then determined using Eq. 3.55 and the following equation from mechanics of materials:

$$\varepsilon_\theta = \frac{6(1-\nu^2)M_\theta}{Ew_r t^2}, \tag{3.58}$$

where:

w_r, t = ring width and thickness (m),

ε_θ = strain at angular position θ on the ring (m/m),

M_θ = bending moment in the ring at the angular position θ (N m),

ν = Poisson's ratio and

E = modulus of elasticity (Pa).

The maximum bending moment of the ring section was calculated using Eq. 3.55 then ring thickness was computed using Eq. 3.58. The allowable strain for aluminum 6061-T6 is 0.0039 m/m; therefore, based on this strain and the design loads, a ring thickness of 6.5 mm was obtained for the EOR. Once the ring thickness was determined, the ratio of the ring radius to the ring thickness (R/t) was calculated to make sure that the condition for the thin ring was satisfied. The designed EOR dimensions are shown in Table 3.1. A set of four strain gages were each installed at the positions of $\theta = \pm 39.5^\circ$ and $\theta = 90^\circ$ on the ring section of the EORs. Each set of these strain gages formed a full Wheatstone bridge so that there was one horizontal output and one vertical output for each of the EORs (Fig. 3.26). Therefore, the force in the *x*-direction was calculated from the sum of the horizontal outputs of the two EORs, and the force in the *y*-direction was computed from the sum of the vertical outputs.

Table 3.1 Dimensions of the EOR.

Parameter	Dimension (mm)
t (ring thickness)	6.5
w_r (ring width)	38
$2L$ (ring center to center distance)	100
h	6
r (ring radius)	25

3.3.2.3 Sensor Calibration

The uni-axial loading calibration was performed by applying forces in the *x*- and *y*-directions separately to determine the sensor vertical and horizontal primary, secondary, and cross sensitivities. Three directional calibration was also carried out by applying forces in the *x*-, *y*-, and *z*-directions to the sensor simultaneously. Independent forces in the *x*- and *y*-directions were applied using the Wykeham Farrance shear box apparatus and in the *z*-direction, force was applied by using a C-clamp. The applied force in the *z*-direction was measured by locating a small load cell between the C-clamp and the sensor wall (Figure 3.27). Four loading and three unloading points were considered for the three directional calibrations.

A data acquisition system including a data logger (PPIO-AI8), a signal conditioner (EXP16), a power supply, and a laptop were used to record the output of the sensor at the frequency of 50 Hz. The data of the three directional calibration were used to develop the multiple regression calibration equations to predict each of the forces in the *x*- and *y*-directions. The primary, the secondary, and the cross sensitivities for each

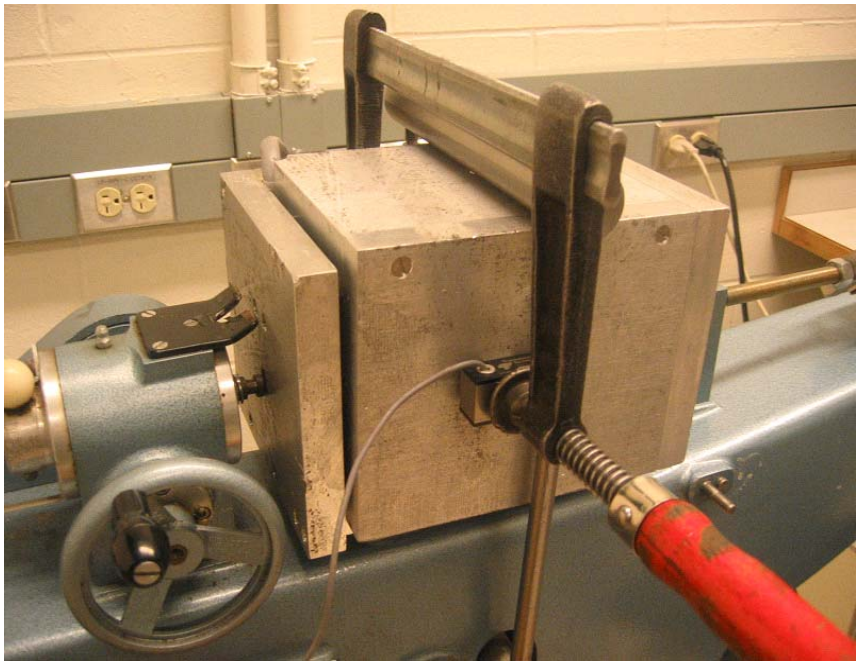

Figure 3.27 Sensor calibration using the Wykeham Farrance shear box apparatus and a C-clamp.

of the horizontal and the vertical loading were also computed using the data of the uni-axial calibration. In both cases of the sensors (the uni-axial and the tri-axial sensors), a potentiometer was used to measure the load cell position with respect to the baler plunger at each moment when it was moving to the back of the baler along with the bale (Fig. 3.28).

3.4 Field Experiments

The baler was tested in two different provinces of Canada in 2001 to collect appropriate data for the pressure-density relationship. First, it was tested in Saskatchewan in late June and early July with alfalfa then it was shipped to Québec and tested with barley straw in late July and early August. Data collection for the pressure

distribution model was performed in 2003 by baling whole green barley, barley straw, and wheat straw.

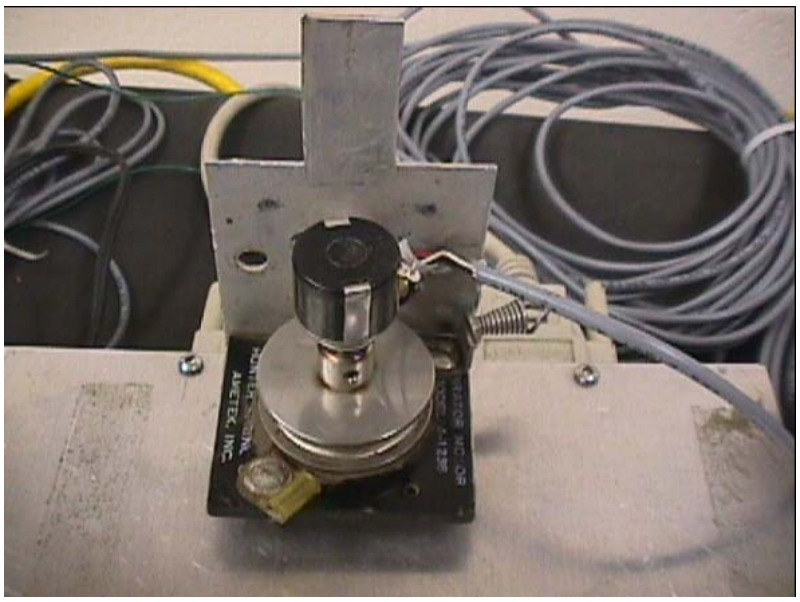

Figure 3.28 Displacement sensor used to measure the load cell position.

3.4.1 Pressure-Density of Alfalfa

The farm considered in Saskatchewan was located in Clavet, a town about 30 km southeast of Saskatoon. This field consisted of a quarter section (64 ha) of second year pure alfalfa. The first cut was done in late June and early July, and completed in three days. The effect of flake size and the load settings on the plunger force and the bale density was evaluated on this field. The equipped large square baler was used to bale alfalfa at 12.4% (wb) moisture content (Fig. 3.29). To determine the effect of flake size and the load setting on the plunger force and bale density, three levels of flake sizes (three positions of the sensitivity lever such as 3, 6, and 9 out of 10) and three levels of load settings (50, 60, and 70% of the available maximum plunger force) were

considered. Baling was performed at the constant forward speed of 8 km/h. The forces on the plunger arms were recorded by the data acquisition system. The average of the peak forces resulting from the sum of the forces on the two plunger arms was considered as the plunger force for each bale formation.

Figure 3.29 Baling pure alfalfa in Saskatchewan.

The actual bale bulk density was calculated by measuring the bale dimensions and weight (Fig. 3.30). Table 3.2 shows a sample of the raw data taken in this test. Moisture content of the material samples was determined using the ASAE standard S358.2 DEC 98 for forage materials (ASAE 2001). A split plot experimental design with three replications was established in the field to evaluate the effect of the main factor (load setting) and the sub factor (flake size) on the plunger force and the bale density. The SAS software (SAS Institute, Cary, NC) was used to analyze the data resulting from this experiment, and the treatment mean comparison was carried out using Duncan's multiple range tests. Finally, efforts were made to fit one of the pressure-density models which had been introduced in the literature to the data of the plunger pressures and the corresponding bale densities. None of the models discussed in the section 2.2.1 fitted

sufficiently well to the experimental data of this test; therefore, a modified empirical model was used to fit to the data of this experiment.

Figure 3.30 Bale weight measurement.

3.4.2 Pressure-Density of Barley Straw

In Québec, barley straw with 8.7% (wb) moisture content was baled in a 48 ha farm. To determine the effect of flake size and the load setting on the plunger force and bale density, three levels of flake sizes (three positions of the sensitivity lever like 3, 6, and 9 out of 10) and four levels of the load settings (40, 60, 80, and 100% of the available maximum plunger load) were considered (Fig. 3.31). Baling was performed at the constant forward speed of 15 km/h. The forces on the plunger arms were recorded by the data acquisition system. The average of the peak forces resulting from the sum of the forces on the two plunger arms was considered as the plunger force for each bale formation. The actual bale bulk density was calculated in the same manner as the alfalfa in Saskatchewan. A sample of raw data taken in this test is shown in Table 3.3.

Figure 3.31 Baling barley straw in Quebec.

Moisture content of the material samples was determined using the ASAE standard S358.2 DEC 98 for forage materials (ASAE 2001). The same experimental design, the statistics software, and the mean comparison test, used in the previous test, were also applied in this part of the study. At the end, an empirical model was fitted to the data of this experiment.

Table 3.2 Raw data from pressure-density tests for alfalfa.

Load Setting (%)	Flake size (lever position out of 10)	Plunger Force (kN)	Bale Density (kg/m^3)
50	3/10	261.4	151.9
50	3/10	240.3	158.4
50	3/10	235.9	151.9
50	3/10	256.6	160.5
50	6/10	273.7	156.2
50	6/10	243.0	156.2
50	6/10	262.9	156.9
50	6/10	271.9	156.2
50	9/10	261.3	152.9
50	9/10	269.3	154.9
50	9/10	283.2	150.8
50	9/10	248.1	150.8
60	3/10	297.9	159.7
60	3/10	288.8	159.7
60	3/10	302.2	168.4
60	3/10	306.4	157.5
60	6/10	329.6	162.7
60	6/10	298.0	161.2
60	6/10	308.9	158.5
60	6/10	293.8	166.8
60	9/10	320.3	162.2
60	9/10	314.8	162.2
60	9/10	325.0	160.7
60	9/10	308.3	166.4
70	3/10	359.9	175.6
70	3/10	365.1	175.6
70	3/10	366.6	182.9
70	3/10	351.4	178.0
70	6/10	366.9	188.4
70	6/10	391.0	185.9
70	6/10	347.8	183.4
70	6/10	366.9	180.9
70	9/10	384.9	184.8
70	9/10	384.5	189.8
70	9/10	381.1	184.8
70	9/10	388.8	187.3

Table 3.3 Raw data from pressure-density tests for barley straw.

Load Setting (%)	Flake size (lever position out of 10)	Plunger Force (kN)	Bale Density (kg/m^3)
40	3/10	221.9	113.3
40	6/10	210.5	110.0
40	9/10	216.8	106.6
60	3/10	315.4	121.9
60	6/10	315.6	124.8
60	9/10	315.8	125.9
80	3/10	398.8	131.9
80	6/10	383.2	140.0
80	9/10	403.2	141.4
100	3/10	483.6	140.9
100	6/10	500.0	143.9
100	9/10	493.8	147.6

3.4.3 Pressure Distribution Tests

In order to validate the developed analytical model for the pressure distribution and develop empirical models for the pressure distribution, experimental data of forces inside the bale were required. Therefore, the uni-axial sensor was put inside the compression chamber to record the forces inside the bale along the length of compression chamber for alfalfa. The sensor was inserted in the bale in the *x*-, *y*- and *z*-directions via a small window located on the side wall (Figs. 3.32, 3.33, and 3.34). In

this case, the load was set at 70% and the flake size set at 5/10. Alfalfa at 15.7% (wb) moisture content was baled and tests were repeated three times for each direction. The displacement sensor was also set to record the load cell position inside the bale with respect to the full extension point of the plunger in the *x*-direction.

Figure 3.32 Load cell inside the bale in the *x*-direction.

Figure 3.33 Load cell inside the bale in the *z*-direction.

Figure 3.34 Load cell inside the bale in the *y*-direction.

Forces recorded by the uni-axial sensor for alfalfa were compared with the plunger forces measured by installing strain gages on the plunger arms in the pressure-density tests (section 3.4.1). Results showed that forces recorded by the sensor in the *x*-direction were twice as high as the forces measured by installing strain gages shown in Table 3.2 (Fig. 3.35). This showed that the uni-axial sensor was not able to record accurate data of force inside the compression chamber. Therefore, because of the inaccuracy of forces obtained with the uni-axial sensor, a tri-axial sensor was designed and used in the succeeding experiments.

The tri-axial sensor was used to measure the forces inside the bale in different directions when whole green barley, barley straw, and wheat straw were baled. This sensor was put inside the bale using a small window located on the bale chamber side wall by drilling a hole at the bale cross-section center (Fig. 3.36). Whole green barley was baled in August 2003 in Saskatoon with 51.0% of moisture content at the baling

speed of 8 km/h. The load and the flake size were set at 50% and 5/10, respectively. Barley straw was baled in early September in Saskatoon at a 12.0% moisture content and forward speed of 8 km/h. The load and the flake size settings were 60% and 5/10, respectively. Wheat straw with 9.7% moisture content was baled in late September. The

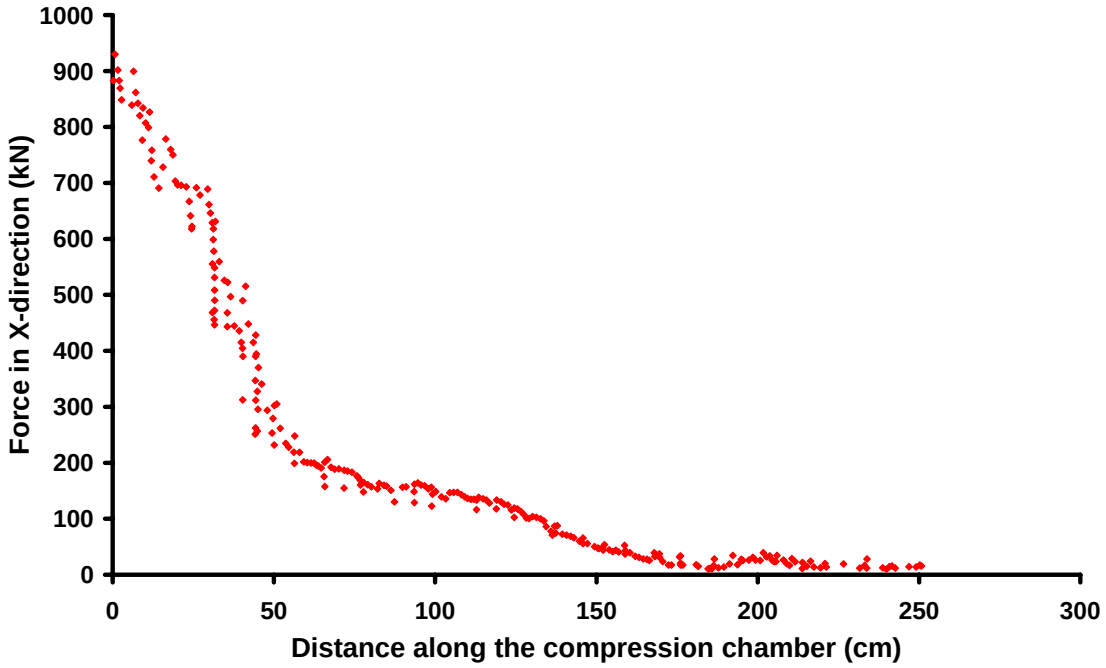

Figure 3.35 Force distribution along the compression chamber length in the *x*-direction for alfalfa recorded by the uni-axial sensor at a moisture content of 15% wb and load setting of 70% (zero on the *x*-axis is the full extension point of plunger).

Figure 3.36 Tri-axial sensor inside the whole green barley bale.

load was set at 70% while the flake size setting and baling forward speed were the same as the previous tests. Each treatment consisted of the force recording for a full length of one bale, and each treatment was repeated three times for all cases. The same data acquisition system, used in the sensor calibration, was utilized to record the output of the sensor at the frequency of 50 Hz.

3.5 Measurement of Crop Properties

Measurement of some crop properties such as coefficients of friction, adhesion, and modulus of elasticity are covered in this section.

3.5.1 Friction and Adhesion Coefficients

In this research, the coefficient of friction of selected forage materials on a polished steel surface was measured in the laboratory using the Wykeham Farrance

shear box apparatus (Fig. 3.37). This apparatus consisted of a sample box for holding the material samples, a force transducer to record the frictional force, two linear variable differential transformers (LVDT) to measure the sample horizontal and vertical displacements, a linkage to apply the normal force to the sample, and an electrical motor to provide a relative motion for the variable half of the sample box with respect to its fixed half. The coefficient of external friction was measured for alfalfa, barley straw, wheat straw, and whole green barley on a polished steel surface. In the case of alfalfa and barley straw, four levels of material moisture content were considered (12.0, 22.0, 31.0, and 42.2% (wb) for alfalfa and 12.2, 20.3, 32.9, 45.7 (wb) for barley straw), and tests were carried out at five levels of normal pressures (200, 330, 500, 600, and 735 kPa).

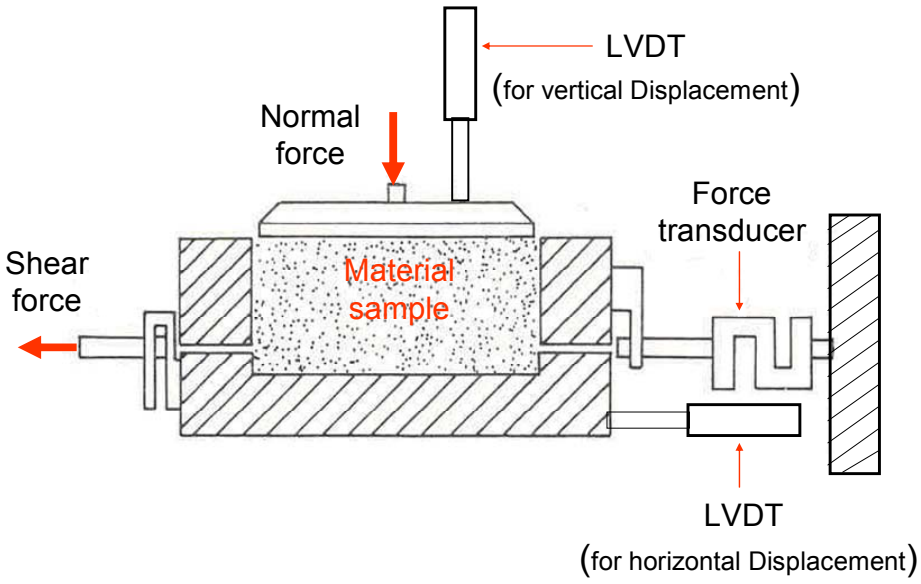

Figure 3.37 Schematic of the Wykeham Farrance shear box (redrawn from Moysey and Hiltz 1985).

The coefficients of friction of wheat straw and whole green barley on a polished steel surface were measured at only one level of moisture content which were 10.0 and 51.0% for wheat straw and whole green barley, respectively. Alfalfa samples were selected from the first cut alfalfa of 2003 crop, and barley and wheat straw were chosen from straw left on the field after harvesting in August 2003. A pre-calculated amount of water was sprayed to the samples to achieve the required moisture, and then the samples were kept in the climate controlled storage for 72 hours. For each test, a sample of forage material was put in the sample box and the bottom half of the sample box was subjected to a shear force by the electrical motor at a shear rate of 0.4 mm/min for each of the aforementioned normal pressures (Fig. 3.38). The frictional force was recorded by the force transducer. The horizontal and the vertical displacements were recorded by the horizontal and vertical LVDTs, respectively. Each test was repeated three times, and the SAS software (SAS Institute, Cary, NC) was used to analyze the data of the experiments in the form of a completely randomized design. The maximum shear stresses were plotted versus the normal pressures at each level of moisture content. The slope of the best fit line to the plotted data was considered as the coefficient of friction, and the *y*-intercept of the line was considered as the adhesion coefficient of the sample at that moisture content based on Coulomb's equation (Fig. 3.39). Data which graph shown in Figure 3.39 was created based on is presented in Table 3.4. Coulomb's equation expresses shear stress as a function of normal stress, coefficient of friction, and adhesion or cohesion coefficients as follow:

$$\tau = A_d + \mu\sigma_n , \tag{3.59}$$

where:

τ = shear stress (kPa),

A_d = adhesion coefficient (kPa),

μ = coefficient of external friction (decimal) and

σ_n = normal stress (kPa).

Figure 3.38 Measurement of the coefficient of friction using Wykeham Farrance shear box.

Table 3.4. A sample of data used to calculate coefficient of friction.

Normal Stress (kPa)	Shear Stress (kPa)
198.9	30.3
331.8	51.6
499.9	78.2
599.0	87.3
734.3	112.6
198.9	32.7
331.8	51.2
499.9	77.6
599.0	85.9
734.3	110.5
198.9	32.9
331.8	48.4
499.9	76.1
599.0	91.7
734.3	111.6

3.5.2 Modulus of Elasticity

The relationship between strain and stress in the proportional limit of the stress-strain curve of the engineering materials could be explained using the modulus of elasticity, E, which is the ratio of stress to strain ($E = \sigma/\varepsilon$). A single value of the modulus of elasticity is considered for the stresses used in design calculations of most engineering materials, because the stress-strain relationship is linear below the proportional limit for these types of materials. For biological materials, the apparent modulus of elasticity is used to explain the relationship between stress and strain. Apparent modulus of elasticity is

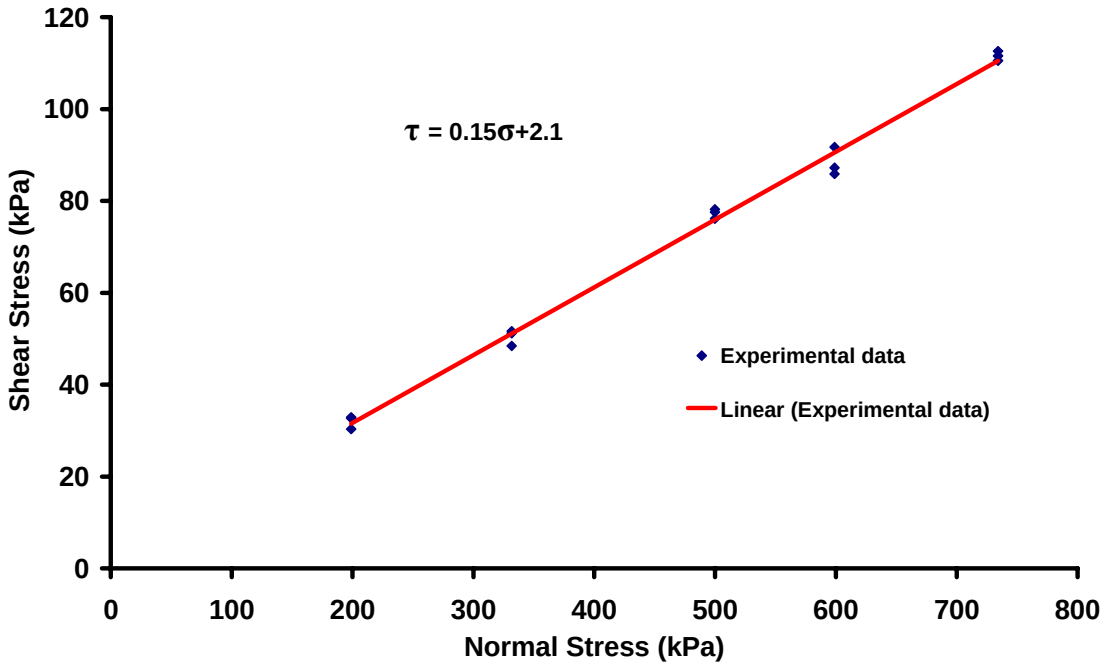

Figure 3.39 Coefficients of friction and the adhesion or cohesion coefficients from the data of shear box.

calculated based on two different definitions called the secant definition and the tangent definition. In the secant definition, the apparent modulus is considered as theratio of stress to strain at a certain point, while the apparent modulus in tangent method is defined as the slope of the stress-strain curve at a certain point on the curve (Stroshine 2000). Figure 3.42 shows calculation of modulus of elasticity at point C using these two methods. In the secant method, modulus of elasticity at point C is defined as the slope of line AC, while in tangent method slope of line BD is considered as modulus of elasticity at point C.

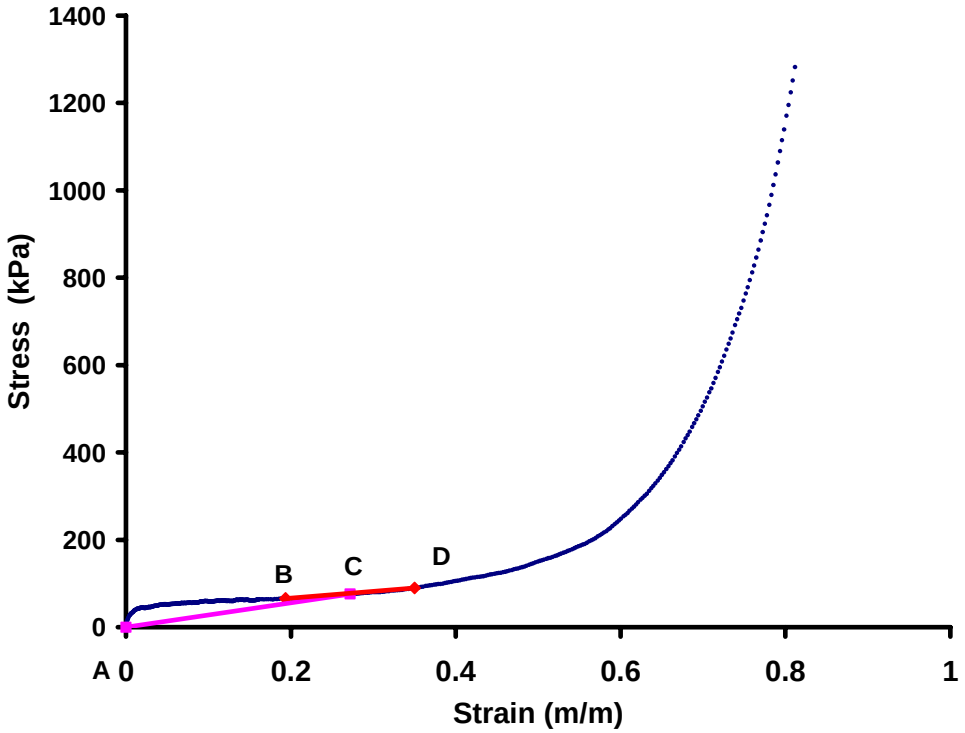

Figure 3.40 Two methods of calculating modulus of elasticity at one point of stress-strain curve.

In order to find a relationship between apparent modulus of elasticity and bulk density of alfalfa and barley straw, the data of the tests performed for the particle stiffness were used. When forage materials were compressed in a closed-end cylinder, these materials were deformed only in the *x*-direction and strains in the *y*- and *z*-directions were zero. Using Eq. 3.6 and setting strains in the *y*- and *z*-directions to zero, the following relation will be found between stress and strain in the *x*-direction:

$$\sigma_x = \frac{E(1-\nu)}{(1+\nu)(1-2\nu)}\varepsilon_x = FE\varepsilon_x, \tag{3.60}$$

where:

$$F = \frac{(1-\nu)}{(1+\nu)(1-2\nu)}. \tag{3.61}$$

According to Eq. 3.60, when one of the aforementioned methods is used to calculate modulus of elasticity, the obtained values (bulk modulus) are a combination of modulus of elasticity and Poisson's ratio. Because, Poisson's ratio is a constant coefficient, plotting the obtained values versus material bulk density can show the trend of variation of modulus of elasticity with respect to material density.

The tangent method for the modulus calculation was used to calculate the product of F (a function of Poisson's ratio) and the modulus of elasticity (E). The stress-strain curve was plotted for each of the tested materials. This curve consisted of three parts: a) an elastic part, which started from the origin and continued up to the point with 50.00 kPa and 0.04 m/m of stress and strain, respectively. This part was very small relative to the compacting part and could be ignored in the modulus calculation process; b) a compacting part, which was the most dominant part of the stress-strain curve in the compression process with an almost constant slope; and c) an incompressible part in which strain remained constant with increasing stress. This part occurred at the high stresses which are not encountered in the baling process; therefore this part was also eliminated in the modulus calculation process. Thus, the compacting part of stress-strain curve (part b) was considered and FE was calculated at each point of the curve using the central difference approximation of the first derivative at that point. Therefore, this value at each point was calculated from the ratio of the difference between the stresses of the two points equidistant from that point (0.002 m/m from either side) to the difference between their strains (Fig. 3.40). Density of the samples was calculated at each strain, and the FE-γ curve was then plotted using the calculated FE values to find the trend of variation of modulus of elasticity with respect to the material density. A sample of the raw data taken in this test is shown in Table 3.5.

Table 3.5 A sample of data used to evaluate the variation of modulus of elasticity with respect to bulk density.

Bulk Density (kg/m^3)	$\frac{(1-\nu)E}{(1+\nu)(1-2\nu)} = FE$ (MPa)
99.0	0.23
100.5	0.23
101.9	0.08
104.5	0.08
105.0	0.08
106.6	0.16
107.7	0.08
109.4	0.31
110.5	0.16
128.9	0.25
133.1	0.30
137.4	0.37
142.2	0.33
147.2	0.16
152.5	0.43
158.3	0.36
164.6	0.45
171.4	0.36
178.7	0.45
186.7	0.40

CHAPTER 4

RESULTS AND DISCUSSION

In this chapter, results of model development and validation, sensor design, and field and laboratory tests are discussed.

4.1 Model Development and Validation

In this section results of model development and validation for the pressure distribution and pressure-density relationship are covered. In each case, results of both analytical and empirical models are discussed.

4.1.1 Analytical Model for the Pressure Distribution

The analytical models for the pressure distribution in the *x*-, *y*-, and *z*-directions were derived based on the theory of elasticity by assuming isotropic linear elastic behavior for the forage materials (Eqs. 3.40, 3.43, and 3.44). In the literature, only one model was found regarding the distribution of pressure inside the compression chamber of balers (Sitkei's model, Eq. 2.19). The developed model in this study (Eq. 3.40) has three important advantages compared to Sitkei's model (Eq. 2.19). The advantages are:

1. The new model (Eq. 3.40) is much simpler than Sitkei's model (Eq. 2.19), has fewer terms, and calculating the pressure using this model is much easier.
2. In the new model, the pressure on the plunger (P_p) has been used as the boundary condition to solve the governing differential equation instead of the pressure at

the end of the bale chamber (P_e) which had been used in Sitkei's model (Eq. 2.19). Measuring the pressure on the plunger is much easier than the pressure at the end of the bale chamber; therefore, the boundary condition used in the new model is much more accessible than that of Sitkei's model (Eq. 2.19).

3. The new model is more general than Sitkei's model (Eq. 2.19), because it is applicable to all kinds of balers (including the balers with top and side walls inclined), whereas Sitkei's model (Eq. 2.19) is only applicable to the balers with one pair of converging walls.

4.1.2 Validation of the Analytical Model

The analytical model (Eq. 3.40) was validated using the experimental data collected for three different crops including barley straw, wheat straw, and whole green barley. The least-square regression analysis method was used to validate the analytical model in the x-direction (Eq. 3.40). In this method, υ, μ, and E were changed in order to minimize the summation of the square difference between data resulting from the model (Eq. 3.40) and the experimental data. Values of υ, μ, and E corresponding to the minimum sum square error were considered as the estimated values for these parameters. Values of 0.32, 0.38, and 0.40 were estimated for Poisson's ratio of whole green barley, wheat straw, and barley straw, respectively (Table 4.1). Sitkei (1986) reported the range of 0.25 to 0.35 for Poisson's ratio of forage materials for the pressure range encountered in balers and the range of 0.35 to 0.45 for the pressure range encountered in pelleting machines. Because the pressure in a large square baler is usually higher than the pressure in smaller balers, the estimated values for Poisson's ratio of the tested materials are acceptable. For the modulus of elasticity, values of 10,

39, and 2.4 kPa were estimated from the analytical model validation for barley straw, wheat straw, and whole green barley, respectively (Table 4.1). The estimated value of the modulus of elasticity for barley straw was much lower than the measured value (122.5 kPa). There were no measured values of modulus of elasticity for wheat straw and whole green barley to compare the estimated values with. For the coefficient of friction between forage materials and bale chamber walls, values of 0.55, 0.43, and 0.45 were estimated for whole green barley, wheat straw, and barley straw, respectively (Table 4.1). These values were approximately three times as high as the coefficient of friction of the same crops on polished steel surface measured in laboratory using shear box at the similar moisture content. After observing these high values for coefficient of

Table 4.1 Constants of the analytical model for the pressure distribution in the *x*-direction for the different forage materials.

Material type	α (rad)	β (rad)	E (kPa)	μ	ν
Barley straw	0.09	0.13	10	0.45	0.40
Wheat straw	0.08	0.14	39	0.43	0.38
Whole green barley	0.07	0.12	2.4	0.55	0.32

friction, the surface of the compression chamber walls was inspected. It was observed that the wall surface was covered by a rough layer of crop dry extract which increased the coefficient of friction. In reality, after baling the first few bales (especially with the higher moisture content), the wall surface will not be a polished steel surface anymore. It will be a rough surface with a high coefficient of friction. Therefore, coefficients of

friction estimated from the analytical model are more realistic than the measured ones in laboratory. The following are the results of model validation for barley straw, wheat straw, and whole green barley.

4.1.2.1 Barley Straw

Pressure distribution inside the compression chamber of the baler in the *x*-direction for barley straw at a load setting of 60% and the material moisture content of 12.2% (wb) is shown in Figure 4.1. Both the experimental data and the predicted pressure values (based on Eq. 3.40) are presented in this figure. According to this plot, the best fit between the experimental data and the predicted values was found at the beginning of the compression chamber length close to the plunger and at the end of the bale chamber length. The error of the pressure prediction on the plunger ($x = 0$) was very low which proved that the model has accurately estimated the pressure on the baler plunger. The standard error and the coefficient of determination of the regression analysis in this case were 20.0 kPa and 0.95, respectively (Table 4.2).

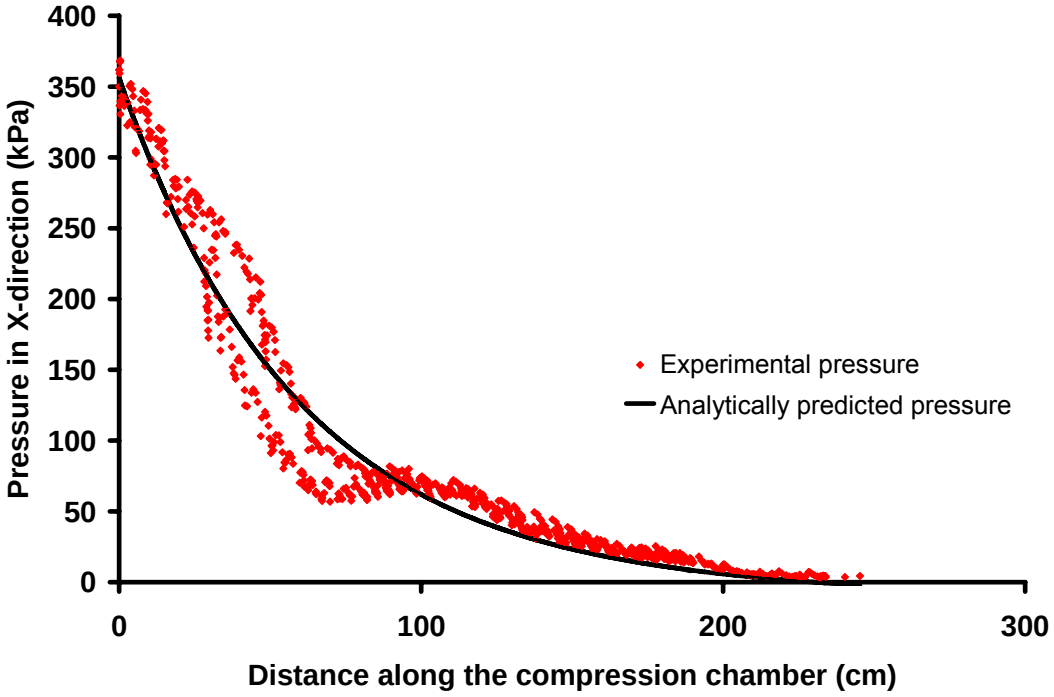

Figure 4.1 Experimental pressure distribution and the predicted pressure distribution based on the analytical model along the compression chamber length in the *x*-direction for barley straw at a moisture content of 12.2% (wb) (zero on the *x*-axis is the full extension point of plunger).

Table 4.2 The coefficient of determination and the standard error of the analytical model in the *x*-direction for different forage materials.

Material type	R^2	Standard error (kPa)
Barley straw	0.95	20.0
Wheat straw	0.95	26.0
Whole green barley	0.96	18.4

According to Eq. 3.43, the vertical pressure (pressure in the *y*-direction) inside the compression chamber of a large square baler at a certain distance from the plunger is a function of the pressure in the *x*-direction, crop properties, and the compression chamber dimensions. Therefore, the pressure distribution along the compression chamber length in the *y*-direction (vertical pressure) for barley straw was obtained using Eq. 3.43 and the data of the predicted horizontal pressures (Fig. 4.2). The pressure distribution in the *y*-direction showed the same pattern as the pressure distribution in the *x*-direction with the highest pressure near the plunger and the lowest pressure at the end of the compression chamber. The maximum pressure in the *y*-direction for the barley straw was about 65% of the maximum pressure in the *x*-direction. The experimental data are also presented in Fig. 4.2. There was a significant difference between the experimental and predicted pressures near the baler plunger, while at the end of compression chamber these pressures were very close together. This showed that the analytical model failed to accurately predict the pressure in the *y*-direction due to the following potential reasons:

1. The analytical model in the *x*-direction was developed by assuming constant value for Poisson's ratio (υ). This value was estimated by validating the analytical model in the *x*-direction and was used in the analytical model in the *y*-direction to predict pressure in this direction. This estimated constant υ was an average value of the actual variable Poisson's ratio. In reality, υ probably has not been constant along the compression process. This ratio has had its minimum value (which has been smaller than the estimated value) at the beginning of compression process (near the plunger) and has increased with increasing distance from the plunger. Therefore, the maximum difference between the

experimental data and the predicted pressures was observed at the beginning of the compression process and the minimum difference was observed at the end of the compression chamber.

2. The experimental data have been much smaller than the expected pressures in the *y*-direction due to the gap between the dug hole inside the bale and the sensor body. Therefore, at the beginning of the baling process the difference between the experimental data and the predicted pressures were very large, while after filling the gap at the end of the compression chamber, the sensor was able to record data close to the expected pressures.

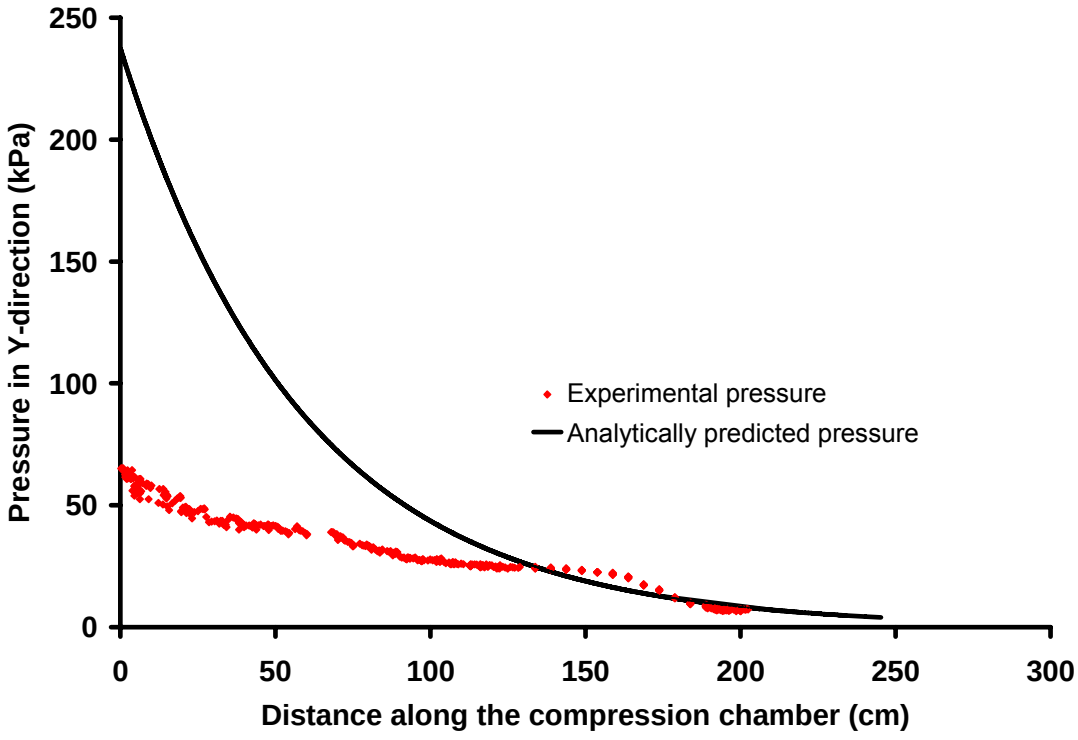

Figure 4.2 The predicted and the experimental pressure distribution along the compression chamber length in the *y*-direction (vertical pressure) based on the analytical model for barley straw at a moisture content of 12.2% (wb) (zero on the *x*-axis is the full extension point of plunger).

Equation 3.42 expresses the pressure inside the compression chamber of a large square baler in the *z*-direction (lateral pressure) in terms of the pressure in the *x*-direction, dimensions of the compression chamber, and the properties of the baled crop. This equation was used to plot the lateral pressure versus the distance from the full extension point of the plunger along the compression chamber length for barley straw by inserting in the predicted pressures in the *x*-direction into Eq. 3.44 (Fig. 4.3). The lateral pressure distribution had the same pattern as the vertical pressure with the small differences in the minimum pressures. The analytical model in the *z*-direction seemed to have the same problem as the analytical model in the *y*-direction; however, there were no experimental data available in this direction to which the predicted pressures could be compared.

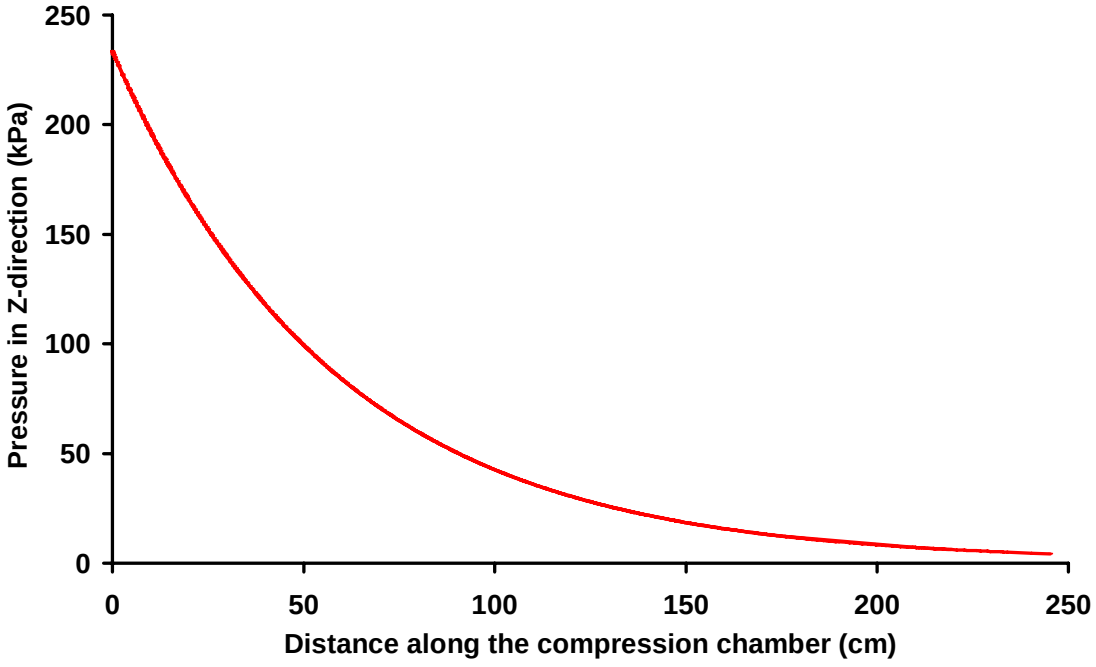

Figure 4.3 Predicted pressure distribution along the compression chamber length in the *z*-direction (lateral pressure) based on the analytical model for barley straw at a moisture content of 12.2% (wb) (zero on the *x*-axis is the full extension point of plunger).

4.1.2.2 Wheat Straw

Figure 4.4 shows the results of wheat straw compressed at a load setting of 70% and material moisture content of 9.7% (wb). The analytical model (Eq. 3.40) predicted the pressure on the baler plunger with an accuracy of 97.5%. The model showed a poor accuracy for the pressure prediction at the compression chamber length range of 50 to 100 cm and for the end of the compression chamber length. The model predicted negative values for the pressure at the distances larger than 190 cm; therefore, the model was valid until 190 cm of the compression chamber length. The regression analysis of the experimental and the predicted data of the pressure distribution in the case of wheat straw presented a high coefficient of determination (0.95) and a low standard error (26 kPa) for the model fitness to the experimental data (Table 4.2).

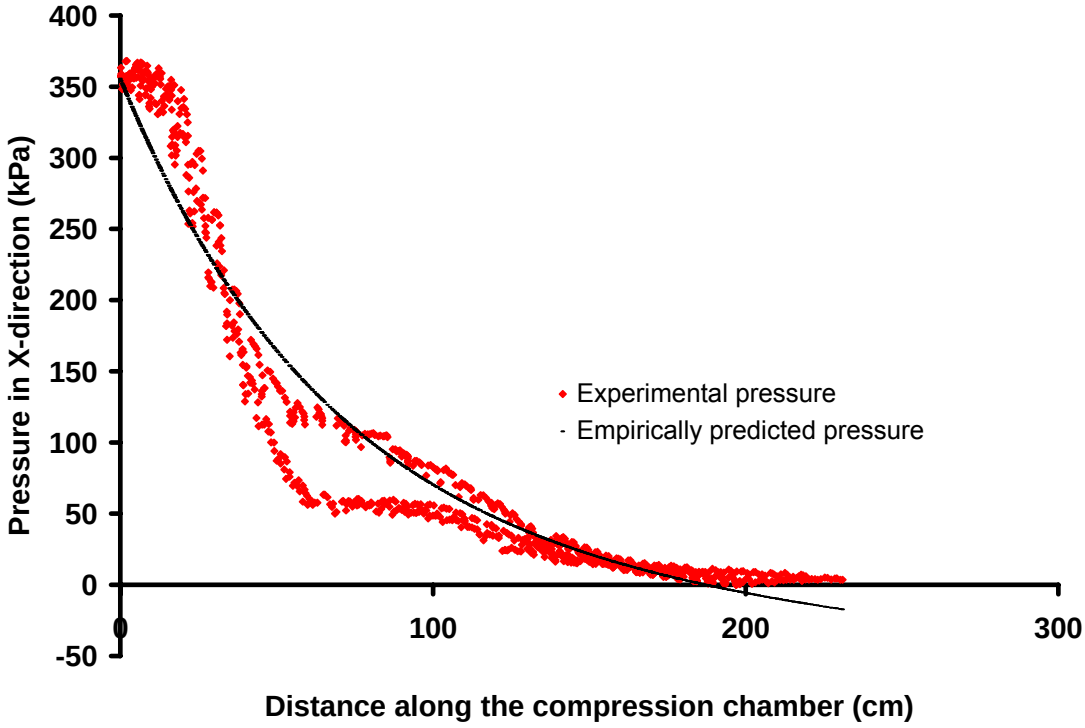

Figure 4.4 Experimental pressure distribution and the predicted pressure distribution based on the analytical model along the compression chamber length in the *x*-direction for wheat straw at a moisture content of 9.7% (wb) (zero on the *x*-axis is the full extension point of plunger).

The pressure distribution in the *y*-direction inside the compression chamber of the baler for wheat straw based on Eq. 3.43 is shown in Figure 4.5. This plot was obtained by inserting in the predicted pressures in the *x*-direction into equation 3.41. The maximum predicted vertical pressure for wheat straw was about 216 kPa which was approximately 60% of the maximum pressure in the *x*-direction. The experimental data are also presented in Figure 4.5. Similar to the results of the model validation in the *y*-direction for barley straw, there was a significant difference between the experimental data and the predicted pressures in the *y*-direction for wheat straw near the baler plunger, while at the end of the compression chamber these pressures were very close together.

Therefore the same justification stated in the case of barley straw could be true for wheat straw as well.

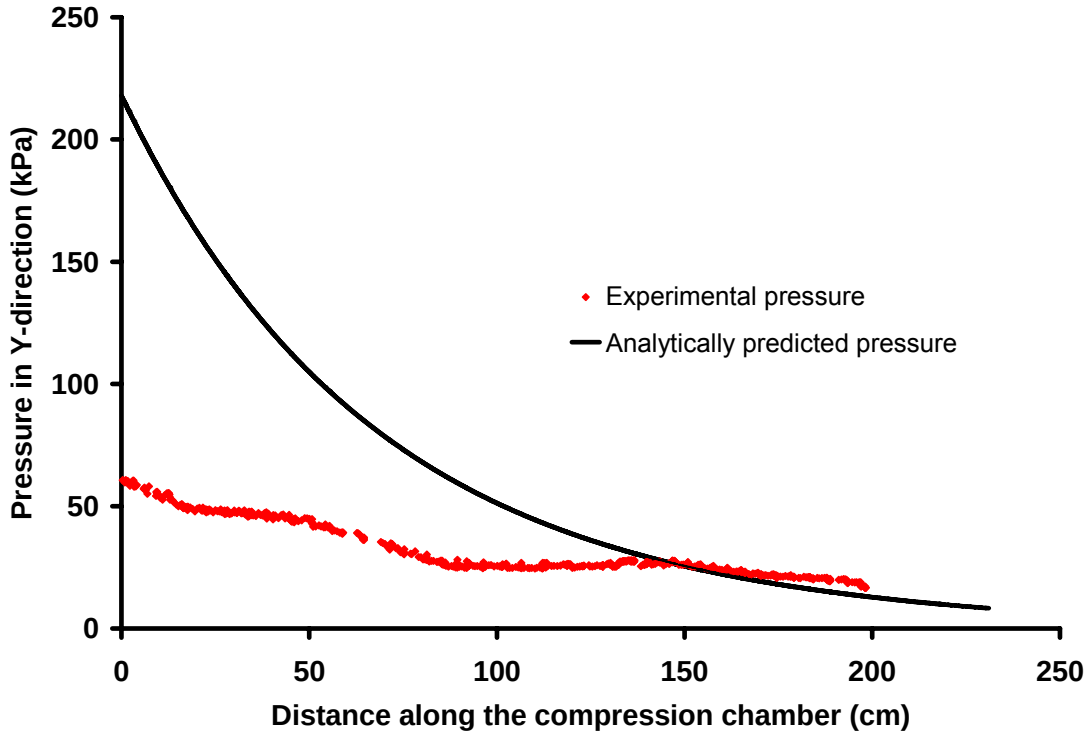

Figure 4.5 Predicted and the experimental pressure distributions along the compression chamber length in the *y*-direction (vertical pressure) based on the analytical model for wheat straw at a moisture content of 9.7% (wb) (zero on the *x*-axis is the full extension point of plunger).

Equation 3.42 was used to plot the lateral pressure versus the distance from the full extension point of the plunger along the compression chamber length for wheat straw by inserting in the predicted pressures in the *x*-direction into this equation (Fig. 4.6). Again, the pattern of the lateral pressure distribution for wheat straw was similar to the vertical pressure pattern with the almost identical pressures on the plunger. However, the model estimated the higher lateral pressure than the vertical one at the end of the compression chamber length. The analytical model in the *z*-direction probably had the

same problem as the analytical model in the *y*-direction; however, there were no experimental data available in this direction to prove that.

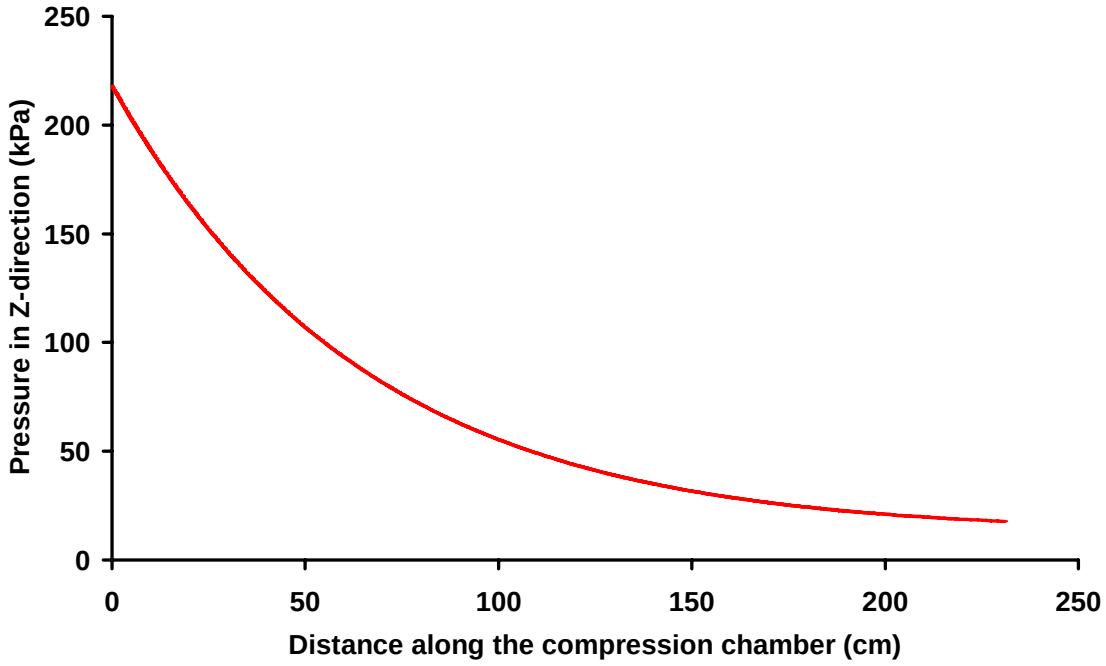

Figure 4.6 Predicted pressure distribution along the compression chamber length in the *z*-direction (lateral pressure) based on the analytical model for wheat straw at a moisture content of 9.7% (wb) (zero on the *x*-axis is the full extension point of plunger).

4.1.2.3 Whole Green Barley

The experimental and the predicted pressure distribution in the *x*-direction based on the developed analytical model for whole green barley at a load setting of 50% and material moisture content of 51% (w.b.) is shown in Figure 4.7. The results of comparing the predicted (based on Eq. 3.40) and the experimental pressures showed that the predicted pressure by the analytical model on the plunger was 10% more than the

experimental pressure at the same position. The overall coefficient of determination and the standard error in this case were 0.96 and 18.4 kPa, respectively (Table 4.2).

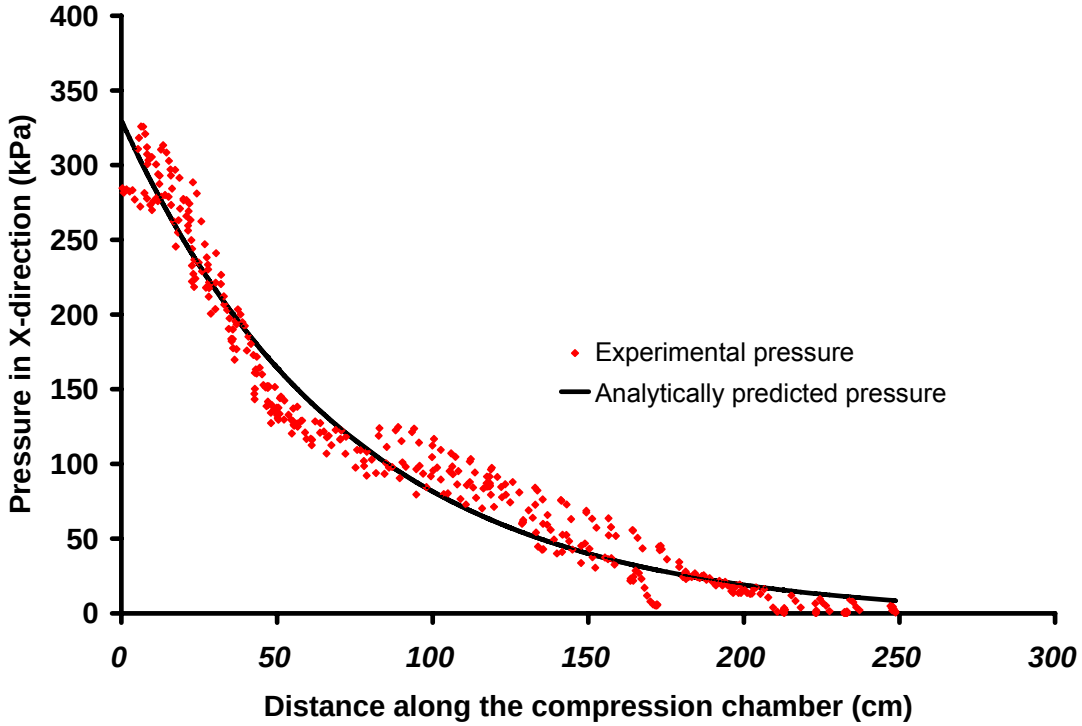

Figure 4.7 Experimental pressure distribution and predicted pressure distribution based on the analytical model along the compression chamber length in the *x*-direction for whole green barley at a moisture content of 51% (wb) (zero on the *x*-axis is the full extension point of plunger).

The pressure distribution inside the compression chamber of the large square baler in the *y*-direction (vertical pressure) for whole green barley is shown in Figure 4.8. Again, this plot resulted from Eq. 3.43 by putting the predicted pressures in the *x*-direction and the model constants into this equation. The maximum vertical pressure on the plunger was 157 kPa which was about 48% of the maximum pressure in the *x*-direction. The experimental data are also presented in this Figure. There was also a

significant discrepancy between the experimental data and the predicted pressures near the baler plunger for whole green barley, but this discrepancy was much smaller compared to the discrepancies in barley and wheat straw. This smaller difference between the experimental data and the predicted pressures was most likely due to the following reasons:

1. Whole green barley had the actual Poisson's ratio closer to the estimated ratio. On the other hand, the variation of Poisson's ratio in whole green barley was smaller than that of barley and wheat straw. Thus, the difference between the experimental data and the predicted pressures was smaller compared to this difference in barley and wheat straw.
2. The dug hole in the whole green barley bale had more uniform shape than the other materials (barley and wheat straw) because of the higher moisture content of green barley. Therefore, the gap between the sensor and the dug hole was smaller for whole green barley and it took the forces less time to fill the gap. For this reason the difference between the experimental and predicted pressures was smaller than that of barley and wheat straw.

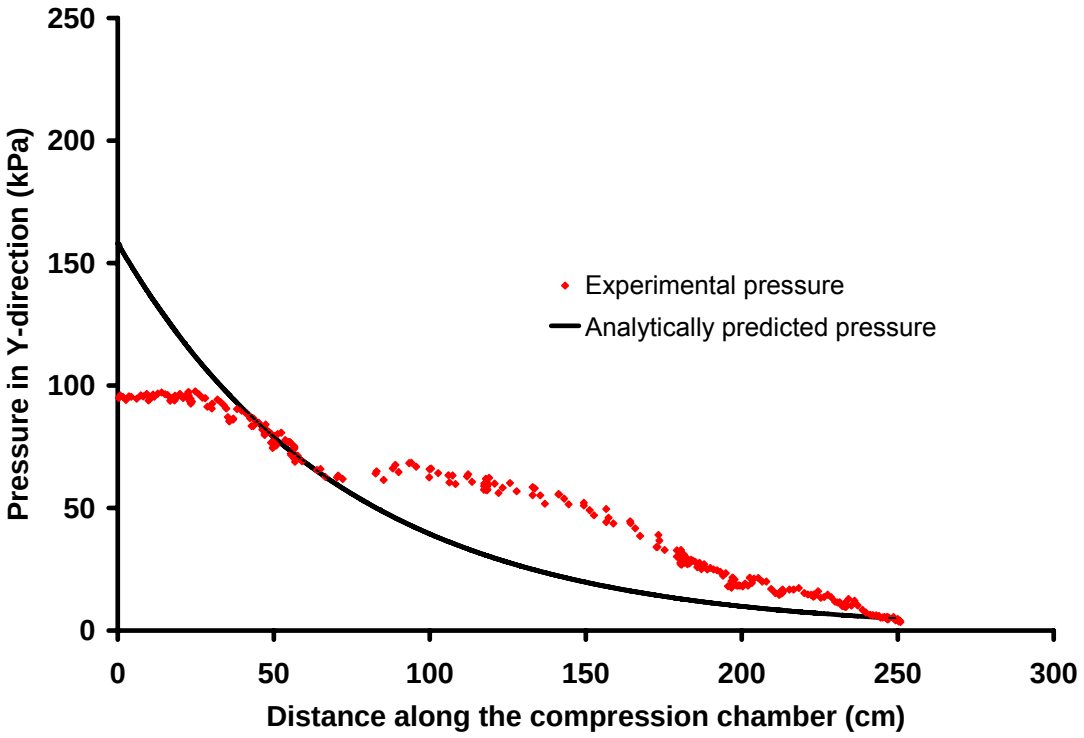

Figure 4.8 Predicted and the experimental pressure distributions along the compression chamber length in the *y*-direction (vertical pressure) based on the analytical model for whole green barley at moisture content of 51% (wb) (zero on the *x*-axis is the full extension point of plunger).

The pressure distribution in the *z*-direction (lateral pressure) for whole green barley showed almost the same pattern as the vertical pressure distribution (Fig. 4.9). In this particular case, the maximum lateral pressure on the plunger and the minimum one at the end of the compression chamber length were almost identical to the vertical maximum and minimum pressures, respectively. There were no experimental data available in the *z*-direction in this case to compare the predicted pressures with.

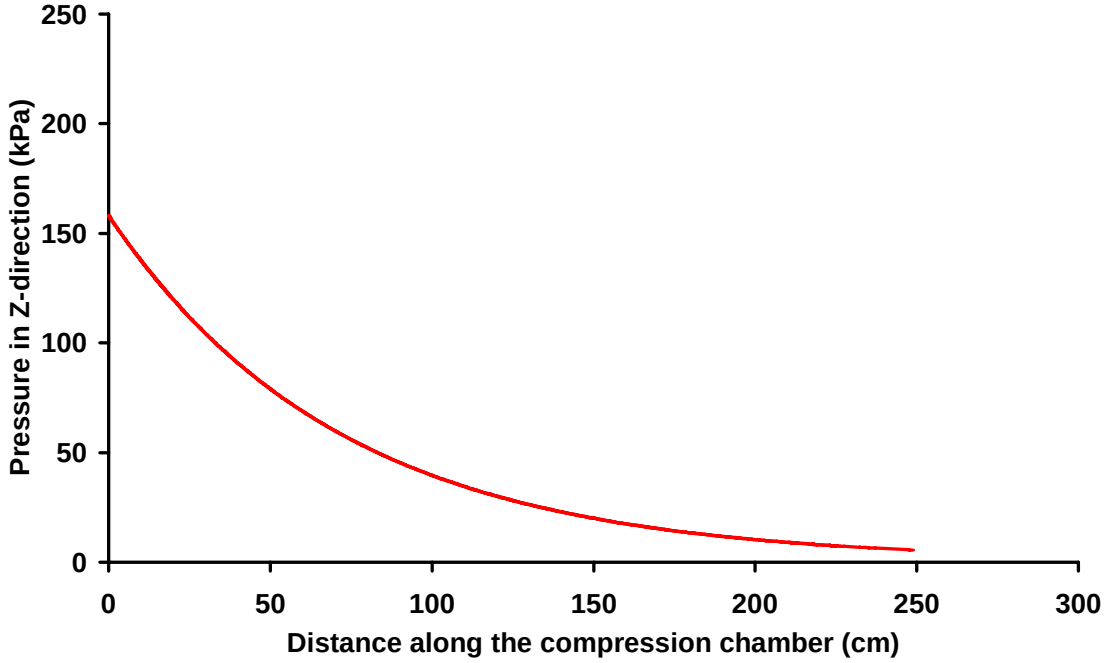

Figure 4.9 Predicted pressure distribution along the compression chamber length in the *z*-direction (lateral pressure) based on the analytical model for whole green barley at a moisture content of 51% (wb) (zero on the *x*-axis is the full extension point of plunger).

The data presented in Figures. 4.1, 4.4, and 4.7 were the results of three replications for each kind of forage material at the flake size lever position of 5/10. Comparing these graphs of the pressure distribution for different forage materials showed that the pressure distribution for all the tested forage materials had almost the same pattern. The maximum pressures for barley straw and wheat straw were approximately identical. Considering the fact that barley straw has been baled at a load setting of 60% compared to the 70% of the load setting for wheat straw, the maximum pressure resulting from baling barley straw was higher than that of the wheat straw. In the case of whole green barley, the maximum pressure was less than that of the barley

and wheat straw which was because of the lower load setting (50%) and Poisson's ratio (0.32).

The experimental pressures in all cases (for all forage materials) had their maximum values on the plunger (x = 0) and then decreased exponentially with increasing distance from the full extension point of the plunger up to about 60 cm from the plunger. At this point (point "A"), the pressure started to increase due to reduction of the cross-section area up to distance of about 95 cm from the plunger (Point "B") and again decreased. This problem occurred because of the presence of a bend in the compression chamber walls (top and side walls) which increased the standard errors and decreased the coefficients of determination of the models (Point "B" in Fig. 4.10). In reality, the compression chamber walls make two different angles with the x-axis (a larger angle for the part AB and a smaller angle for the part BC) while only one angle was considered in model development for each wall for simplification.

Equations 3.43 and 3.44 which express the vertical and the lateral pressures in terms of the pressure in the x-direction forage material properties, and the compression chamber dimensions, consist of two parts. The first part is only a function of Poisson's ratio (v) and the pressure in the x-direction, and is exactly identical in both equations. The second part is a function of the distance from the full extension point of the plunger (x), crop properties, and the compression chamber dimensions which vary from equation to equation. For the maximum lateral and vertical pressures which take place on the plunger, only the first part of the equation comes to play a role, because the distance from the full extension point of the plunger is zero (x = 0). Therefore, the maximum lateral and vertical pressures are solely functions of the maximum pressure in the x-direction and Poisson's ratio. Because the maximum pressure in the x-direction and the

Poisson's ratio for each of the tested forage material were constant, the predicted maximum vertical and the lateral pressures for each of the materials were the same but they varied between crops tested. For the minimum pressures which occurred at the end

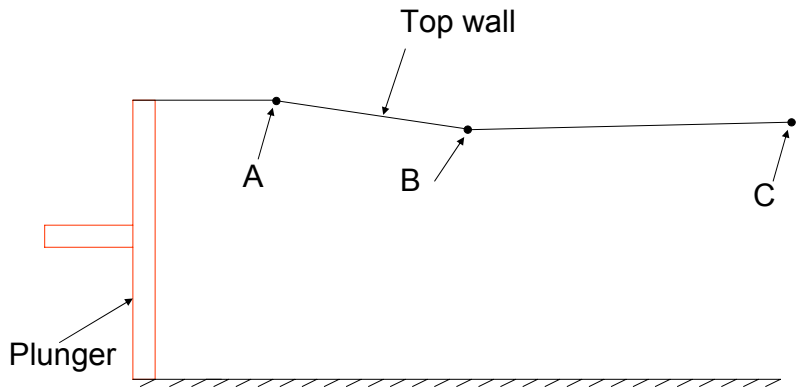

Figure 4.10 The actual shape of the top wall of the compression chamber.

of the compression chamber length, both parts of the equations play a role; therefore, the minimum vertical and lateral pressures are not necessarily identical for a certain crop.

Comparing the maximum vertical and the lateral pressures for the different materials showed that barley straw had the highest maximum lateral and vertical pressures because of its largest Poisson's ratio. Whole green barley had the lowest maximum pressures because of its lowest Poisson's ratio and lowest maximum pressure in the *x*-direction.

4.1.3 Validation of the Empirical Model

The empirical models of the pressure distribution in the *x*- and *y*-directions for different forage materials (Eqs. 3.47 and 3.48) were validated using the experimental data of field tests. The least-square regression analysis was used for model validation, and model constants were estimated for each of the tested crops (Tables 4.3 and 4.4). The coefficient of determination and the standard error were also calculated for each case as criteria of model fitness (Tables 4.3 and 4.4). A high coefficient of determination and a low standard error of the model in the *x*-direction for all tested crops revealed that there was a good correlation between the empirical model and the corresponding experimental data in the *x*-direction. In contrast, coefficient of *x* for the model ($-D_0$) in the *y*-direction had a very low value which showed that the pressure distribution in this direction was almost linear rather than exponential. The reason was probably inaccuracy of the experimental data in the *y*-direction especially near the plunger. Therefore, there was not a good correlation was not found between the empirical model and the experimental data in the *y*-direction. The empirical models were validated using the data collected for three different crops, namely barley straw, wheat straw, and whole green barley. The following are the results of the empirical model validation for different crops.

Table 4.3 Estimated constants of the developed empirical model (Eq. 3.47) for the pressure distribution in the *x*-direction for different forage materials.

Constant	Barley straw	Wheat straw	Whole green barley
A_0	370.81	410.31	326.47
B_0	0.018	0.021	0.014
R^2	0.96	0.97	0.96
Standard error	19.27	20.57	18.39

Table 4.4 Estimated constants of the developed model (Eq. 3.48) for pressure distribution in the *y*-direction for different forage materials.

Constant	Barley straw	Wheat straw	Whole green barley
C	61.2	59.2	113.3
D_0	0.0083	0.0076	0.0077
R^2	0.96	0.93	0.90
Standard error	3.1	2.6	8.2

4.1.3.1 Barley Straw

The pressure distribution inside the compression chamber of the large square baler in the *x*-direction for barley straw based on the developed empirical model at a load setting of 60% and moisture content of 12.2% (wb) is shown in Figure 4.11. Both the experimental and the predicted pressures are presented in this figure. Based on the graphs shown in this figure, the best fit between the experimental data and the predicted pressures was found at the beginning of the compression chamber length close to the

plunger with error of approximately 5%. The overall standard error and the coefficient of determination of the regression analysis in this case were 0.96 and 19.3 kPa, respectively (Table 4.3).

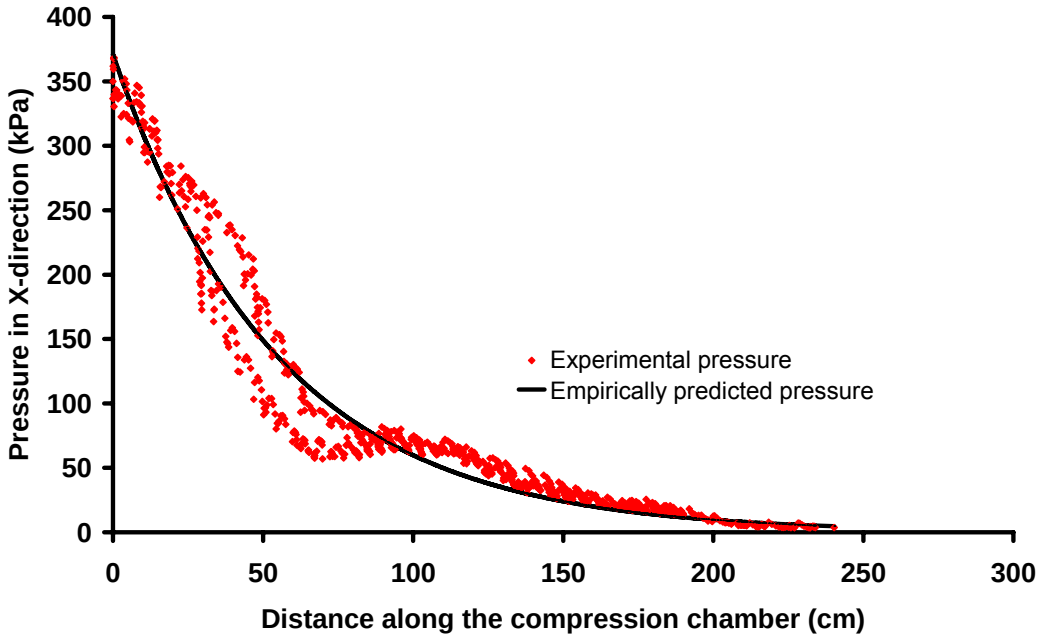

Figure 4.11 Experimental and predicted pressure distribution based on the empirical model along the compression chamber length in the *x*-direction for barley straw at a moisture content of 12.2% (wb) (zero on the *x*-axis is the full extension point of plunger).

The pressure distribution inside the compression chamber of the large square baler in the *y*-direction for barley straw based on the developed empirical model at a load setting of 60% and material moisture content of 12.2% (wb) is shown in Figure 4.12. Based on the results shown in this plot, the model predicted the maximum vertical pressure on the baler plunger with error of approximately 5.4%. The standard error and the coefficient of determination of the regression analysis for the vertical pressure were

3.1 kPa and 0.96, respectively (Table 4.4). The experimental data showed the trend of the pressure distribution in the *y*-direction; however these data were much smaller than the actual data (especially near the plunger).

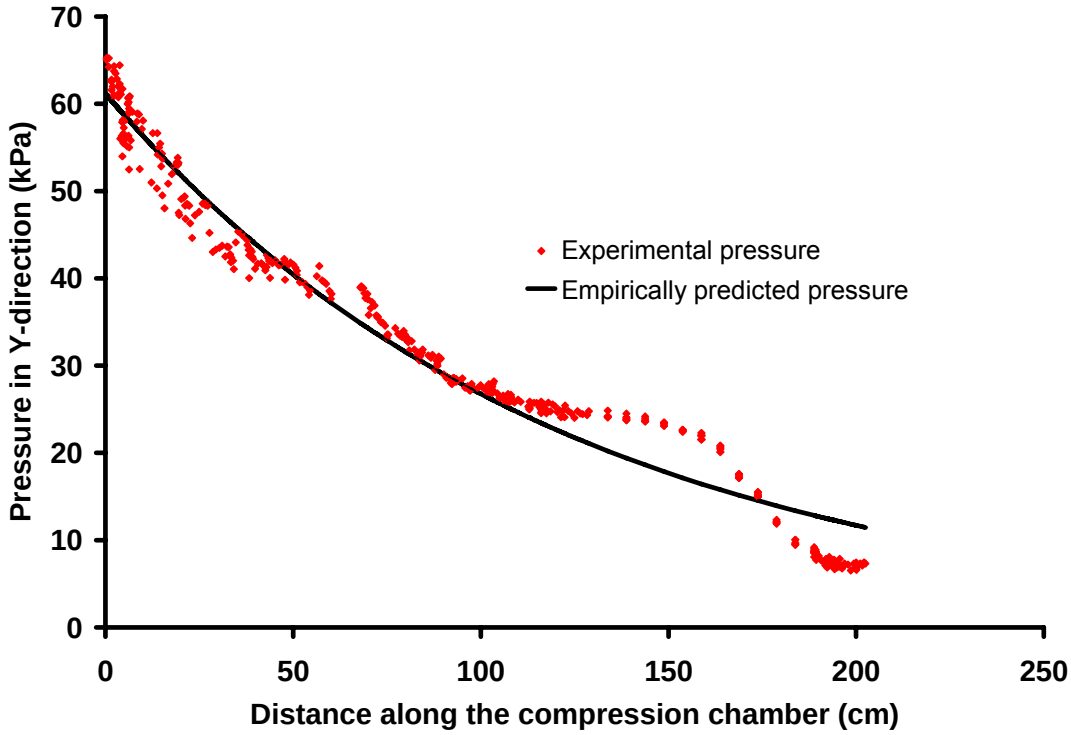

Figure 4.12 Experimental and predicted pressure distribution based on the empirical model along the compression chamber length in the *y*-direction (vertical pressure) for barley straw at a moisture content of 12.2% (wb) (zero on the *x*-axis is the full extension point of plunger). The same experimental data as in Figure 4.2 was used in this plot.

4.1.3.2 Wheat Straw

Figure 4.13 shows similar results for the wheat straw at a load setting of 70% and material moisture content of 9.7% wb. The experimental and the predicted pressures along the compression chamber length are presented in different colors to show the

accuracy of the model fitness. For wheat straw, the empirical model overestimated the pressure on the baler plunger with the accuracy of 87.3% which was the lowest compared to the accuracy of the pressure prediction of the empirical model for the other forage materials at the same position. The regression analysis of the experimental and the predicted data of the pressure distribution in the case of wheat straw showed a high coefficient of determination and a low standard error for the model fitness to the experimental data which were 0.97 and 20.6 kPa, respectively (Table 4.3).

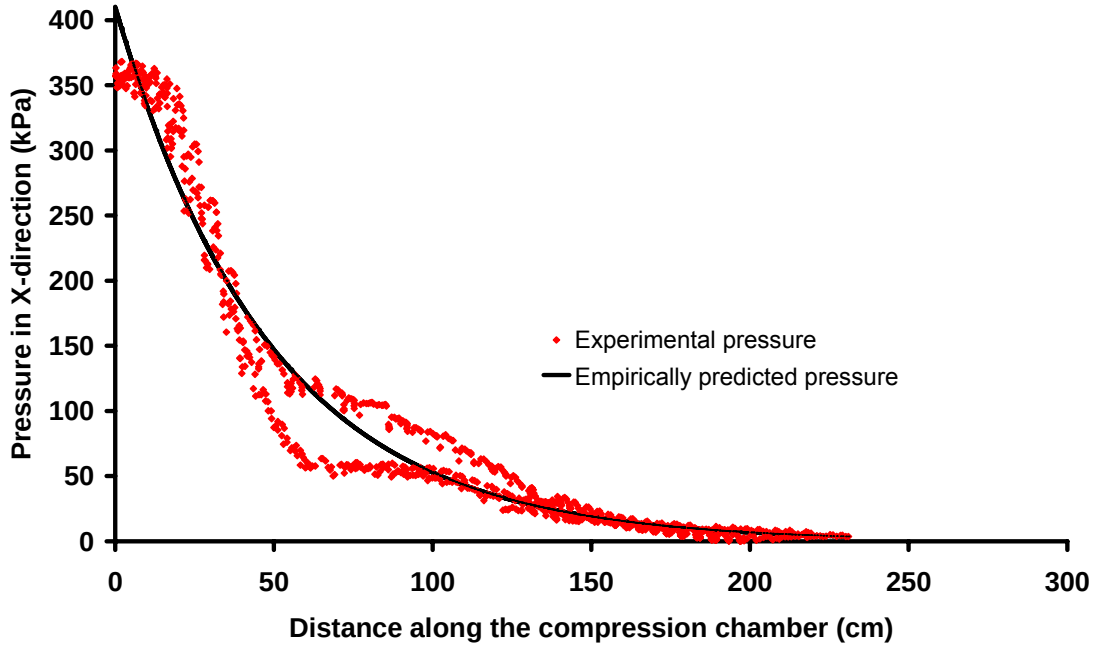

Figure 4.13 Experimental and the predicted pressure distributions based on the empirical model along the compression chamber length in the *x*-direction for wheat straw at a moisture content of 9.7% (wb) (zero on the *x*-axis is the full extension point of plunger).

The pressure distribution inside the compression chamber of the baler in the *y*-direction for wheat straw based on the developed empirical model at a load setting of 70% and material moisture content of 9.7% w.b. is shown in Figure 4.14. Based on the

results shown in this plot, the model predicted the maximum vertical pressure on the baler plunger with error of approximately about 2.6%. The overall standard error and the coefficient of determination of the regression analysis for the vertical pressure were 2.6 kPa and 0.93, respectively (Table 4.4). The experimental data showed the trend of the pressure distribution in the *y*-direction; however the values of these data were not reliable (especially near the plunger).

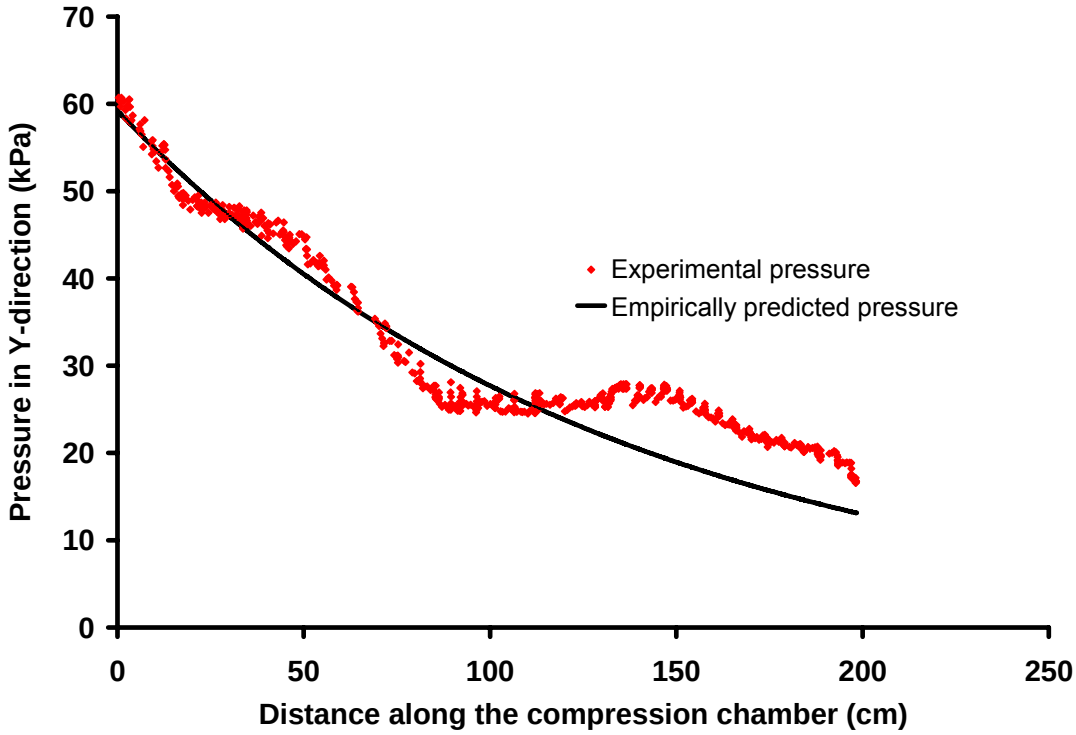

Figure 4.14 Experimental and the predicted pressure distributions based on the empirical model along the compression chamber length in the *y*-direction (vertical pressure) for wheat straw at moisture content of 9.7% (wb) (zero on the *x*-axis is the full extension point of plunger). The same experimental data as in Figure 4.5 was used in this plot.

4.1.3.3 Whole Green Barley

The experimental and the predicted pressure distribution in the *x*-direction based on the developed empirical model for whole green barley at a load setting of 50% and moisture content of 51% (wb) are presented in Figure 4.15. Results of the comparison of predicted and experimental showed that the empirical model predicted the pressure on the plunger with error of about 5%. The overall coefficient of determination and the standard error in this case were 0.96 and 18.4 kPa, respectively (Table 4.3).

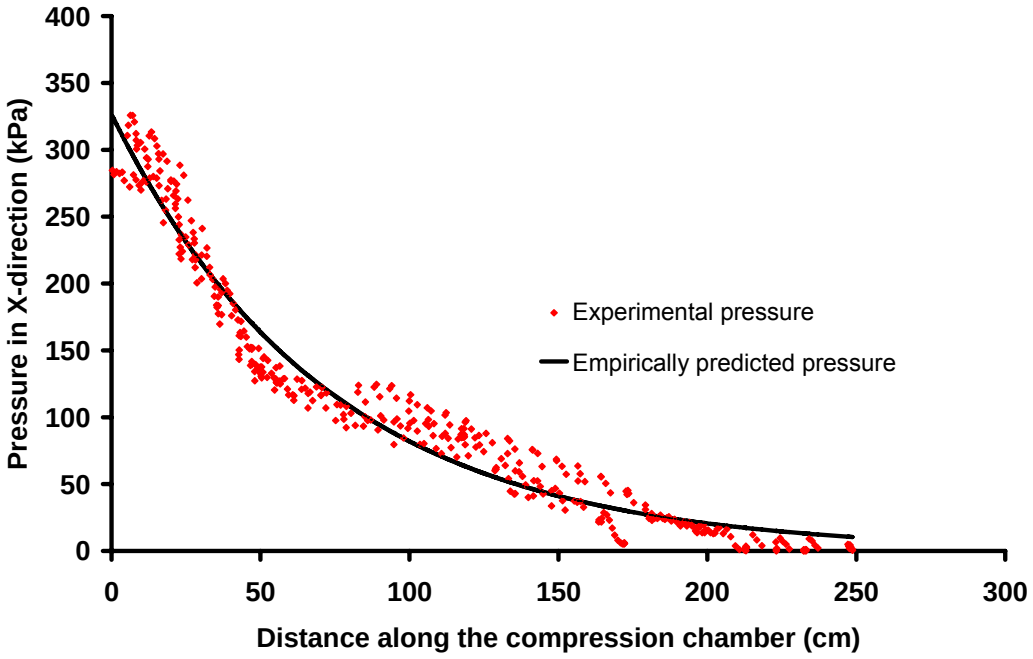

Figure 4.15 Experimental and the predicted pressure distribution based on the empirical model along the compression chamber length in the *x*-direction for whole green barley at moisture content of 51% (wb) (zero on the *x*-axis is the full extension point of plunger).

The pressure distribution in the *y*-direction for whole green barley based on the developed empirical model at a load setting of 50% and material moisture content of

51% (wb) is shown in Figure 4.16. Based on the results shown in this plot, the model predicted the maximum vertical pressure on the baler plunger with error of approximately about 17.9%. The overall standard error and the coefficient of determination of the regression analysis for the vertical pressure were 8.2 kPa and 0.90, respectively (Table 4.4). The experimental data showed the trend of the pressure distribution in the *y*-direction; however these data were much lower than the actual data (especially near the plunger) and were not reliable from the viewpoint of their values.

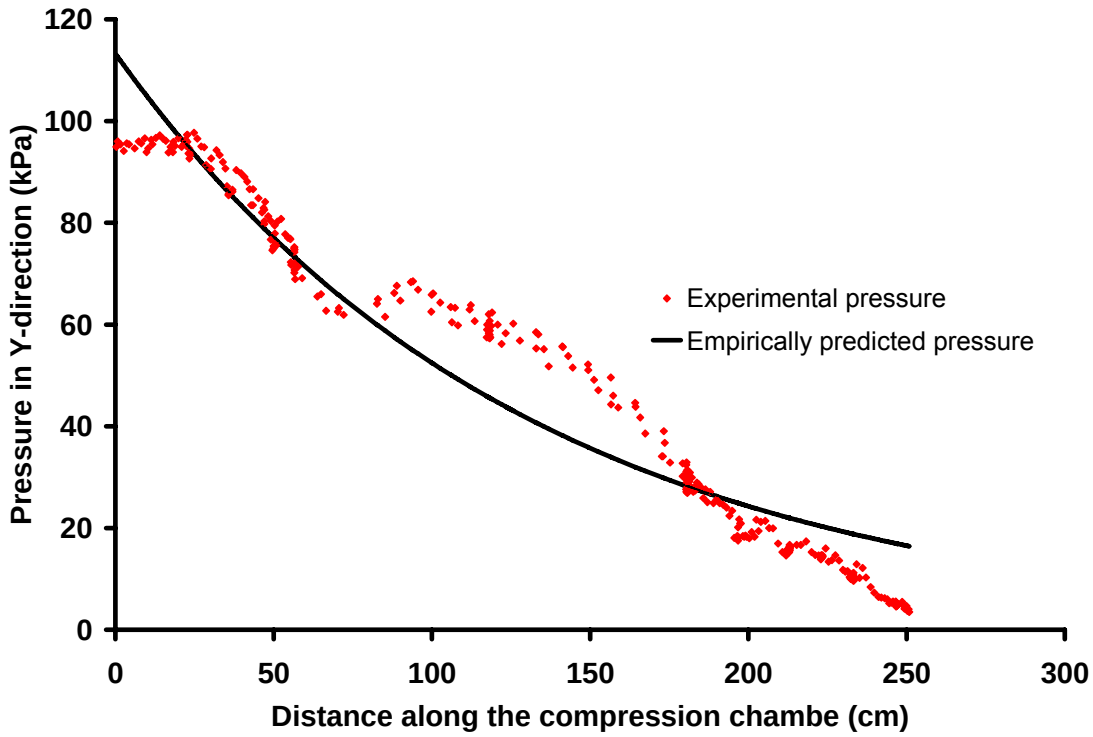

Figure 4.16 Experimental and the predicted pressure distribution based on the empirical model along the compression chamber length in the *y*-direction (vertical pressure) for whole green barley at a moisture content of 51% (wb) (zero on the *x*-axis is the full extension point of plunger). The same experimental data as in Figure 4.2 was used in this plot.

4.1.4 Comparison of Analytical and Empirical Models

The analytical model for the pressure distribution was a complicated model and had many parameters. These parameters which were related to the compression chamber dimensions or forage material physical and mechanical properties have to be measured prior to the modeling process. Measuring these parameters is usually a time-consuming exercise and is very expensive. In contrast, the empirical models were simple equations which were only functions of the distance from the full extension point of the plunger along the compression chamber. Comparing the analytical and empirical models of the pressure distribution in the *x*-direction (Eqs. 3.40 and 3.47) showed that the general form of the empirical model was exactly the same as the first term of the analytical model. Because the value of the first term of Eq. 3.40 was very large relative to that of the other terms, especially for the distances less than 150 cm (Table 4.5), it was reasonable to have the empirical model with the general form of the first term of Eq. 3.40. Coefficient "A_0" in this model is identical to the pressure on the plunger (P_p). Ideally, these two coefficients (A_0 in the empirical model and P_p in the analytical model) should be equal to the experimental pressure on the plunger (maximum experimental pressure) but in practice, there was some discrepancy between these coefficients depending on the model accuracy. Results of model validation showed that the coefficient "A_0" in the empirical model for barley straw, wheat straw, and whole green barley were 370.8, 410.3, and 326.5 kPa, respectively (Table 4.3), while P_p in the analytical model was 350.0, 360.0, and 325.0 kPa for barley straw, wheat straw, and whole green barley, respectively.

Comparing the results of the analytical and the empirical models in the *x*-direction for barley straw revealed that the empirical model provided more accurate pressure prediction with a larger coefficient of determination and a lower overall

standard error; however, the analytical model provided more accurate prediction of the pressure on the plunger than the empirical model. Comparison of the results of the analytical and the empirical models in the *x*-direction for baling wheat straw indicated that the empirical model had more accurate overall prediction for the pressure along the compression chamber, and had the larger coefficient of determination and the lower overall standard error, while the analytical model provided more accurate prediction of the pressure only on the plunger. For baling whole green barley, results showed that both analytical and empirical models predicted the pressure distribution in the *x*-direction with similar accuracy. Therefore, in order to estimate the pressure distribution of baling whole green barley, either model could be used.

Comparing Eqs. 3.47 and 3.48 showed that the empirical model for the pressure distribution in the *x*- and *y*-directions have the same general form with different model constants. Comparing the analytical and empirical models for the pressure distribution in the *y*-direction (Eqs. 3.43 and 3.48) revealed that the empirical model in the *y*-direction had exactly the same general form as the first term of the analytical model in this direction. Since the value of the first term of Eq. 3.43 was very large relative to that of the other terms especially for the distances less than 150 cm (Table 4.5), the empirical model was selected similar to the general form of the first term of Eq. 3.43. Coefficient "*C*" in the empirical model was identical to the coefficient of the first term of the analytical model.

Table 4.5 Values of the different terms of Eqs. 3.40 and 3.43 as a function of distance form the full extension point of the plunger for barley straw.

Distance from the plunger (cm)	First term of Eq. 3.40 (kPa)	Rest of Eq. 3.40 (kPa)	First term of Eq. 3.43 (kPa)	Rest of Eq. 3.43 (kPa)
0.0	356.0	0.0	237.3	0.0
15.0	275.6	-0.1	183.7	0.3
30.0	212.2	-0.3	141.5	0.5
45.0	164.9	-0.5	109.9	0.6
60.0	127.1	-0.9	84.7	0.7
75.0	97.8	-1.3	65.2	0.8
90.0	75.5	-1.8	50.4	0.8
105.0	56.9	-2.3	37.9	0.8
120.0	45.2	-2.8	30.1	0.8
135.0	35.2	-3.3	23.5	0.8
150.0	27.4	-3.8	18.2	0.8
165.0	21.1	-4.4	14.1	0.8
180.0	16.3	-4.9	10.9	0.7
195.0	12.6	-5.5	8.4	0.7
210.0	9.7	-6.1	6.5	0.6
225.0	8.2	-6.7	5.0	0.6
240.0	7.8	-7.3	3.9	0.5

4.1.5 Analytical Model for Pressure-Density Relationship

Alfalfa bale density versus distance from the full extension point of the plunger along the compression chamber was plotted based on the analytical model of pressure-density (Eq. 3.52). This graph shows that bale density decreases with distance of up to 50.0 cm, and then remains almost constant up to the end of the compression chamber (Fig. 4.17), while in reality bale density should remain almost constant along the

compression chamber. This analytical model failed to accurately predict the bale density along the compression chamber length due to the assumptions made in the model development. This model was developed by assuming elastic behavior for forage materials, while these materials were not elastic in reality. Therefore, the unloading process in forage materials was not reversible. Figure 4.18 compares the pressure-density relationship based on the analytical model with the possible pressure-density relationship in reality. Point "A" is on the plunger; therefore the pressure and density at this point are the maximum pressure and density in the baling process. Point "B" is assumed to be a point at a distance x from the full extension point of the plunger. According to the analytical model (Eq. 3.52), point "B" should be on the pressure-density curve. Thus, the density at this point (γ_B) is much smaller than the maximum density (γ_{max}). In practice, point "B" will be probably somewhere at "C" instead of being at "B" due to the inelastic property of forage materials. Point "C" has a density close to the maximum density; therefore in reality density remains almost constant along the compression chamber length. On the other hand, point "C" still has the same pressure as point "B"; for this reason, the analytical model for the pressure distribution which is based on the same assumptions as the analytical model for the pressure-density relationship works well in the x-direction. Unfortunately, no experimental data of the bale density along the compression chamber were available to validate this analytical model. Figure 4.17 showed the bale density variation with distance from the plunger when the bale was inside the bale chamber, so it cannot be extended to the variation of the bale density after coming out of the compression chamber. When the bale is out of the compression chamber, the tied twines keep a constant pressure on the bale. This constant pressure can balance the bale density

along the bale length by densifying the looser parts and loosening the denser parts. Therefore, the bale final density will have a value which is approximately an average of the maximum and minimum densities of the bale in the compression chamber.

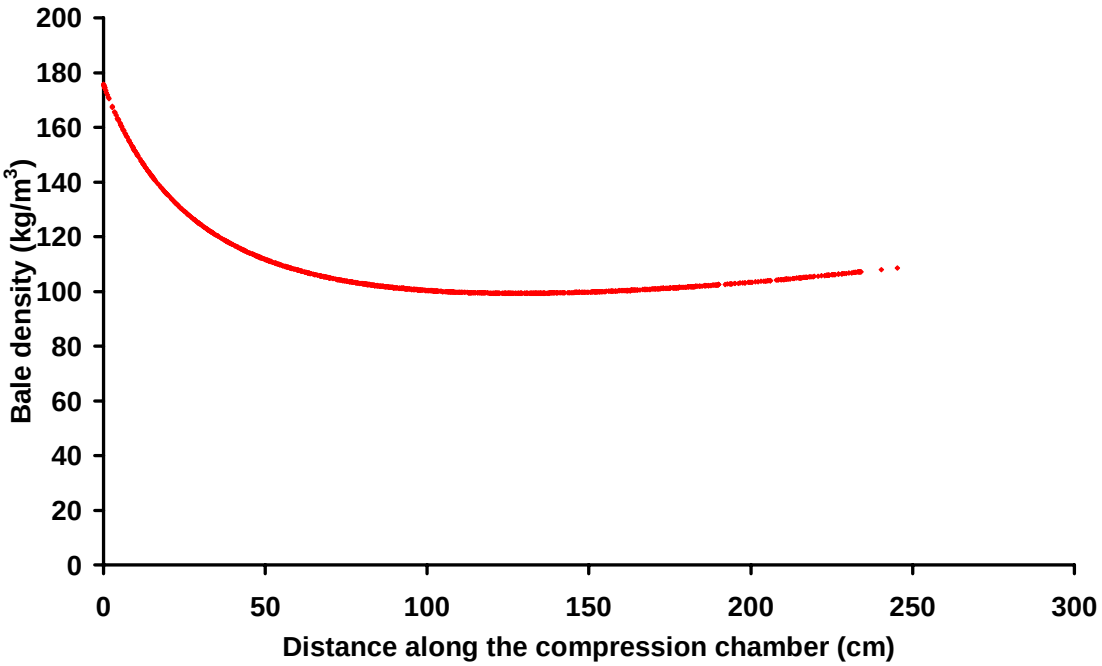

Figure 4.17 Variation of bale density along the compression chamber length for alfalfa at a moisture content of 12.4% (wb) based on the analytical model of pressure-density (zero on the *x*-axis is the full extension point of plunger).

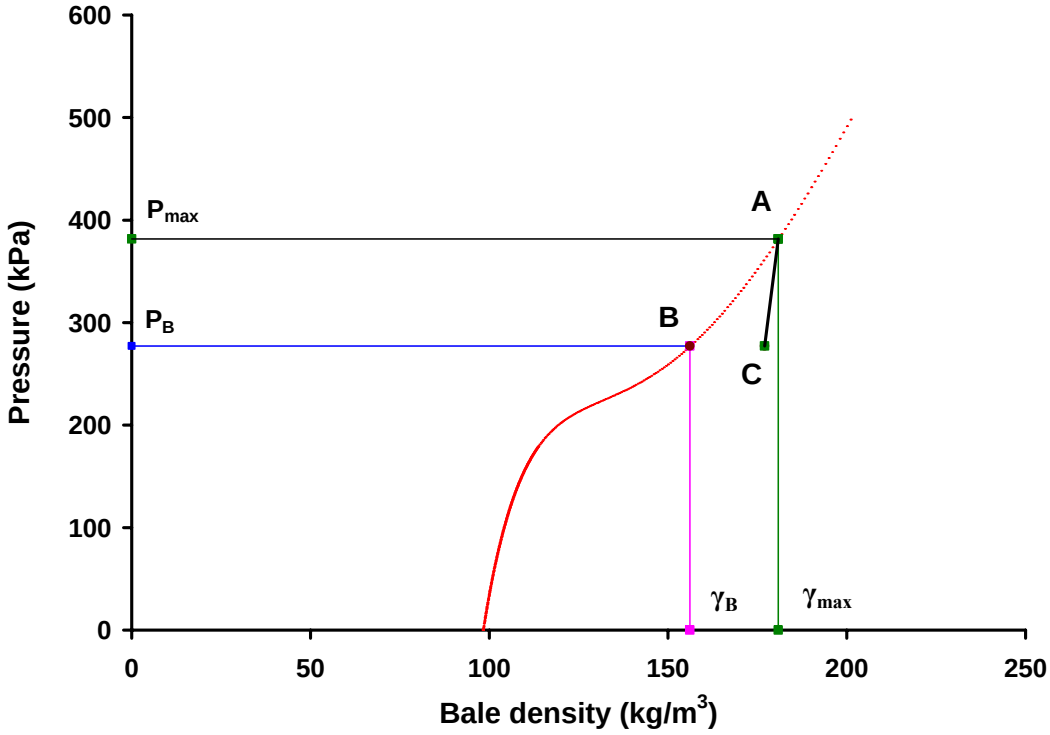

Figure 4. 18 Comparing the pressure-density relationship based on the analytical model with the possible pressure-density relationship in reality.

4.1.6 Empirical Model for Pressure-Density Relationship

Different models have been proposed for the pressure-density relationship of forage materials in the literature. Some of these models including those proposed by Ferrero et al. (1990), Viswanathan and Gothandapani (1999), Watts and Bilanski (1991), Butler and McColly (1959), and Bilanski et al. (1985) were tested with the data of the experimental tests to find the best model for the pressure-density relationship. The least-square regression analysis method was used to validate each model with the experimental data. In this method, model constant coefficients were changed in order to minimize the summation of the square difference between data resulting from each of

the models and the experimental data. Then, the standard error and the average error were calculated using the following equations (Figliola 2000):

$$SE = \sqrt{\frac{\sum_{i=1}^{n}\left[\left(y_p\right)_i - \left(y_e\right)_i\right]^2}{n}} \tag{4.1}$$

$$AE = 100\left(\frac{SE}{\bar{y}_e}\right)$$

where:

SE = standard error,

y_p = predicted data,

y_e = experimental data,

AE = average error and

$\bar{y}_e$ = average of the experimental data.

The model that had the minimum average error was selected as the best model. Results of validation of these models using the experimental data of alfalfa are shown in Table 4.6. This table showed that the developed model for the pressure-density relationship in this study (first model in the table) had the highest coefficient of determination and lowest average error. The coefficient of determination and average error for this model were 0.89 and 2.55%, respectively. This model was a modified version of model proposed by Ferrero et al. (1990). Experimental data and predicted density for alfalfa based on the proposed model (Eq. 3.54) versus plunger pressure are plotted in Figure 4.19. The standard error and the coefficient of determination for this model were 4.25 kg/m^3 and 0.89, respectively (Table 4.6).

The estimated values for the constant coefficients of this model are shown in Table 4.7. Models expressing pressure-density relationship in the literature were the results of compressing forage materials in a closed-end die which differed from the baler compression chamber used in the present study. Basically, the bale chamber of a baler is an open-end canal rather than a closed-end die. For this reason, none of the previously proposed models could be applied to the data of the pressure-density relation of the large square baler.

Table 4.6 Summary of validating of different models of pressure-density relationship with the data of baling alfalfa in the large square baler.

Pressure-density model		R^2	Average error (%)
$\gamma_s = \gamma_0 + (A_0 + B_0 P + CP^2)(1 - e^{-D_0 P})$		0.89	2.55
$\gamma_s = \gamma_0 + (A_0 + B_0 P)(1 - e^{-D_0 P})$	(Ferrero et al. 1990)	0.86	2.96
$(\gamma_{\max} - \gamma_s)/(\gamma_{\max} - \gamma_0) = e^{(-P/K)}$	(Bilanski et al. 1985)	0.85	3.02
$\gamma_i = k_1 \ln(\sigma / k_2)$	(Butler and McColly 1959)	0.83	3.27
$P = A_0 + B_0 \gamma_s + C\gamma_s^{\,2}$	(Viswanathan 1999)	0.87	5.91
$P = K_1 \log[1 - K_2(\gamma_s - \gamma_0)]$	(Watts and Bilanski 1991)	0.86	6.09

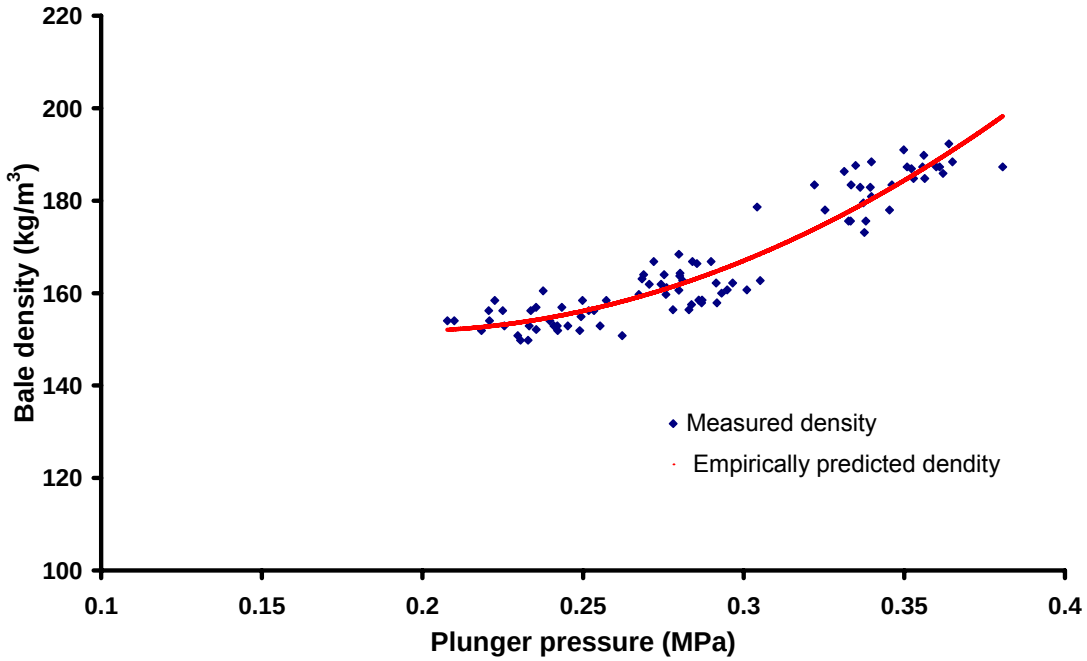

Figure 4.19 Experimental and the predicted densities vs. plunger pressure in a large square baler for alfalfa at a moisture content of 12.4% (wb).

Table 4.7 Estimated constants of the pressure-density model for alfalfa (Eq. 3.54).

Constant	Estimated values for alfalfa
γ_0	80.00
A_0	119.86
B_0	-501.53
C	1306.62
D_0	71.31
R^2	0.89
Standard error	4.25

Models proposed by Ferrero et al. (1990), Viswanathan and Gothandapani (1999), Watts and Bilanski (1991), Butler and McColly (1959), and Bilanski et al. (1985) were also tested with the data of barley straw to find the best model for the pressure-density relationship. Results of validation of these models using the experimental data of barley straw are shown in Table 4.8. This table showed that the developed model for the pressure-density relationship in this study (first model in the table) had the highest coefficient of determination and lowest average error. The coefficient of determination and average error for this model were 0.94 and 2.50%, respectively. The experimental data and predicted densities for barley straw based on the developed model (Eq. 3.54) versus the plunger pressure are plotted in Figure 4.20. The estimated values for the constant coefficients of this model are shown in Table 4.9. The standard error and the coefficient of determination of this model were 3.21 kg/m^3 and 0.94, respectively (Table 4.9).

Table 4.8 Summary of validating different models of pressure-density relationship with the data of baling barley straw in the large square baler.

Pressure-density model	R^2	Average error (%)
$\gamma_s = \gamma_0 + (A_0 + B_o P + CP^2)(1 - e^{-D_0 P})$	0.94	2.50
$(\gamma_{\max} - \gamma_s)/(\gamma_{\max} - \gamma_0) = e^{(-P/K)}$ (Bilanski et al. 1985)	0.94	2.52
$\gamma_i = k_1 \ln(\sigma / k_2)$ (Butler and McColly 1959)	0.94	2.55
$\gamma_s = \gamma_0 + (A_0 + B_0 P)(1 - e^{-D_0 P})$ (Ferrero et al. 1990)	0.92	2.89
$P = A_0 + B_0 \gamma_s + C\gamma_s{}^2$ (Viswanathan 1999)	0.93	7.81
$P = K_1 \log[1 - K_2(\gamma_s - \gamma_0)]$ (Watts and Bilanski 1991)	0.92	8.00

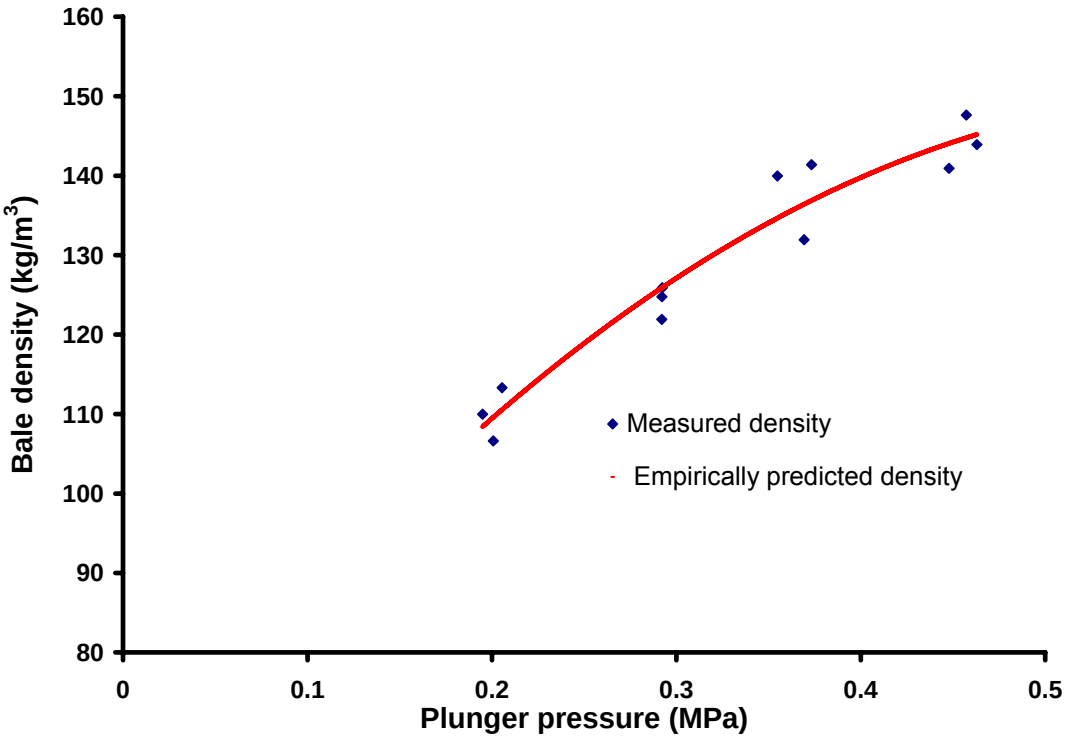

Figure 4.20 Experimental and the predicted densities vs. plunger pressure in a large square baler for barley straw at a moisture content of 8.7% (wb).

Table 4.9 Estimated constants of the pressure-density model for barley straw (Eq. 3.54).

Constant	Estimated values for barley straw
γ_0	50.00
A_0	9.11
B_0	301.66
C	-250.05
D_0	71.21
R^2	0.94
Standard error	3.21

4.1.7 Comparison of Analytical and Empirical Models

Comparison of the analytical and empirical models for bale density as a function of pressure on the plunger, P_p, (Eqs. 3.53 and 3.54) showed that these models had completely different general forms, but in both models bale density had a direct relationship with the material initial density and plunger pressure. Figure 4.21 represents the variation of the bale density of alfalfa with respect to the maximum pressure inside the compression chamber (P_p) based on both analytical and empirical models. According to these graphs, the trend of variation of density with pressure in both models is similar, but their rate of changes is different. Variation rate of density with pressure in the analytical model is higher than that of the empirical model. At low plunger pressures, the analytical model underestimates the bale density but at the higher pressures its prediction gets close to the real bale density. The cause of low accuracy in density prediction based on the analytical model is probably the assumptions made in deriving the analytical model. In the analytical model development, forage materials assumed to behave as an isotropic linear elastic material which is not true in reality.

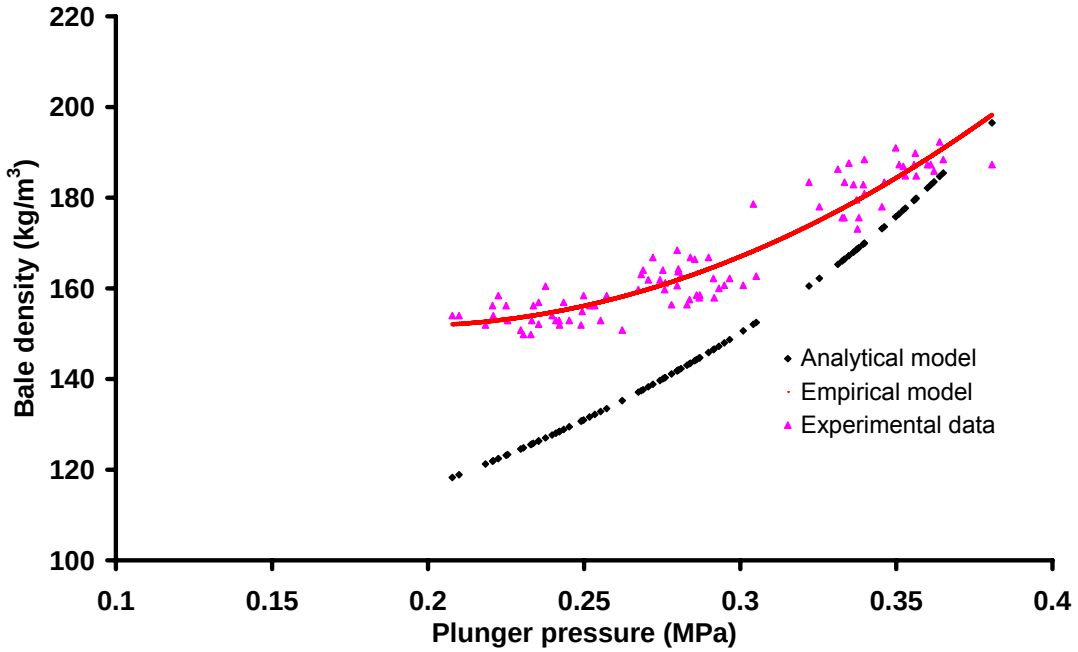

Figure 4.21 Experimental data and the predicted densities based on the analytical and empirical models vs. the plunger pressure in a large square baler for alfalfa at 12.4% (wb) moisture content.

4.1.8 Field Tests

Collected data from the experiments in both provinces (Saskatchewan and Québec) in 2001 were analyzed using a split plot design in the SAS software (SAS Institute, Cary, NC) except the evaluation of the flake size and load setting effect on the barley straw bale density in Québec. For this study, insufficient data were collected to do the statistical analysis. In this section, results of the effect of load setting and flake size on the plunger force and bale density are discussed. Results are provided for baling alfalfa and barley straw.

4.1.8.1 Baling Alfalfa

The analysis of variance of the data collected to test the effect of load setting and flake size on the plunger force showed that both the load setting and flake size had a significant effect on the plunger force (Table A.1). Means comparison analysis using the Duncan's multiple range test (DMRT) indicated that the difference between the plunger forces at all the load settings was significant even at the significance level of 1% (Table 4.10). Means comparison analysis of the plunger forces at different flake sizes revealed that at the significance level of 5%, the difference between all treatments was significant (Table 4.11). However, at the significance level of 1% there was a considerable difference only between the plunger force at flake size of 3/10 and the others (Table 4.11). The plunger force increased with increased percentage of the available maximum plunger force on the load pre-setting control system and flake size. Although, the plunger force was supposed to decrease with increasing flake size, results showed that the plunger force increased with increasing flake size. This was probably due to the increased flake size which increased the material rebounding after each plunger stroke. A greater plunger force with the increasing load setting was expected; therefore, when the load was set at 70% of the available maximum load, the plunger force reached its maximum value.

Table 4.10 Average plunger forces at different load settings for alfalfa (α = 0.01).

Load setting	Plunger force (kN)
50	255.6 a
60	305.5 b
70	372.3 c

a, b, c Averages with different letters were statistically different at 99% level.

Table 4.11 Average plunger forces at different flake sizes for alfalfa.

Flake size (plunger/stuffer ratio setting)	Plunger force (kN) (α = 0.05)	Plunger force (kN) (α = 0.01)
3/10	299.7 a	299.7 a
6/10	313.6 b	313.6 b
9/10	320.1 c	320.1 b

a, b, c Averages with different letters were statistically different.

The results of the analysis of variance for the effect of load setting and flake sizes on the alfalfa bale density are presented in Appendix A (Table A.2). These results revealed that load setting, flake size, and their interaction had significant effect on the alfalfa bale density at a significance level of 1%. The difference between all mean values of the bale densities at different load settings at a significance level of 1% was significant (Table 4.12). The mean comparison analysis of the bale density at different flake sizes showed that at the significance level of 5%, the bale density at the flake size of 3/10 was significantly different from bale densities at other flake sizes (Table 4.13). However, at the confidence level of 99% only the difference between the bale densities

at the flake sizes of 3/10 and 6/10 was significant (Table 4.13). The bale density drastically increased with increasing load setting, but slightly increased with increasing flake size, as expected. The effect of interaction between load setting and flake size on the bale density was significant only at the load setting of 70%. Bale density at the flake size of 3/10 at 70% load setting was significantly different from the bale density of this load setting at 6/10 and 9/10 flake sizes (Table 4.14).

Table 4.12 Average alfalfa bale densities at different load settings ($\alpha = 0.01$).

Load setting (as percentage of the available maximum load)	Bale density (kg/m^3)
50	154.3 a
60	161.8 b
70	183.8 c

a, b, c Averages with different letters were statistically different at 99% level.

Table 4.13 Average alfalfa bale densities at different flake sizes.

flake size (plunger/stuffer ratio setting)	Bale density (kg/m^3) ($\alpha = 0.05$)	Bale density (kg/m^3) ($\alpha = 0.01$)
3/10	165.2 a	165.2 a
6/10	167.5 b	167.5 b
9/10	167.2 b	167.2 ab

a, b Averages with different letters were statistically different.

Table 4.14 The effect of the interaction between load setting and flake size on the bale density for alfalfa.

Load setting (%)	Flake size	Bale density (kg/m^3)
50	3/10	155.1 a
50	6/10	155.1 a
50	9/10	152.6 a
60	3/10	162.4 b
60	6/10	161.7 b
60	9/10	161.3 b
70	3/10	178.0 c
70	6/10	185.8 d
70	9/10	187.6 d

4.1.8.2 Baling Barley Straw

A summary of the analysis of variance of the data showing the effect of load setting and flake size on the plunger load of the baler in the baling barley straw is presented in the appendix A (Table A.3). Results showed that plunger load was drastically affected by the load setting and interaction between load setting and flake size at 1% significance level, while flake size had no significant effect on the plunger load even at the significance level of 5%. Based on the mean comparison analysis, the difference between plunger loads at diverse load settings was significant at the significance level of 1%, therefore checking the difference between the treatments at the significance level of 5% was not necessary (Table 4.15). This analysis, on the other

hand, showed no significant difference between the plunger load mean values at the different flake sizes at the confidence level of 99% (Table 4.16). Whereas, means comparison showed a significant difference between plunger loads at flake sizes of 6/10 and 9/10 at the confidence level of 95% (Table 4.16). As expected, a higher load setting considerably increased the plunger load, while greater flake size slightly increased the plunger load due to more relaxation of the larger flakes. The interaction between load setting and flake size had a significant effect on the plunger force at all load settings but 60%. Results showed that at the highest level of load setting (100%) the medium flake size required the maximum plunger force, while at the medium load settings (60 and 80%) the thickest and at the lowest load setting (40%) the thinnest flake size needed the maximum plunger force (Table 4.17).

Table 4.15 Average plunger forces at different load settings for the baling barley straw ($\alpha = 0.01$).

Load setting (percent of available maximum plunger force)	Plunger force (kN)
40	216.4 a
60	317.7 b
80	397.8 c
100	492.4 d

a, b, c, d Averages with different letters were statistically different at 99% level.

Table 4.16 Average plunger forces at different flake sizes for the baled barley straw.

flake size (plunger/stuffer ratio setting)	Plunger force (kN) ($\alpha = 0.05$)	Plunger force (kN) ($\alpha = 0.01$)
3/10	354.9 ab	354.9 a
6/10	354.0 b	354.0 a
9/10	359.3 a	359.3 a

a, b Averages with different letters had statistically significant difference.

Table 4.17 The effect of the interaction between load setting and flake size on the plunger force for barley straw.

Load setting (%)	Flake size	Plunger force (kN)
40	3/10	221.9 a
40	6/10	210.5 ab
40	9/10	216.8 b
60	3/10	315.4 c
60	6/10	317.8 c
60	9/10	320.1 c
80	3/10	398.8 d
80	6/10	387.9 e
80	9/10	404.9 d
100	3/10	483.6 f
100	6/10	500.0 g
100	9/10	493.8 g

Average barley straw bale densities of the different treatments showed that the bale density significantly increased with increasing load setting (Table 4.18). Flake size had a slight effect on the barley straw bale density (Table 4.19); however, the number of data available for the barley straw density was insufficient to perform a complete statistical analysis. Results of flake size effect on the bale density in both tested materials also showed that at the low load settings, bale density decreased with increasing flake size (Table 3.2 and 3.3). This was probably because of more recovery (rebound) of the thicker flakes at the lower plunger pressures.

Table 4.18 Average barley straw bale densities at different load settings.

Load setting (percent of available maximum plunger force)	Bale density (kg/m^3)
40	109.9
60	124.1
80	137.7
100	144.1

Table 4.19 Average barley straw bale densities at different flake sizes.

Flake size (plunger/stuffer ratio setting)	Bale density (kg/m^3)
3/10	127.0
6/10	129.6
9/10	130.3

4.2 Sensor Design

Results of sensor sensitivity, sensor calibration, and sensor performance in the field are discussed in this section.

4.2.1 Sensor Sensitivity

The sensor showed an excellent linearity under the uni-axial vertical and horizontal loading calibration with no hysteresis in the unloading cycle (Figs. 4.22 and 4.223). Results of the primary, the secondary, and the cross sensitivities of the sensor for each of the horizontal and the vertical loadings are shown in the Table 4.20. The horizontal and vertical primary sensitivities of the sensor were 1479.7 and 1387.8 $\mu VV^{-1}kN^{-1}$, and cross sensitivities of four arm bridge outputs for the horizontal and the vertical loadings were 0.64% and 2.85%, respectively. Godwin (1975) reported draft and vertical cross sensitivities of 1.1 and 2.1%, respectively. McLaughlin et al. (1998) found a cross sensitivity of 1.9 and 7.0% for the draft and the vertical loadings. Gu et al. (1993) determined a range of 0 to 4% for the cross sensitivity. Therefore, the horizontal cross sensitivity determined in this study was the lowest compared to those previously reported, and the vertical cross sensitivity was found to be smaller than all reported vertical sensitivities but what reported by Godwin (1975).

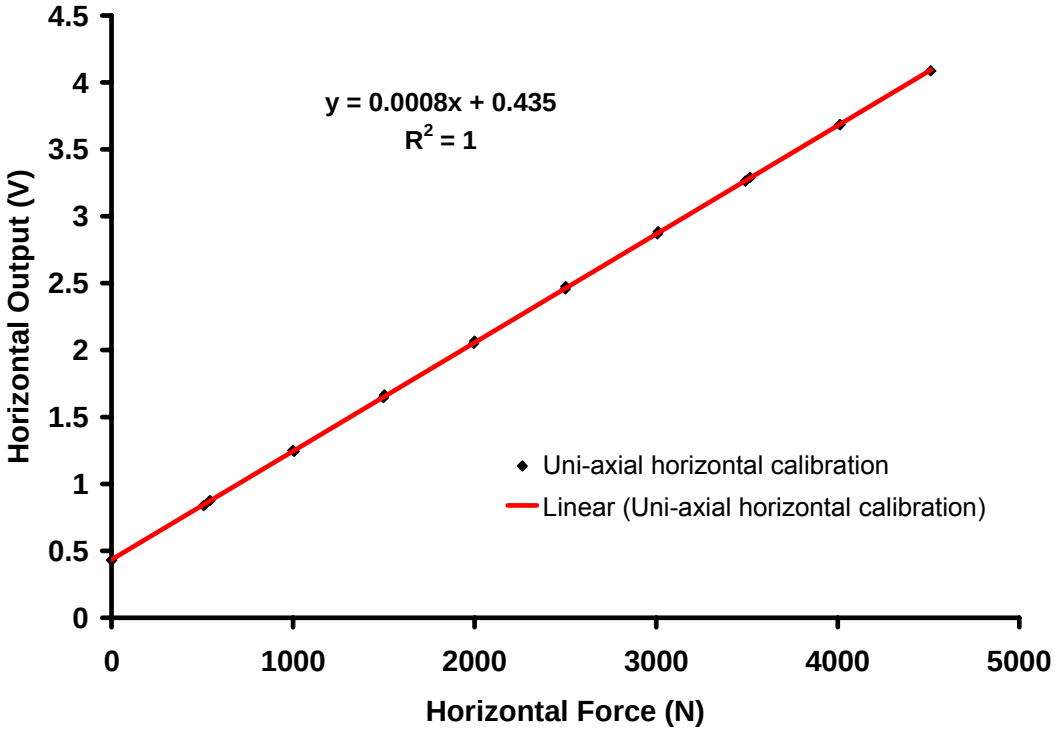

Figure 4.22 Uni-axial horizontal calibration of the tri-axial sensor.

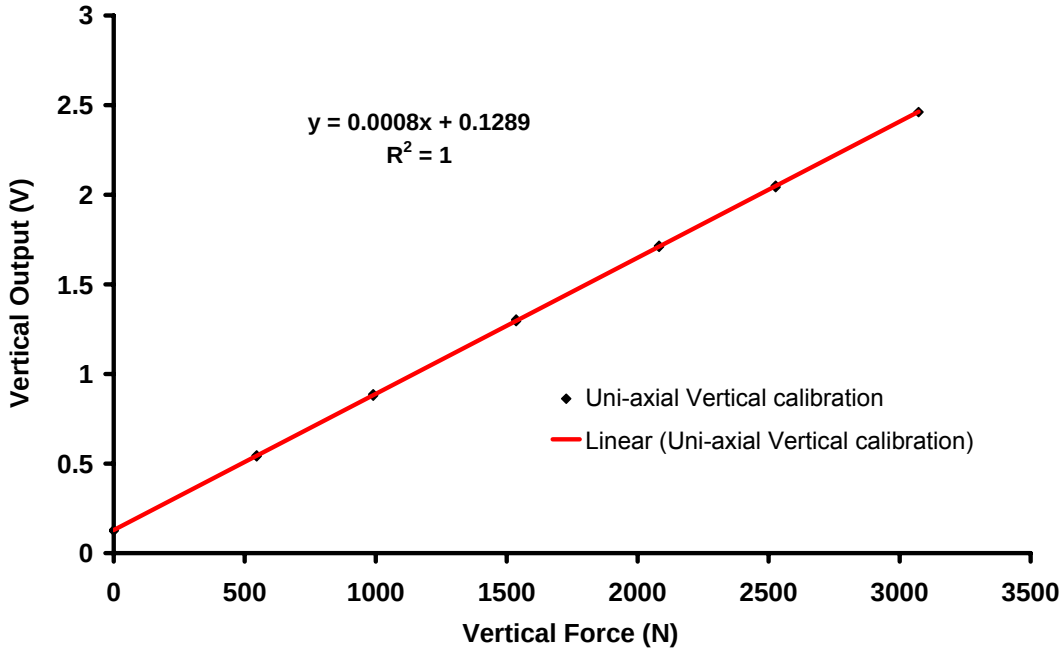

Figure 4.23 Uni-axial vertical calibration of the tri-axial sensor.

Table 4.20 Cross sensitivities of the sensor resulting from uni-axial calibration.

Loading axis	Primary sensitivity ($\mu VV^{-1}kN^{-1}$)	Secondary sensitivity ($\mu VV^{-1}kN^{-1}$)	Cross sensitivity (%) (Secondary/Primary)
x	1479.7	9.45	0.64
y	1387.8	39.55	2.85

4.2.2 Sensor Calibration

The tri-axial loading calibration data were used to develop the following calibration equations for the forces in the *x*-direction (draft) and the *y*-direction (vertical force) using multiple regression analysis.

$$F_x = c_x V_x + c_z V_y + c_i (V_x V_y) + c_0, \tag{4.3}$$

$$F_y = c_y V_y + c_x V_x + c_i (V_x V_y) + c_0, \tag{4.4}$$

where:

F_x, F_y = forces in the *x*- and *y*-directions (N),

V_x, V_y = output of the horizontal and vertical force measurement bridges (v) and

c_x, c_y, c_i, c_0 = model coefficients.

Least square method in multiple regression analysis was used to validate the developed models and estimate the model constant coefficients (Table 4.21).

Table 4.21 Estimated constants of the calibration equations of the sensor

Model	c_x	c_y	c_i	c_0
F_x	-1214.71	7.63	-13.91	-450.44
F_y	-15.48	-1313.99	-0.53	-223.41

Results of the multiple regression models for F_x and F_y showed that the best prediction model expressed the forces as a function of primary bridge output, secondary bridge output, and the interaction between the primary and secondary outputs. The predicted horizontal and vertical loads versus applied horizontal and vertical loads for the tri-axial loading calibration are plotted in Figures 4.24 and 4.25, respectively. The predicted forces were calculated using the abovementioned multiple regression models. Figure 4.24 showed that the regression model for the force prediction in the *x*-direction had successfully corrected the cross sensitivity effects from the forces in other directions on the force measurement in this direction. The coefficient of determination and the standard error in this case were 0.99 and 28.64 N, respectively (Table 4.22). The plot of the predicted vertical forces versus applied vertical forces showed that the regression model for the force in the *y*-direction had the ability to predict the applied forces to the sensor in the *y*-direction (R^2 = 0.99). However, the random error in this prediction was higher than that of the model predicting force in the *x*-direction. The coefficient of determination and the standard error for the force prediction in the *y*-direction were 0.99 and 86.5 N, respectively (Table 4.22).

Primary sensitivities of the EORs, calculated from the analytical equations and the strain gage bridge theory, were 1122.4 and 848.8 $\mu VV^{-1}kN^{-1}$ for the horizontal and

vertical sensitivities, respectively. These calculated sensitivities were 75.9 and 61.2% of the measured sensitivities (1479.7 and 1387.8 $\mu VV^{-1}kN^{-1}$). These results revealed that the analytical equations used for the EOR design (Eqs. 3.54 and 3.57) underestimated the stress at both positions ($\theta = \pm 39.5^{\circ}$ and $\theta = 90^{\circ}$) of the ring section of the EOR.

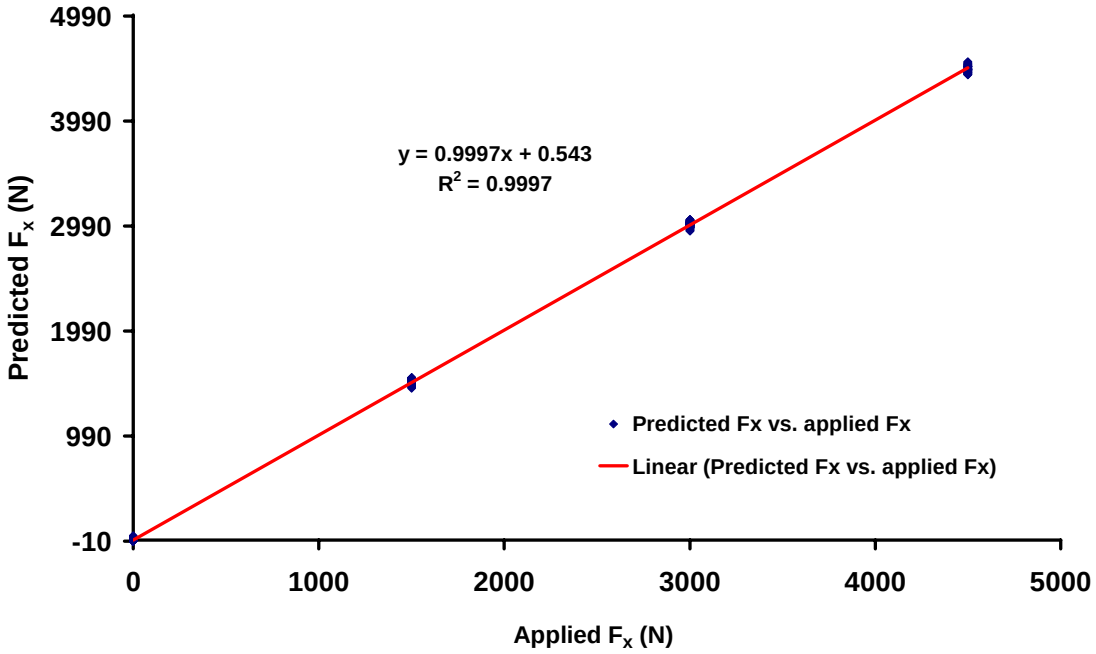

Figure 4.24 Predicted horizontal loads resulting from the developed model in the tri-axial calibration vs. the applied horizontal loads.

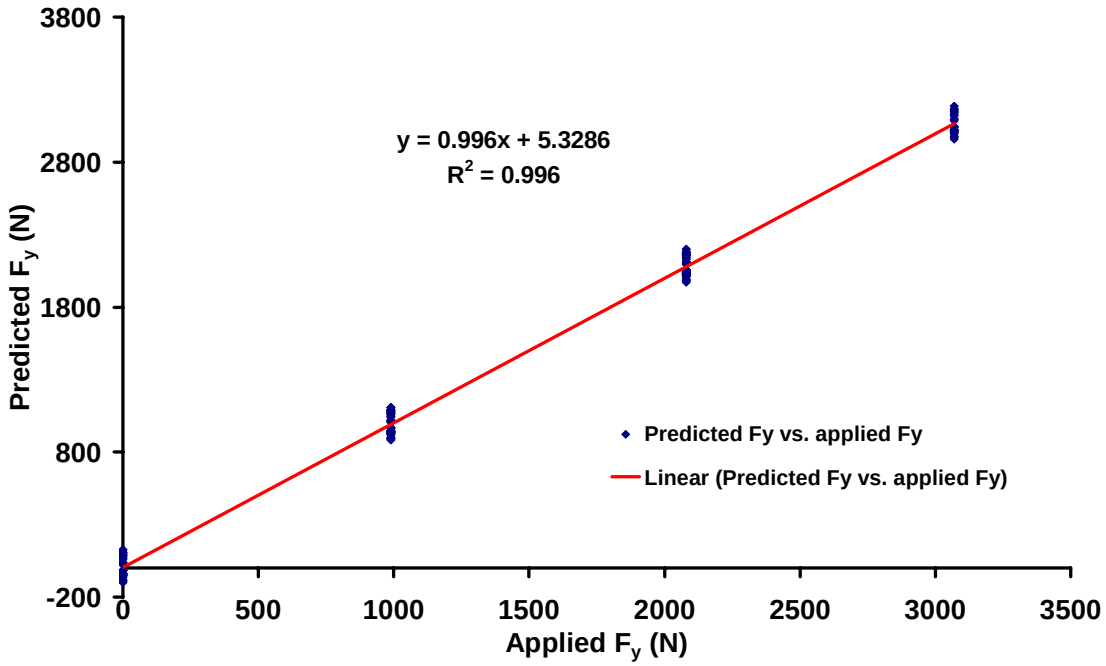

Figure 4.25 Predicted vertical loads resulting from the developed model in the tri-axial calibration vs. the applied vertical loads.

Table 4.22 The coefficient of determination and the standard error of the sensor calibration equations.

Model	R^2	Standard error (kPa)
F_x	0.99	28.64
F_y	0.99	86.5

4.2.3 Sensor Performance in the Field

Placing the sensor inside the compression chamber of the baler and its alignment inside the bale was the most difficult practical problem during the field tests. There was no reference inside the compression chamber and the bale to use for sensor alignment;

therefore, sensor alignment was performed observationally. This has probably made some misalignment for the sensor during the field tests which has caused some errors in the recorded forces. Meanwhile, since the dug hole in the bale for sensor was usually larger than the sensor size, there was a gap between the sensor body and the top and side walls of the dug hole. In practice, some of the applied forces in the *y*- and *z*-directions have been consumed to fill this gap. For this reason, recorded forces in the *y*-direction were lower than the expected forces. Results of force measurement inside the compression chamber in the *x*-direction were similar to the results obtained for the baler plunger maximum force by installing strain gages on the plunger arms. The error for the force measurement using the tri-axial sensor for barley straw was about 5%. However, there was no reference to evaluate the obtained forces by the sensor in the *y*-direction; results showed that the recorded forces were lower than the expected forces in this direction. The reason was probably the gap between the walls of the sensor and dug hole inside the bale. According to the theoretical analysis given in section 3.3.2.2, forces in the *z*-direction could not be recorded by the strain gages mounted on this sensor. Therefore, this sensor could only record the forces in the *x*- and *y*-directions. In practice, some values were obtained for F_z as a function of the difference between forces in the *x*-direction in two EORs, but the accuracy of this measurement was very low. In order to make the sensor a perfect tri-axial force transducer, a set of stain gages must be mounted on the side faces of the ring section of the EOR (Fig. 3.25) to be able to record F_z in addition to F_x and F_y.

4.3 Measurement of Crop Properties

Results of measurement of some crop properties such as coefficient of friction, adhesion coefficient, and modulus of elasticity are discussed in this section.

4.3.1 Friction and Adhesion Coefficients

Results of the analysis of variance of the effect of moisture content on the static coefficient of friction of alfalfa on a polished steel surface showed that alfalfa moisture content had a significant effect on the coefficient of friction at the confidence level of 99% (Table A.4). The coefficient of variation and the correlation coefficient in this case were 6.1 and 0.95, respectively. The coefficient of friction increased with increasing moisture content; however, the rate of the increment was larger for the higher moisture contents than that of the lower ones (Table 4.23). This result was in good agreement with the results reported for alfalfa and similar materials in the literature. Shinners et al. (1991) reported that moisture content had a significant effect on the coefficient of friction of alfalfa so that it was lower in the moisture range of 33 to 37% than the range of 73 to 77%. Mani et al. (2003) presented that moisture content had a significant effect on the coefficient of friction of corn stover grind. Ling et al. (1997) showed that both the static and the kinetic coefficients of friction of wood ash increased with increasing ash moisture content. At the confidence level of 95%, the difference between the coefficients of friction at all moisture contents was significant, while at confidence level of 99%, only difference between the coefficients at 12.0, 31.0, and 42.2% was significant (Table 4.23). The coefficients of friction for alfalfa ranged from 0.15 to 0.26 for moisture contents of 12.0 to 42.2% (wb). Efforts were made to develop a mathematical relationship between the coefficient of friction of alfalfa on a polished

steel surface and alfalfa moisture content. Therefore, the relationship between coefficient of friction and moisture content for alfalfa was best expressed by the following quadratic equation:

$$\mu = 7\times10^{-5} M_w^{\,2} - 10^{-4} M_w + 0.14, \qquad (4.5)$$

where:

μ = coefficient of friction and

M_w = moisture content % wb.

The experimental and predicted data of the coefficient of friction of alfalfa on a polished steel surface versus moisture content is shown in Figure 4.26. The coefficient of determination and the standard error of the model fitness were 0.95 and 0.01, respectively.

Table 4.23 Mean comparison of the static coefficient of friction of alfalfa on a polished steel surface at different moisture contents.

Moisture content (%)	Coefficient of friction (α = 0.05)	Coefficient of friction (α = 0.01)
12.0	0.15 a	0.15 a
22.0	0.17 b	0.17 ab
31.0	0.20 c	0.20 b
42.2	0.26 d	0.26 c

a, b, c, d Averages with different letters were statistically different. Each coefficient of friction represents average of fifteen samples.

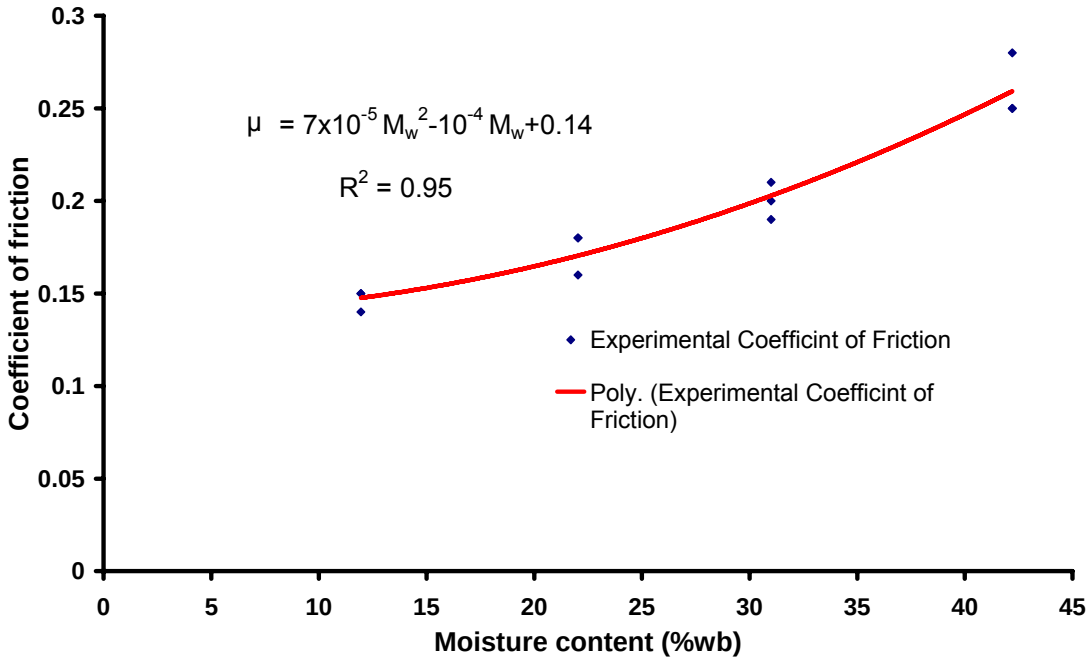

Figure 4.26 Experimental and predicted coefficients of friction of alfalfa on a polished steel surface vs. material moisture content.

Although, the difference between the adhesion coefficients of alfalfa on a polished steel surface at different levels of moisture content was considerable, the analysis of variance of the effect of moisture content on the adhesion coefficient showed no significant effect (A.5). This lack of effect could be partially due to a high coefficient of variation between the data. However, Duncan's multiple range mean comparison test showed a significant difference between the adhesion coefficients at 12.0% and 42.2% (wb) moisture contents at 95% of confidence level. The adhesion coefficient of alfalfa on a polished steel surface increased with increasing moisture contents from 12.0 to 31.0% (wb) and then decreased at the moisture content of 42.2% (Table 4.24). The lower adhesion coefficient at 42.2% moisture content could be related to the lubrication of steel surface by water released from the moist materials under pressure. No literature was found regarding adhesion coefficient of alfalfa to be able to compare the results

with, but some studies related to the effect of moisture content on the adhesion coefficient of some other forage materials have been reported. For instant, Mani et al. (2003) reported that moisture content had no significant effect on adhesion coefficient which is in agreement with the results of this study.

Table 4.24 Adhesion coefficient of alfalfa on a polished steel surface at different moisture contents.

Moisture content (%)	Adhesion coefficient (kPa)
12.0	2.1 a
22.0	11.4 ab
31.0	14.9 ab
42.2	8.3 b

a, b Averages with different letters were statistically different at 95% level. Each adhesion coefficient represents average of fifteen samples.

Results shown in Table A.6 indicated that the static coefficient of friction of barley straw on a polished steel surface was affected by moisture content, as stated in previous studies. Comparison of the treatment means proved that the difference between all treatments was significant at the confidence level of 95%. However, the difference between the coefficients of friction at moisture contents ranging from 12.2% and 32.8%, was not significant at confidence level of 99% (Table 4.25). The coefficient of friction for barley straw was in the range of 0.14 to 0.27 at moisture contents of 12.2 to 45.7% (wb). The relationship between the coefficient of friction of barley straw on a polished steel surface and moisture content is best expressed by the following linear equation:

$$\mu = 0.0037M_w + 0.1006, \quad (4.6)$$

where:

μ = coefficient of friction and

M_w = moisture content % wb.

The coefficient of determination and the standard error of the model were 0.93 and 0.013, respectively.

Table 4.25 Static coefficient of friction of barley straw on a polished steel surface at different moisture contents.

Moisture content (%)	Coefficient of friction ($\alpha = 0.05$)	Coefficient of friction ($\alpha = 0.01$)
12.2	0.14 a	0.14 a
20.3	0.18 b	0.18 ab
32.8	0.22 c	0.22 b
45.7	0.27 d	0.27 c

a, b, c, d Averages with different letters were statistically different. Each coefficient of friction represents average of fifteen samples.

The adhesion coefficient of barley straw on a polished steel surface was not significantly affected by the material moisture content, while the difference between the adhesion coefficients was considerable (Table A.7). However, Duncan's multiple range mean comparison test showed a significant difference between the adhesion coefficients at moisture contents of 20.3% and 45.7% at the confidence level of 95% (Table 4.26). Again the high coefficient of variation could be the reason for this lack of significant difference. The coefficient increased with increasing moisture contents ranging from

12.2 to 20.3% and then decreased with moisture contents ranging from 20.3 to 45.7%. The lubricating role of the released water from the moist material under pressure could explain the reduction of the adhesion coefficient at high moisture contents. The static coefficients of friction of wheat straw and whole green barley on a polished steel surface were measured at 10.0 and 51.0% moisture contents, respectively, which were 0.13 for the wheat straw and 0.21 for whole green barley.

Table 4.26 Adhesion coefficient of barley straw on a polished steel surface at different moisture contents.

Moisture content (%)	Adhesion coefficient (kPa)
12.2	5.9 ab
20.3	11.2 a
32.8	3.1 ab
45.7	0.2 b

a, b Averages with different letters were statistically different at 95% level. Each adhesion coefficient represents average of fifteen samples.

4.3.2 Modulus of Elasticity

In order to find a relationship between apparent modulus of elasticity and bulk density of alfalfa and barley straw, the data of the tests performed for the particle stiffness were used. The tangent method for the modulus calculation was used in this study. According to Eq. 3.60, when the tangent method is used to calculate modulus of elasticity, the obtained values are combination of modulus of elasticity and Poisson's

ratio ($\frac{(1-\nu)E}{(1+\nu)(1-2\nu)} = FE$). Since, Poisson's ratio is a constant coefficient, plotting the obtained values versus material bulk density can show the trend of variation of modulus of elasticity with material bulk density. Therefore, calculated values for alfalfa and barley straw were plotted versus material bulk density (*FE*-γ curve). Results for alfalfa showed that the apparent modulus of elasticity remained constant as the density increased from 100 kg/m^3 to 220 kg/m^3 (Fig. 4.27). Results for barley straw also showed that the apparent modulus of elasticity remained constant as the density increased from 100 kg/m^3 to 190 kg/m^3 (Fig. 4.28). Therefore, the results of this study proved that modulus of elasticity of alfalfa and barley straw was constant for the density range encountered in the large square baler.

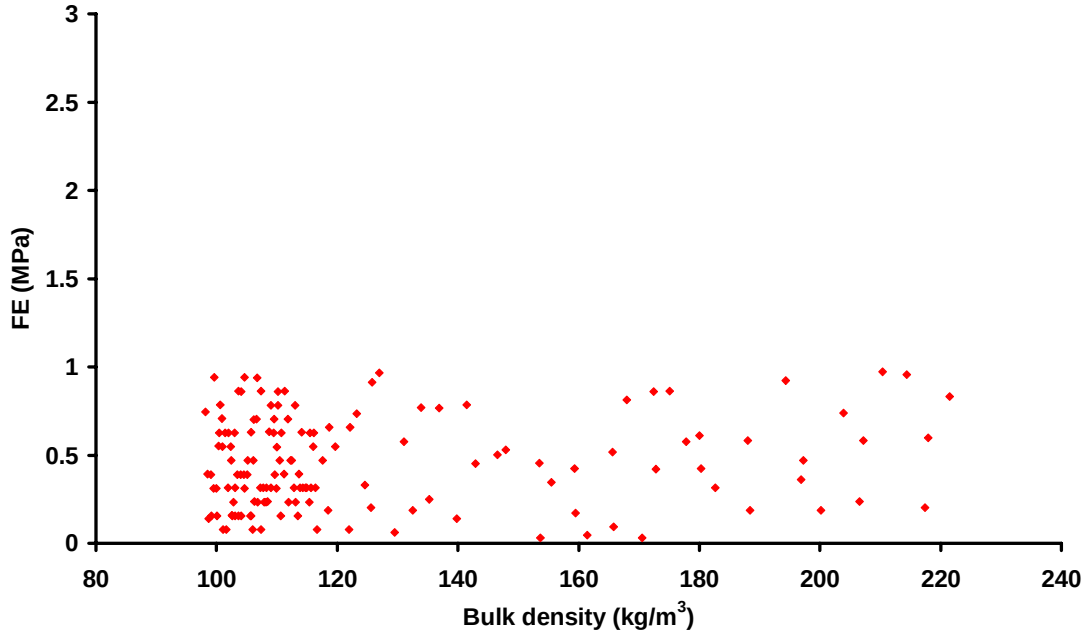

Figure 4.27 Variation of the apparent modulus of elasticity with bulk density of alfalfa (*E* is modulus of elasticity and *F* is a function of Poisson's ratio as defined in Eq. 3.61).

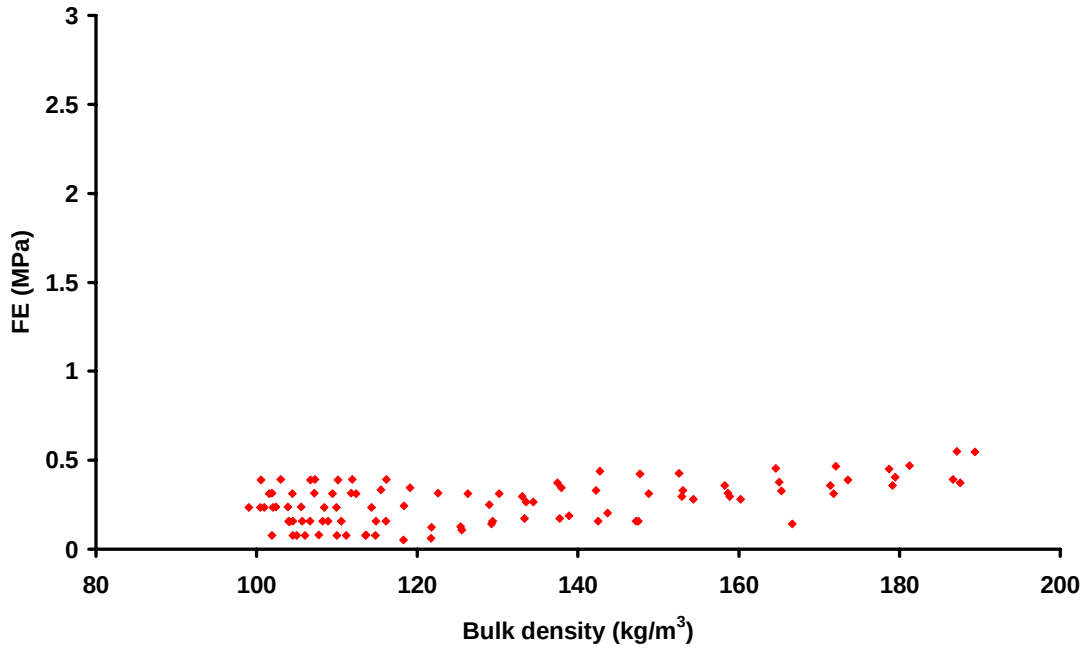

Figure 4.28 Variation of the apparent modulus of elasticity with the bulk density of barley straw (E is modulus of elasticity and F is a function of Poisson's ratio as defined in Eq. 3.61).

CHAPTER 5

SUMMARY AND CONCLUSIONS

5.1 Summary

This section is intended to provide a summary of the most important results achieved in this study.

5.1.1 Analytical Model for the Pressure Distribution

A new analytical model was developed for the pressure distribution inside the compression chamber of a baler by assuming isotropic linear elastic behavior for forage materials. Model development was performed according to the conditions of a large square baler. The new conditions involved the constant modulus of elasticity instead of the variable modulus of elasticity, and the inclined top and side walls instead of the inclined top wall in Sitkei's model (Eq. 2.19). The derived analytical model was found to be simpler and more convenient than Sitkei's model (Eq. 2.19). Results of the model validation showed that the analytical model accurately predicted the pressure in the *x*-direction, while the model was not accurate in the *y*- and *z*-directions. The overall standard error and the coefficient of determination of the regression analysis were 20.0 kPa and 0.95, respectively.

For wheat straw, the analytical model predicted the pressure on the baler plunger (maximum pressure) with the accuracy of 97.5%. The regression analysis of the experimental and the predicted data of the pressure distribution for wheat straw revealed

a standard error and a coefficient of determination of 26 kPa and 0.95, respectively. The overall standard error and coefficient of determination for whole green barley were 18.4 kPa and 0.96, respectively. Therefore, an acceptable correlation was found between the experimental data and the derived analytical model for each of forage materials tested in this study.

Comparing graphs of the pressure distribution of different forage materials based on the derived analytical model indicated that the pressure distribution for all tested forage materials had similar patterns. The maximum pressures for barley straw and wheat straw were approximately identical. Considering the fact that barley straw had been harvested at a lower load setting compared to the load setting for wheat straw (barley straw baled at a load setting of 60% and wheat straw baled at a load setting of 70%), the maximum pressure resulting from the baling barley straw was higher than that of wheat straw. The maximum pressure for whole green barley was inferior to those of the barley and wheat straw which was explained by the lower load setting (50%) and Poisson's ratio (0.32).

5.1.2 Empirical Model for the Pressure Distribution

Data of the experimental tests were used to develop an exponential empirical model for the pressure distribution inside the compression chamber of the baler for each of the tested forage materials (barley straw, wheat straw, and whole green barley) using regression analysis. These empirical models were simple equations which were only functions of the distance from the full extension point of the plunger along the compression chamber. These models had the identical general form for all forage materials in each specific direction with different model constants. Based on the results

obtained for baling barley straw, the best correlation between the experimental data and the predicted pressures was found at the beginning of the compression chamber length close to the plunger (maximum pressure inside the bale chamber) with an error of approximately 5%. The overall standard error and the coefficient of determination of the regression analysis in this case for model in the *x*-direction were 19.3 kPa and 0.96, respectively. For wheat straw, the empirical model overestimated the pressure in the *x*-direction on the baler plunger with an accuracy of 87.3% which was the lowest compared to the accuracy of the pressure prediction of the empirical model for the other crops at the same position. The regression analysis of the experimental and the predicted data of the pressure distribution in the *x*-direction for wheat straw presented a good coefficient of determination and a low standard error for the model correlation to the experimental data which were 0.97 and 20.6 kPa, respectively. Results of comparing the predicted and experimental pressures showed that the empirical model predicted the pressure on the plunger in the *x*-direction with the error of about 5% for whole green barley. The overall coefficient of determination and the standard error were 0.96 and 18.4 kPa, respectively. Comparing the experimental and the predicted pressure distribution in the *x*-direction revealed that the developed model for wheat straw overestimated the maximum pressure on the baler plunger, whereas models for barley straw and whole green barley estimated more accurate values for the maximum pressure on the baler plunger. The empirical model in the *y*-direction was not accurate because of the inaccurate experimental data.

5.1.3 Comparison of Models of Pressure Distribution

Comparing the results of the analytical and the empirical models in the *x*-direction for barley straw revealed that the empirical model provided more accurate pressure prediction with a larger coefficient of determination and a lower overall standard error; however, the analytical model provided more accurate prediction of the pressure on the plunger than the empirical model. Comparison of the results of the analytical and the empirical models in the *x*-direction for baling wheat straw indicated that the empirical model had more accurate overall prediction for the pressure along the compression chamber, and had the larger coefficient of determination and the lower overall standard error, while the analytical model provided more accurate prediction of the pressure only on the plunger. For baling whole green barley, results showed that both analytical and empirical models predicted the pressure distribution with similar accuracy. Therefore, in order to estimate the pressure distribution of baling whole green barley, either model could be used.

5.1.4 Pressure-Density Relationship

Analytical and empirical models were developed for the pressure-density relationship of the baler for baling alfalfa and barley straw. Results of plotting the analytical model versus distance from the plunger showed that bale density decreased with distance up to 50 cm, and then remained almost constant up to end of compression chamber. This model failed to accurately predict the bale density along the bale length because of the assumption made in the model development. The developed empirical model for both alfalfa and barley straw was a combination of a quadratic and an exponential equation. In order to validate the developed models, field tests were

performed by baling alfalfa and barley straw. For alfalfa with 12.4% moisture content, three flake sizes and three load settings were considered. Three levels of the flake sizes and four levels of the load settings were considered for barley straw with 8.7% moisture content. The forces on the plunger arms were recorded by a data acquisition system. The actual bale bulk density was calculated by measuring the bale dimensions and weight. Results showed that both load setting and flake size had a significant effect on the plunger force and bale density. The plunger force and bale density increased with increasing load setting and flake size.

Comparing analytical and empirical models for the bale density as a function of pressure on the plunger showed that the trend of variation of density with pressure in both models was similar, but the rate of change was different. The variation rate of density with pressure in the analytical model was higher than that of the empirical model. The analytical model underestimated the bale density at low plunger pressures but showed more accurate prediction at higher pressures, while the empirical model accurately predicted the bale density at low and high pressures.

5.1.5 Sensor Design

A tri-axial sensor was designed using an extended octagonal ring (EOR) and was calibrated uni-axially and tri-axially. The sensor showed excellent linearity and low cross sensitivities. Primary sensitivities of the EORs calculated from the analytical equations and the strain gage bridge theory were 1122.4 and 848.8 $\mu VV^{-1}kN^{-1}$ for the horizontal and the vertical sensitivities, respectively. These calculated sensitivities were 75.9 and 61.2% of the measured ones (1479.7 and 1387.8 $\mu VV^{-1}kN^{-1}$). Results revealed that the analytical equations used for the EOR design (Eqs. 3.55 and 3.58)

underestimated the stress at the all positions ($\theta = \pm 39.5^{\circ}$ and $\theta = 90^{\circ}$) of the ring section of the EOR. Results of the force measurement inside the bale compression chamber in the *x*-direction were close to the results obtained for the baler plunger maximum force from installing strain gages on the plunger arms. For barley straw, the error for the force measurement using the tri-axial sensor was approximately 5%. However, there was no reference to evaluate the obtained forces by the sensor in the *y*-direction; results showed that the recorded forces were lower than the expected forces in this direction. The reason was probably the gap between the walls of the sensor and the dug hole inside the bale. According to the theoretical analysis given in section 3.3.2.2, forces in the *z*-direction could not be recorded by the strain gages mounted on this sensor. Therefore, this sensor could only record the forces in the *x*- and *y*-directions.

5.1.6 Crop Properties

Results of the static coefficient of friction of different forage materials on the polished steel surface showed that the moisture content of the forage materials had a significant effect on the coefficient of external friction. The coefficient of external friction increased with increasing crop moisture content for both alfalfa and barley straw. The static coefficient of friction of alfalfa on a polished steel surface was a quadratic function of material moisture content, while the relationship between the coefficient of friction of barley straw on a polished steel surface and material moisture content was best expressed by a linear equation. Results of variation of modulus of elasticity with bulk density for both alfalfa and barley straw showed that the apparent modulus of elasticity remained constant as bulk density increased in the density range encountered in a large square baler.

5.2 Conclusions

This section is intended to list some of the most significant conclusions that can be drawn from this research based on the addressed objectives. These conclusions are outlined as follows:

1. Analytical models were developed for the pressure distribution inside the bale along the compression chamber length in the *x*-, *y*-, and *z*-directions based on theory of elasticity. The models were validated using experimental data in the *x*- and *y*-directions collected for barley straw, wheat straw, and whole green barley. The model in the *x*-direction was simpler and more convenient than Sitkei's model (Eq. 2.19) and showed a good correlation with the experimental data. The analytical models did not work in the *y*- and *z*-directions because of either inaccurate experimental data or inappropriate assumptions in model development.
2. Empirical models were also developed for the pressure distribution in the *x*- and *y*-direction for each of the tested forage materials using regression analysis. The model accurately predicted the pressures in the *x*-direction, while it had a poor accuracy in the *y*-direction.
3. Analytical and empirical models were developed for the pressure-density relationship of large square baler for alfalfa and barley straw. The empirical model had a good correlation with the experimental data, while the analytical model showed an inaccurate prediction of density particularly at the low plunger pressures.

4. Load setting and flake size had a significant effect on the plunger force and bale density. The plunger force and bale density increased with increasing load setting and flake size.
5. A tri-axial sensor was designed using EOR and was calibrated uni-axially and tri-axially. The sensor showed excellent linearity and low cross sensitivities.
6. The static coefficient of friction of alfalfa on a polished steel surface was a quadratic function of material moisture content, while the relationship between the coefficient of friction of barley straw and moisture content was best expressed by a linear equation.

5.3 Recommendations for Future Work

According to results and limitations of this study, the following recommendations can be given to make the future studies more effective in this area:

1. This study was limited to the modeling of variation of the pressure distribution in the *x*-, *y*-, and *z*-directions with respect to the *x*-direction. In other word, the sensor was located at the center of the bale cross-section area; therefore, forces were measured on the centerline of bale at different distances from plunger. In order to have a comprehensive understanding of pressure patterns inside the compression chamber, having the pressure variation in the *y*- and *z*-direction (pressure variation from center to top and side walls) are also necessary. Therefore, modeling of the variation of pressure in the *y*- and *z*-direction by locating sensors at different positions from center to top and side walls could be one of the objectives of the future studies.
2. The analytical models in the *y*- and *z*-directions were not validated in this study because of lack of accurate experimental data in these directions. Therefore,

validating these models using accurate experimental data can be another aspect of future work.

3. The analytical model for the pressure-density relationship was not validated in this study, because of lack of experimental data. Therefore, validation of the analytical model of pressure-density relationship by measuring the bale density variation along the bale length can be performed in the future.

4. Since the field experiments in present study were performed at one level of moisture content for each crop, evaluation of the effect of crop moisture content on the pressure-density relationship and pressure distribution models can also be considered in the future research.

REFERENCES

ASAE Standards, 47th Ed. 2001. S358.2-Moisture measurement-forage. 579. St. Joseph, Mich. ASAE.

Bickert, W. G and F. H. Buelow. 1966. Kinetic coefficient of grains on surfaces. Transactions of the ASAE 9(1):129-131, 134.

Bilanski, W. K., V. A. Graham and J. A. Hanusiak. 1985. Mechanics of bulk forage deformation with application to wafering. Transactions of the ASAE 28(3): 697-702.

Brubaker, J. E. and J. Pos. 1965. Determining static coefficients of friction of grains on structural surfaces. Transactions of the ASAE 8(1):53-55.

Burrows, C. R., J. N. Reed, P. Hogan, S. P. Tomlinson and M. A. Neale. 1992. Hydraulic flow division and ram synchronization in a high-density baler. Journal of Agricultural Engineering Research 53(4): 273-287.

Butler, J, L. and H. F. McColly. 1959. Factors affecting the pelleting of hay. Agricultural Engineering 40(8): 442-446.

Coblentz, W. K., J. O. Fritz and K. K. Bolsen. 1993. Baling system for making laboratory-scale hay bales. Agronomy Journal 85: 962-965.

Corrie, W. J. and D. A. Bull. 1969. Investigations into the characteristics of large bales. Journal of Agricultural Engineering Research 14(4): 323-331.

Culpin, C. 1986. Farm machinery, 11th ed. London, Britain. Collins Professional and Technical Books.

Faborode, M. O. and J. R. O'Callaghan. 1986. Theoretical analysis of the compression of fibrous agricultural materials. Journal of Agricultural Engineering Research 35(3): 175-191.

Fairbanks, G. E., S. C. Fransen and M. D. Schrock. 1981. Machine made stacks compared with round bales. Transactions of the ASAE 24(2): 281-283, 287.

Ferrero, A., J. Horabik and M. Molenda. 1990. Density-pressure relationship in compaction of straw. Canadian Agricultural Engineering 33(1): 107-111.

Figliola, R. S. and D. E. Beasley. 2000. Theory and design for mechanical measurements, 3rd ed. New York, NY, the United States of America. John Wiley and Sons, INC.

Freeland, R. S. and B. L. Bledsoe. 1988. Energy required to form large round hay bales-effect of operational procedure and baler chamber type. Transaction of the ASAE 31(1): 63-67.

Fung, Y. C. 1977. A first course in continuum mechanics, 2nd ed. Englewood Cliffs, New Jersey, the United States of America. Prentice-Hall, INC.

Godwin, R. J. 1975. An extended octagonal ring transducer for use in tillage studies. Journal of Agricultural Engineering Research 20:347-352.

Godwin, R. J., A. J. Reynols, M. J. O'Dogherty, and A. A. Al-Ghazal. 1993. A triaxial dynamometer for force and moment measurements on tillage implements. Journal of Agricultural Engineering Research 55:189-205.

Godwin, R. J., P. S. G. Magalhaes, S. M. Miller, and R. K. Fry. 1985. Instrumentation to study the force system and vertical dynamic behaviour of soil-engaging implements. Journal of Agricultural Engineering Research 36:301-310.

Gu, Y., R. L. Kushwaha, and G. C. Zoerb. 1993. Cross sensitivity analysis of extended octagonal ring transducer. Transactions of the ASAE 36(6):1967-1972.

Hall, G. E. and C. W. Hall. 1968. Heated-die wafer formation of alfalfa and bermudagrass. Transactions of the ASAE 11(4): 578-581.

Hann, S. A. and H. P. Harrison. 1976. Friction in and energy required for extruding alfalfa. Canadian Agricultural Engineering 18(1): 21-25.

Hoag, D. L., and R. R. Yoerger. 1975. Analysis and design of load rings. Transactions of the ASAE 19:995-1000.

Hundtoft, E. B. and F. H. Buelow. 1971. An axial stress-strain relationship for bulk alfalfa. Journal of Agricultural Engineering Research 16(1): 32-45.

Hunt, D. 2001. Farm power and machinery management, 10th ed. Ames, Iowa, the USA. Iowa State University Press.

Jenkins, B. M., D. A. Toenjes, J. B. Dobie, and J. F. Arthur. 1985. Performance of large balers for collecting rice straw. Transactions of the ASAE 28(2): 360-363.

Kepner, A. R., R. Bainer, and E. L. Barger. 1972. Principles of farm machinery, 2nd ed. Westport, Connecticut, the United States of America. The AVI Publishing Company, INC.

Lawton, P. J. and J. A. Marchant. 1980. Direct shear testing of seeds in bulk. Journal of Agricultural Engineering Research 25: 189-201.

Ling, Q., J. H. Wilhoit, and C. A. Flood. 1997. Static and kinetic friction coefficients of wood ash on stainless steel. ASAE Paper No. 976020. St. Joseph, Mich.: ASAE.

Lowen, E. G., E. R. Marshall, and M. C. Shaw. 1951. Electric strain gage tool dynamometers. Proceedings of the Society of Experimental Stress Analysis 8(2): 1-16.

Mani, S., L. G. Tabil, S. Sokhansanj, and M. Roberge. 2003. Mechanical properties of corn stover. CSAE Paper No. 036090. Montreal, Quebec: CSAE/SCGR.

McLaughlin, N. B. 1996. Correction of an error in equations for extended ring transducers. Transactions of the ASAE 39(2):443-444.

McLaughlin, N. B., S. Tessier, and A. Guilbert. 1998. Improved double extended octagonal ring drawbar transducer for 3-D measurement. Canadian Agricultural Engineering 40:257-264.

Mewes, E. 1958. Zum verhalten von pressgutern in prestopfen (on the behaviour of compressed matter in pressure chambers). Landtechnische Forshuny 8(6): 158-164.

Mewes, E. 1959. Verdichtungsgesetzmassigkeiten nach presstop fversuchen (compression relationships as a result of experiments in pressure chambers). Landtechnische Forshuny 9(3): 67-76.

Mohsenin, N. and J. Zaske. 1976. Stress relaxation and energy requirement in compaction of unconsolidated materials. Journal of Agricultural Engineering Research 21: 193-205.

Moysey, E. B. and S. Hiltz. 1985. Friction properties of fertilizers. Canadian Agricultural Engineering 27(2): 79-83.

New Holland. 2001. BB940, BB950, and BB960 Operator's Manual. New Holland North America Inc., New Holland, PA.

Norris, E. R. and W. K. Bilanski. 1969. Tensile properties of alfalfa stems. Canadian Agricultural Engineering 11(1): 14-15.

Osobov, V. I. 1967. Theoretical principles of compressing fibrous plant materials. Trudy Viskhom 55: 221-265.

O'Dogherty, M. J. 1975. A dynamometer to measure the forces on a sugar beet topping knife. Journal of Agricultural Engineering Research 20:339-345.

O'Dogherty, M. J. 1996. The design of octagonal ring dynamometer. Journal of Agricultural Engineering Research 63:9-18.

O'Dogherty, M. J. and J. A. Wheeler. 1984. Compression of straw to high densities in closed cylindrical dies. Journal of Agricultural Engineering Research 29(1): 61-72.

O'Dogherty, M. J. and H. G. Gilbertson. 1988. The relationship between bulk density and median chop length of chopped wheat straw samples. Journal of Agricultural Engineering Research 40(4): 245-257.

O'Dogherty, M. J. 1989. A review of the mechanical behavior of straw when compressed to high densities. Journal of Agricultural Engineering Research 44(4): 241-265.

O'Dogherty, M. J., J. A. Huber, J. Dyson and C. J. Marshall. 1995. A study of physical and mechanical properties of wheat straw. Journal of Agricultural Engineering Research 62(2): 133-142.

Pickard, G. E., W. M. Roll and J. H. Ramser. 1961. Fundamental of hay wafering. Transactions of the ASAE 4(1): 65-68.

Reece, F. N. 1966. Temperature, pressure, and time relationships in forming dense hay wafers. Transactions of the ASAE 9(6): 749-751.

Reece, F. N. 1967. Power requirements for forming wafers in a closed-die process. Transactions of the ASAE 10(2): 150-151.

Rehkugler, G. E. and W. F. Buchele. 1967. Influence of stem in alfalfa forage on the formation of wafers. Journal of Agricultural Engineering Research 12(4): 285-292.

Richter, D. 1954. Friction coefficients of some agricultural materials. Agricultural Engineering 35(6): 411-413.

Shinners, K. J., R. G. Koegel and L. L. Lehman. 1991. Friction coefficient of alfalfa. Transactions of the ASAE 34(1): 33-37.

Shinners, K. J., R. J. Straub and R. G. Koegel. 1992. Performance of two small rectangular baler configurations. Applied Engineering in Agriculture 8(3): 309-313.

Shinners, K. J., R. J. Straub, R. L. Huhnke and D. J. Undersander. 1996. Harvest and storage losses associated with mid-size rectangular bales. Applied Engineering in Agriculture 12(2): 167-173.

Sitkei, G. 1986. Mechanics of Agricultural Materials. Amsterdam, the Netherlands: Elsevier.

Snyder, L. H., W. L. Roller, and G. E. Hall. 1967. Coefficients of kinetic friction of wheat on various metal surfaces. Transactions of the ASAE 10(3):411-413,419.

Srivastava, A. C., W. K. Bilanski and V. A. Graham. 1981. Feasibility of producing large-size hay wafers. Canadian Agricultural Engineering 23(2): 109-112.

Stroshine, R. 2000. Physical properties of agricultural materials and food products. West Lafayette, Indiana, the USA.

Tabil, L. G., and S. Sokhansanj. 1997. Bulk properties of alfalfa grind in relation to its compaction characteristics. Applied Engineering in Agriculture 13(4): 499-505.

Thompson, S. A., and I. J. Ross. 1983. Compressibility and frictional coefficients of wheat. Transactions of the ASAE :1171-1176,1180.

Viswanathan, R. and L. Gothandapani. 1999. Pressure density relationship and stress relaxation characteristics of coir pith. Journal of Agricultural Engineering Research 73(3): 217-225.

Watts, K. C. and W. K. Bilanski. 1991. Stress relaxation of alfalfa under constant displacement. Transactions of the ASAE 34(6): 2491-2498.

Zhang, Q., M. G. Britton, and R. J. Kieper. 1994. Interactions between wheat and a corrugated steel surface. Transactions of the ASAE :951-956.

APPENDIX A

TABLES OF ANALYSIS OF VARIANCE

Table A.1 Analysis of variance of the data of the effect of flake size and load setting on the alfalfa plunger force.

Source	DF	SS	MS	F	P	R^2	CV
Flake size	2	6487.6	3243.8	24.7	<0.0001	0.95	3.7
Load setting	2	205830.5	102915.2	783.6	<0.0001		
Interaction	4	687.7	171.9	1.31	0.27		
Error	81	10638.8	131.3				
Total	89	223644.6					

Table A.2 Analysis of variance of data for the effect of the flake size and the load setting on alfalfa bale density.

Source	DF	SS	MS	F	P	R^2	CV
Flake size	2	96.7	48.4	5.6	0.005	0.95	1.8
Load setting	2	14124.7	7062.4	818.5	<0.0001		
Interaction	4	472.5	118.1	13.7	<0.0001		
Error	81	698.9	8.6				
Total	89	15392.8					

Table A.3 Analysis of variance of data of the effect of flake size and load setting on the plunger force for the baling barley straw.

Source	DF	SS	MS	F	P	R^2	CV
Flake size	2	519.6	259.8	2.74	0.07	0.99	2.7
Load setting	3	991904.9	330635.0	3489.6	<0.0001		
Interaction	6	2636.2	439.4	4.64	0.0004		
Error	84	7959.0	94.8				
Total	95	1003019.7					

Table A.4 Analysis of variance of data of the effect of the moisture content on the coefficient of friction of alfalfa on a polished steel surface.

Source	DF	Sum of squares	Mean square	F Value	Pr>F	R^2	Coefficient of variation
Model	3	0.0212	0.0071	49.8	<0.0001	0.95	6.1
Error	8	0.0011	0.0001				
Corrected total	11	0.0223					

Table A.5 Analysis of variance of data of the effect of the moisture content on the adhesion coefficient of alfalfa on a polished steel surface.

Source	DF	Sum of squares	Mean square	F Value	Pr>F	R^2	Coefficient of variation
Model	3	263.91	87.97	3.25	<0.081	0.55	56.61
Error	8	216.57	27.07				
Corrected total	11	480.47					

Table A.6 Analysis of variance of data of the effect of the moisture content on the coefficient of friction of barley straw on a polished steel surface.

Source	DF	Sum of squares	Mean square	F Value	Pr>F	R^2	Coefficient of variation
Model	3	0.0266	0.0089	38	<0.0001	0.93	7.5
Error	8	0.0019	0.0002				
Corrected total	11	0.0285					

Table A.7 Analysis of variance of data of the effect of moisture content on the adhesion coefficient of barley straw on a polished steel surface.

Source	DF	Sum of squares	Mean square	F Value	Pr>F	R^2	Coefficient of variation
Model	3	244.68	81.56	2.79	<0.11	0.51	114.09
Error	8	233.54	29.19				
Corrected total	11	478.22					

APPENDIX B

FORCES APPLIED TO THE TRI-AXIAL SENSOR

Forces applied on the cover plates of the sensor and a schematic of the sensor without cover plates are shown in Figures B.1 and B.2. F_y is applied on the center of the y side, while F_x and F_z have an offset of "b_0" with respect to the centers of x and z sides. Therefore, when the forces are transferred to the end of the bracket in addition to the moments $F_y a_0$ and $F_z a_0$, $F_x b_0$ and $F_z b_0$ also appear at that point (Fig. B.3). When the forces are transferred to the center of the bracket, $F_y a_0$ and $F_z a_0$ disappear and only $F_x b_0$ and $F_z b_0$ remain at the center of the bracket (Fig. B.4). These two moments ($F_x b_0$ and $F_z b_0$) and orthogonal forces (F_x, F_y, and F_z) apply bending stresses on the "S_1" and "S_2" sides of the ring section of the sensor (Fig. B.5). Distribution of stresses created by F_x and F_y is shown in Figure B.5b and the stress distribution created by F_z is shown in Figure B.5c. In order to sense the strains created by F_x, F_y, strain gages must be installed on the face "S_2", while strain gages on the face "S_1" sense the strain created by F_z.

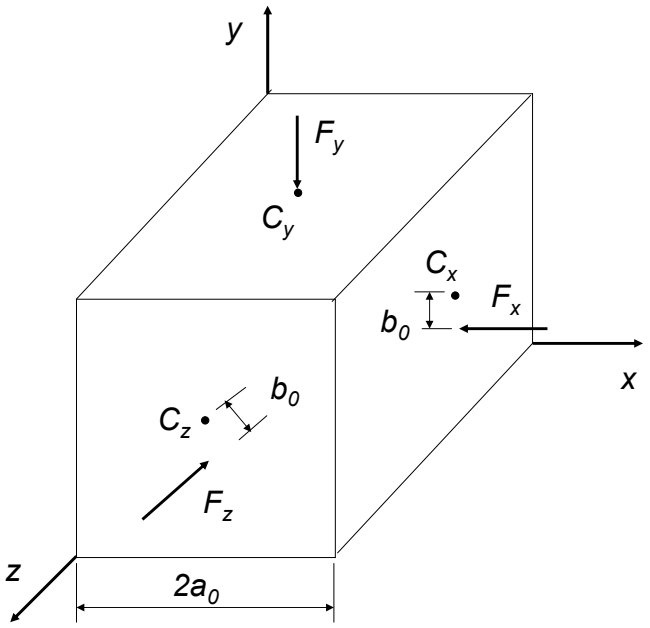

Figure B.1 Forces applied to the cover plates of the sensor.

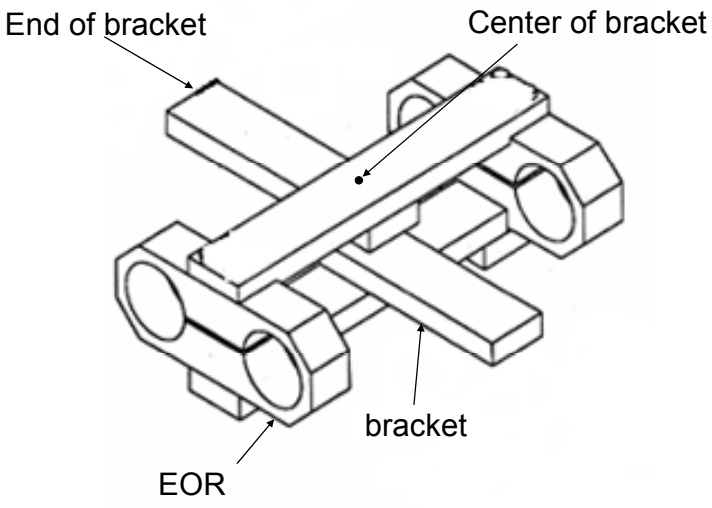

Figure B.2 Schematic of the sensor without cover plates.

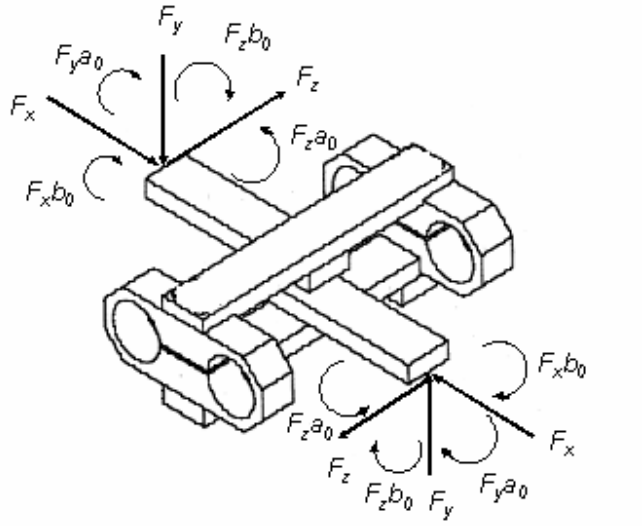

Figure B.3 Forces transferred from the covers to the hitch point of sensor.

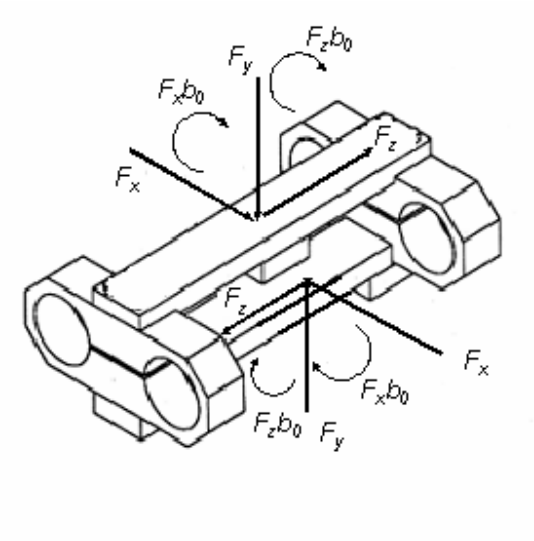

Figure B.4 Forces transferred from the hitch point to the center of braces.

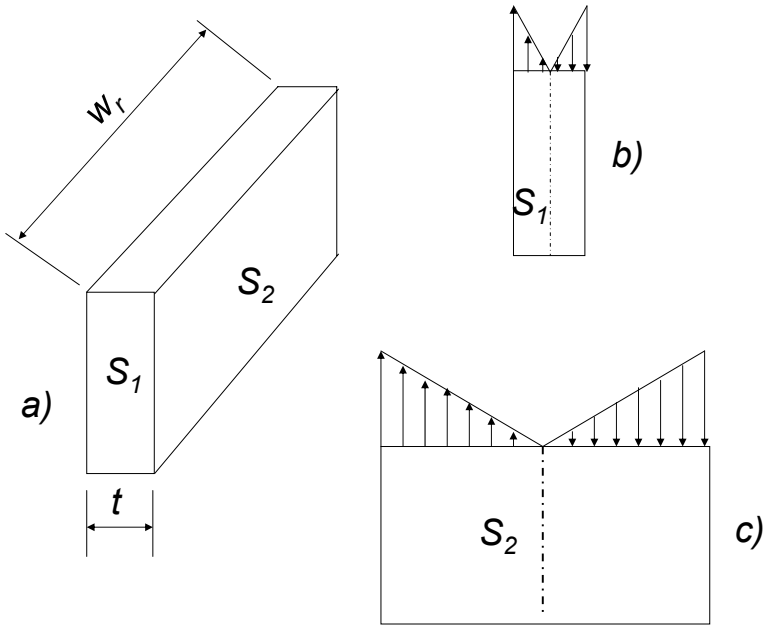

Figure B.5 Bending stresses applied to the ring section of the sensor. a) a section of the flexible part (ring section) of the sensor; b) bending stress applied by F_x and F_y on the cross-section of the ring; and c) bending stress applied by F_z on the cross-section of the ring.